MASARYKOVA UNIVERZITA

Přírodovědecká fakulta

Ústav teoretické fyziky a astrofyziky

Diplomová práce

Brno 2026 **Bc. Filip Holoubek**

MASARYKOVA UNIVERZITA

Přírodovědecká fakulta

Ústav teoretické fyziky a astrofyziky

Diplomová práce

Modelování asféricky interagujících supernov až po nebulární fázi

Bc. Filip Holoubek

Vedoucí práce: Mgr. Ing. arch. Petr Kurfürst, Ph.D.

Brno 2026

Bibliografický záznam

Autor:	Bc. Filip Holoubek Přírodovědecká fakulta, Masarykova univerzita Ústav teoretické fyziky a astrofyziky

Název práce:	Modelování asféricky interagujících supernov až po nebulární fázi
Studijní program:	Fyzika
Studijní plán:	Astrofyzika
Vedoucí práce:	Mgr. Ing. arch. Petr Kurfürst, Ph.D.
Akademický rok:	2025/2026
Počet stran:	IX + 79
Klíčová slova:	Supernovy, interakce s CSM, zářivá hydrodynamika, reinicializace simulace, světelné křivky, spektra, CASTRO, SIROCCO

Bibliographic entry

Author:	Bc. Filip Holoubek Faculty of Science, Masaryk University Department of Theoretical Physics and Astrophysics
Title of Thesis:	Modelling aspherically interacting supernovae up to the nebular phase
Degree Programme:	Physics
Field of Study:	Astrophysics
Supervisor:	Mgr. Ing. arch. Petr Kurfürst, Ph.D.
Academic year:	2025/2026
Number of Pages:	IX + 79
Keywords:	Supernovae, interactions with CSM, radiation hydrodynamics, reinitialisation of simulation, light curves, spectra, CASTRO, SIROCCO

Abstrakt

Supernovy interagující s okolní hvězdnou hmotou (CSM) se vyznačují mimořádnou svítivostí, která odhaluje historii ztráty hmoty před výbuchem předchůdce. Pro zachycení asymetrie těchto dějů byly kódem CASTRO provedeny dvourozměrné hydrodynamické simulace interakce supernovy s CSM. Byla vyvinuta vlastní metoda rozšiřování prostorové domény o čtyři řády, což optimalizovalo využití výpočetních zdrojů a umožnilo nepřetržité sledování exploze až do fáze pozůstatku supernovy. Hydrodynamické výstupy byly následně zpracovány kódem SIROCCO, řešícím přenos záření metodou Monte Carlo. Získané syntetické širokopásmové světelné křivky a spektra úspěšně odhalily klíčové morfologické trendy a geometricky závislé radiační jevy. Odvození těchto veličin navíc poskytlo důležité diagnostické poznatky o výpočetních limitech při přemapovávání. Práce tak přináší nejen ověřenou metodiku pro rozšiřování domény, ale i robustní rámec pro budoucí modelování pozorovatelných projevů supernov.

Abstract

Supernovae interacting with circumstellar medium (CSM) exhibit exceptional luminosity, revealing a progenitor's pre-explosion mass-loss history. To capture their asymmetry, 2D radiation-hydrodynamic simulations of CSM interactions were performed using the CASTRO code. A custom pipeline was created to expand the spatial domain across four orders of magnitude, optimising resources to continuously track the explosion into the remnant phase. Hydrodynamic outputs were subsequently processed using the SIROCCO Monte Carlo radiative transfer code. The synthesised broadband light curves and spectra successfully revealed key morphological trends and geometry-dependent radiative effects. Furthermore, the generation of these observables provided critical diagnostic insights into the computational limitations of discrete grid remapping, providing a verified domain expansion methodology and a framework for future observable generation.

MUNI
SCI

MASARYKOVA UNIVERZITA
PŘÍRODOVĚDECKÁ FAKULTA
KOTLÁŘSKÁ 2, 611 37 BRNO
IČ: 00216224
DIČ: CZ00216224

ZADÁNÍ DIPLOMOVÉ PRÁCE

Akademický rok: 2025/2026

Ústav:	Ústav teoretické fyziky a astrofyziky
Student:	Bc. Filip Holoubek
Program:	Fyzika
Specializace:	Astrofyzika

Ředitel *ústavu* PřF MU Vám ve smyslu Studijního a zkušebního řádu MU určuje diplomovou práci s názvem:

Název práce:	Modelování asféricky interagujících supernov až po nebulární fázi
Název práce anglicky:	Modelling aspherically interacting supernovae up to the nebular phase
Jazyk práce:	angličtina

Oficiální zadání:
The reason why these supernovae (SN) are interesting is that circumstellar medium (CSM) interactions are a very efficient engine for making bright transients, allowing superluminous transients to arise from normal SN explosion energies, and allowing transients of normal SN luminosity to arise from sub-energetic explosions or low radioactivity yield. Efforts to uncover the physical parameters of individual events and connections to possible progenitor stars make this a rapidly evolving topic that continues to challenge paradigms of stellar evolution. Using advanced hydrodynamic and radiation transfer codes, we calculate light curves and synthetic spectral features of SNe interacting with dense asymmetric CSM. We will also confront these theoretical outcomes with observed SNe.

Vedoucí práce:	Mgr. Ing. arch. Petr Kurfürst, Ph.D.
Datum zadání práce:	8. 8. 2024
V Brně dne:	8. 7. 2025

Zadání bylo schváleno prostřednictvím IS MU.

Bc. Filip Holoubek, 9. 8. 2024
Mgr. Ing. arch. Petr Kurfürst, Ph.D., 11. 8. 2024
Mgr. Dušan Hemzal, Ph.D., 27. 11. 2024

Poděkování

Na prvním místě bych rád poděkoval vedoucímu své práce, Dr. Petru Kurfürstovi, za jeho odborné vedení a cenné rady. Děkuji mu především za to, že dokončení práce věřil i ve chvílích, kdy simulace vázly a termín odevzdání se neúprosně blížil.

Mé další, avšak neméně důležité poděkování směřuje k Sabče. Bez její podpory a povzbuzení v situacích, kdy jsem sám pochyboval, bych tuto práci sotva dokončil. Jsem moc rád, že nás nepojí pouze několikaleté společné trauma.

Můj dík patří rovněž přátelům, kteří mě v mém směřování původně inspirovali, a všem, kteří mi po celou dobu studia dělali společnost a byli mi oporou. Závěrečné a obrovské díky patří našim a bráchovi za jejich nekonečnou trpělivost, kterou mi projevovali během obtížných studijních období i mých četných stěhování.

Prohlášení

Prohlašuji, že jsem svoji diplomovou práci vypracoval samostatně pod vedením vedoucího práce s využitím informačních zdrojů, které jsou v práci citovány.

V Brně dne 6. května 2026 .....

Filip Holoubek

Contents

Introduction

Core-collapse supernovae are traditionally classified by their spectral signatures. A distinct subclass is the Type IIn supernova (SN IIn), characterised by bright, narrow hydrogen Balmer emission lines. These lines originate from the violent interaction between the rapidly expanding supernova ejecta and a dense circumstellar medium (CSM). To understand the physical evolution of these systems, this thesis focuses on the multidimensional modelling of complex, asymmetric ejecta–CSM interactions.

This interaction efficiently converts kinetic energy into radiation, often producing extreme luminosities that can cross the threshold of Superluminous Supernovae (SLSNe). The primary objective of this thesis is to construct long-term, 2D radiation hydrodynamics (RHD) models of interacting supernovae and translate the resulting physical structures into synthetic spectra and light curves. By modelling distinct CSM geometries—specifically, an equatorial disc from binary interaction and bipolar lobes from pre-supernova eruptions—this work explores how the progenitor's mass-loss history shapes the remnant's morphology.

The methodological core of the thesis relies on combining hydrodynamics with radiative transfer. The hydrodynamic simulations are computed using the CASTRO code. To track the evolution from early shock breakout into the late nebular phase, a custom sequential reinitialisation routine was developed. This allowed the simulation domain to continuously expand up to ≈ 1 pc while keeping computational costs manageable. The resulting multidimensional data were then processed using a custom-built Julia package and fed into the SIROCCO Monte Carlo radiative transfer code to generate synthetic observables.

The thesis is structured as follows: Chapter 1 introduces the physics and observational signatures of ejecta–CSM interaction, while Chapter 2 explores the formation of asymmetric circumstellar environments. Chapter 3 outlines the computational tools (CASTRO and SIROCCO) and the analytical CSM setups. Chapter 4 details the custom domain reinitialisation routine and the Julia post-processing pipeline. Chapter 5 presents the physical results of the simulations alongside the synthetic observables. Finally, Chapter 6 discusses the physical and methodological implications of these findings.

Chapter 1

Physics and Observational Signatures of Supernovae

Supernova (SN) explosions are among the most energetic phenomena in the universe, typically releasing on the order of 10^{51} erg of kinetic energy in just a few seconds. While the vast majority of this energy drives the rapid expansion of the stellar ejecta, a critical fraction is emitted as electromagnetic radiation. The diversity of observed SN light curves and spectra reflects both the underlying explosion mechanism and the environment into which the star expands.

When fast-moving ejecta collide with a slower-moving CSM, strong shock waves form, converting kinetic energy into heat and radiation. This interaction can supplement, or even completely dominate, the standard luminosity powered by the radioactive decay of ^{56}Ni. Due to the high efficiency of this conversion process, CSM interaction provides a natural explanation for some of the brightest observed transients, as well as peculiar events where the synthesised radioactive yield is too low to account for the peak luminosity. Despite this, the majority of theoretical models for these interactions still assume spherical symmetry. In reality, both observations and stellar evolution theory indicate that the CSM is often highly asymmetric, having been shaped by binary interactions, rapid rotation, or pre-SN eruptive mass loss.

1.1 Energy Sources in Supernovae

Although SNe were distinguished from "classical" novae in the 1930s, a proper description of the explosion mechanism did not emerge until Hoyle & Fowler (1960) categorised them into two groups from the collapsing point of view:

- **Explosion without catastrophic implosion**. Thermonuclear runaway in degenerate conditions, which leads to the destruction of white dwarf stars and resulting in SN type Ia.

- **Implosion-explosion case**. The gravitational collapse of a massive star's core triggers an outward shock which is currently categorised as a core-collapse supernova (CC-SN).

1.1.1 Core-Collapse and Ejecta Asymmetry

Progenitors of CC-SNe spend most of their lives on the Main Sequence (MS), eventually forming a concentric nuclear burning shell structure around a degenerate iron core. When the core approaches the Chandrasekhar limit ($\sim 1.4\,M_{\odot}$), it collapses into a proto-neutron star. The initial rebound of the inner core creates a shock wave, but energy losses stall it deep within the star. Modern simulations demonstrate that this stalled shock is revived by intense neutrino heating from the contracting proto-neutron star (Woosley & Janka, 2005; Janka, 2012).

While the neutrino-heating mechanism provides the necessary energy, the resulting explosions are rarely spherical. The shock revival is heavily driven by multidimensional hydrodynamic instabilities, such as convection and the Standing Accretion Shock Instability (SASI). Rather than expanding symmetrically, SASI creates large-scale sloshing and bipolar oscillations that severely disrupt the star's spherical structure, transferring energy outward in an uneven, turbulent manner (Blondin et al., 2003; Foglizzo et al., 2007).

These intrinsic instabilities profoundly shape the morphology of the expelled material. Instead of expanding as a uniform shell, the heavy elements synthesised in the deep interior—specifically ^{56}Ni, ^{44}Ti, and ^{28}Si—are channelled into massive, high-velocity clumps. As a result, the ejecta front that impacts the CSM is characterised by these fast-moving macroscopic bullets (Wongwathanarat et al., 2013). This inherent asymmetry guarantees that the subsequent shock interactions with the surrounding environment will be complex and highly non-linear.

1.1.2 Supernova Light Curve Energy Sources

The way in which SN energy is thermalised and emitted is determined by the complex ejecta morphology (nickel-rich clumps and high-velocity fingers). The explosion mechanism determines the total energy budget, while the resulting light curve depends on how this kinetic and chemical energy is converted into radiation. For the SN interactions, three primary power sources can be identified: radioactive decay, hydrogen recombination and circumstellar interaction (additionally magnetars).

Radioactive decay ^{56}Ni → ^{56}Co → ^{56}Fe

The primary internal power source for the light curve is the radioactive decay of unstable isotopes synthesised during the explosion. The short-lived ^{56}Ni ($t_{\rm Ni} = 8.8$ days)

decays into ^{56}Co mainly via electron capture, dominating the early-stage energy input and powering the light curve peak (Arnett, 1982; Nadyozhin, 1994). Subsequently, the slower decay of ^{56}Co into stable ^{56}Fe ($t_{\mathrm{Co}} = 111.3$ days) powers the late-time bolometric tail.

For this radioactive energy to become visible, the decay products—specifically gamma rays resulting from electron capture and positrons generated via β^+ decay—must be trapped by the expanding ejecta, heating the matter to produce luminosity. As the ejecta expands and its density drops, it eventually becomes transparent to gamma rays, while positron kinetic energy often remains trapped to sustain the late-time tail. Crucially, multidimensional mixing caused by Rayleigh-Taylor instabilities creates clumping in the dense shells, which alters the local optical depth and dictates exactly when the matter becomes transparent to this radiation.

Cooling wave

The cooling wave is a phase transition driven by the expansion of the initially ionised, optically thick hydrogen envelope. As the ejecta expands and cools below the hydrogen recombination temperature ($\sim$6,000 K), protons and electrons recombine into neutral hydrogen (Grassberg et al., 1971). This reduces the electron scattering opacity, creating a sharp ionisation front that recedes into the ejecta mass.

Because the inward recession of this front roughly balances the outward physical expansion of the gas, the effective radiating radius and photospheric temperature remain relatively constant. According to the Stefan-Boltzmann law, this balance produces a sustained, homogeneous luminosity—the characteristic plateau phase defining SNe Type IIP (Popov, 1993; Dessart & Hillier, 2011). However, macroscopic mixing of ^{56}Ni outward into the envelope can alter the local optical depth, smearing the sharp luminosity drop typically expected at the end of this plateau (Kasen & Woosley, 2009; Wongwathanarat et al., 2015).

Circumstellar interaction

Circumstellar interaction acts as a dissipative mechanical engine, powering SN emission by directly converting macroscopic kinetic energy into thermal radiation. When expanding ejecta collide with a dense, slow-moving CSM, strong shocks form, producing a powerful flux of X-ray and UV radiation that is subsequently reprocessed into optical light by the optically thick CSM envelope (Chevalier & Fransson, 1994).

Because CC-SNe possess massive kinetic energy, this efficient shock mechanism can achieve extreme peak luminosities without requiring unphysical masses of radioactive isotopes, making it the accepted powerhouse for many SLSNe (Smith, 2014). Consequently, in environments with dense CSM, this interaction-driven luminosity com-

pletely dominates the emission, masking standard isolated explosion signatures like the hydrogen recombination plateau (Dessart et al., 2015).

1.2 Physics of Ejecta–CSM Interaction

While the previous section established circumstellar interaction as a dominant energy source, fully understanding the resulting observable light curves requires a detailed examination of the fluid dynamics (Smith, 2017). The fundamental physical scenario involves the supersonic SN ejecta colliding with a dense, slower-moving CSM previously shed by the progenitor star. This inelastic collision naturally drives a classic double-shock structure, consisting of a forward shock propagating into the ambient medium and a reverse shock driven back into the expanding ejecta (Chevalier, 1982). Due to the extreme densities involved in these specific environments, the highly pressurised shocked gas can cool radiatively at a rapid pace, severely altering the thermodynamic structure of the collision zone.

1.2.1 The Hydrodynamic Double-Shock Structure

The collision between the fastly expanding SN ejecta and the slower CSM produces a classic double-shock structure. As illustrated in Figure 1.1, this interaction region is broadly delineated by an outer forward shock sweeping into the ambient medium, an inner reverse shock propagating back into the stellar ejecta, and a central contact discontinuity separating the two shocked layers.

While the spatial geometry is mapped visually, the hydrodynamics of the shock are fundamentally governed by the contrasting boundary conditions of the two unshocked regions. The freely expanding inner ejecta travels at extreme velocities ($\sim 10^4$ km s^{-1}) with a steep density profile ($\rho_{\rm ej} \propto r^{-n}$, where n typically ranges between 7 and 12). Conversely, the outer unshocked CSM consists of a slow-moving stellar wind (10–500 km s^{-1}) defined by a shallower density profile ($\rho_{\rm CSM} \propto r^{-s}$, where $s = 2$ for a steady wind) dictated by the mass-loss rate of the progenitor star (Chevalier, 1982; Smith, 2017).

1.2.2 Radiative Cooling and the Cold Dense Shell

The forward and reverse shocks initially heat the swept-up gas to extreme temperatures capable of emitting X-rays. Because these specific SNe explode into an exceptionally dense CSM, the interaction region becomes highly collisional. This extreme density drives efficient radiative cooling. The gas radiates away its thermal energy much faster than it can cool via adiabatic expansion (Chevalier & Fransson, 1994; Smith, 2017).

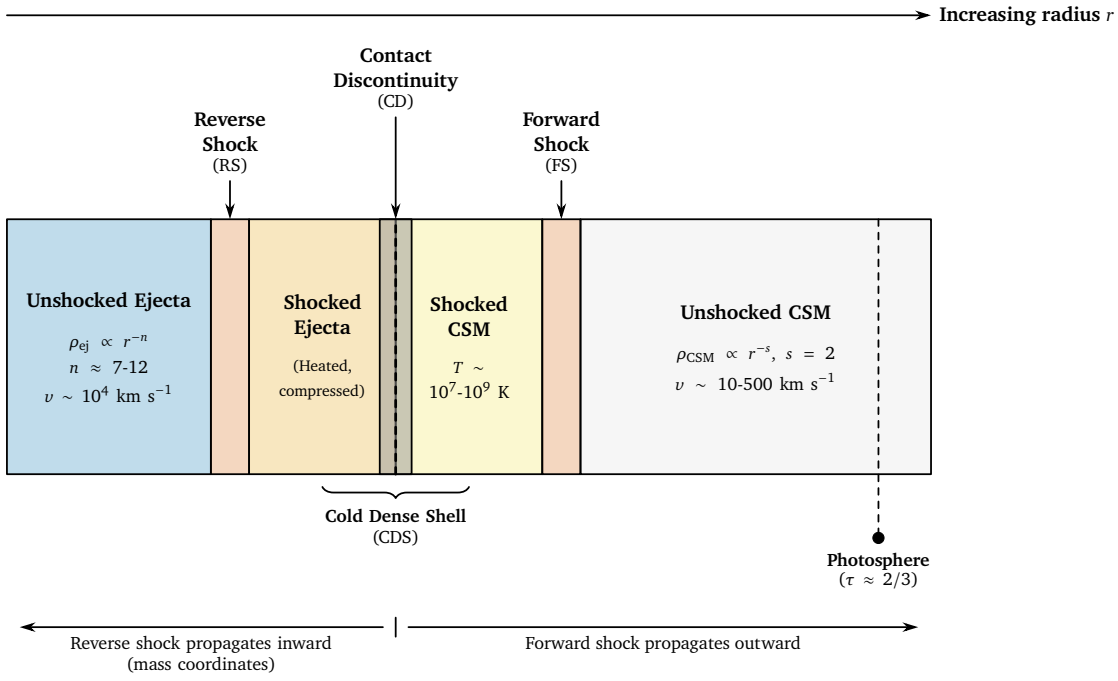

Figure 1.1: Schematic illustration of the radial structure of the ejecta–CSM interaction region in a Type IIn SN. The reverse shock and forward shock bracket the contact discontinuity, where radiative cooling forms the Cold Dense Shell. The optical photosphere (optical depth $\tau \approx 2/3$, dashed line) forms within the unshocked CSM, well outside the shock front. Zone widths are not to scale. Schematic representation conceptualised from the foundational 1D interaction framework of Chevalier (1982); Chevalier & Fransson (1994).

This strong radiative cooling drains the thermal energy of the post-shock gas, leading to a critical loss of its internal thermal pressure. Although the gas has lost its pressure support, it is still being rammed by the unshocked ejecta from behind and the unshocked CSM from the front. The interaction region physically collapses, resulting in a catastrophic compression into a geometrically thin but extremely dense layer known as the Cold Dense Shell (CDS). The CDS is located exactly at the contact discontinuity, where it effectively merges the shocked CSM and shocked ejecta into a single structure (Chevalier & Fransson, 1994).

1.2.3 Hydrodynamic Instabilities in the Interaction Region

The CDS is vulnerable to fluid instabilities, such as Rayleigh-Taylor and non-linear thin-shell instabilities, which cause the rapid disruption of the uniform spherical shell. Rayleigh-Taylor fingers grow outward from the contact discontinuity, driven by strong vorticity and tangential flows (Blondin et al., 1996; Vlasis et al., 2016).

As these fingers protrude, combined with Kelvin-Helmholtz instabilities along the shear boundaries, they induce macroscopic mixing of the shocked ejecta into the shocked CSM. This process fractures the interaction region into a highly inhomogeneous, clumpy structure, breaking the symmetry assumed in idealised 1D models. While the broad morphology of SNe IIn light curves is primarily determined by macroscopic factors, such as varying CSM mass and optical depths, this microscopic clumping and mixing changes the local shock dynamics. This chaotic interaction leads to the complex, multi-component emission observed in these transients (Dessart et al., 2015; Vlasis et al., 2016).

1.3 Observational Classification and Taxonomy

Historically, the classical taxonomic system for SNe relies on the macroscopic presence or absence of hydrogen in their optical spectra, dividing them broadly into Type II and Type I events, respectively (Minkowski, 1941; Filippenko, 1997). This foundational classification scheme depends on observing the intrinsic, expanding photosphere of the exploded star. In a standard core-collapse event, the emitted light originates from a photosphere receding through the freely expanding ejecta, allowing observers to detect the normal broad-line signatures that reveal the intrinsic elemental composition of the explosion. However, when an SN's fast-moving ejecta crashes into a dense CSM, the resulting shock interaction generates bright emission that completely shrouds the fast ejecta (Smith, 2017). Because this external environmental interaction effectively masks the normal photospheric signatures, it breaks the standard classification system, demanding a specialised taxonomic approach to accurately categorise these interacting transients (Filippenko, 1997; Gal-Yam, 2012). The full observational classification scheme, with the interaction-powered classes highlighted, is summarised in Figure 1.2.

1.3.1 The Type IIn Designation

In 1990, the taxonomic classification of CC-SNe was expanded to include a new subclass - Type IIn (Schlegel, 1990). The letter "n" stands for narrow, describing the relatively narrow or intermediate-width emission lines that differentiate these transients from typical, broad-lined Type II SNe. Unlike standard core-collapse events, SNe IIn lack the broad P Cygni absorption profiles characteristic of freely expanding ejecta. Observationally, their early continuum is remarkably blue and remains so for an extended period. Because the ongoing shock collision continuously replenishes the thermal energy of the system, their overall spectral evolution proceeds at a significantly slower rate over the first 50 to 100 days. Photometrically, this continuous energy injection results in optical light curves that often exhibit both higher peak luminosities

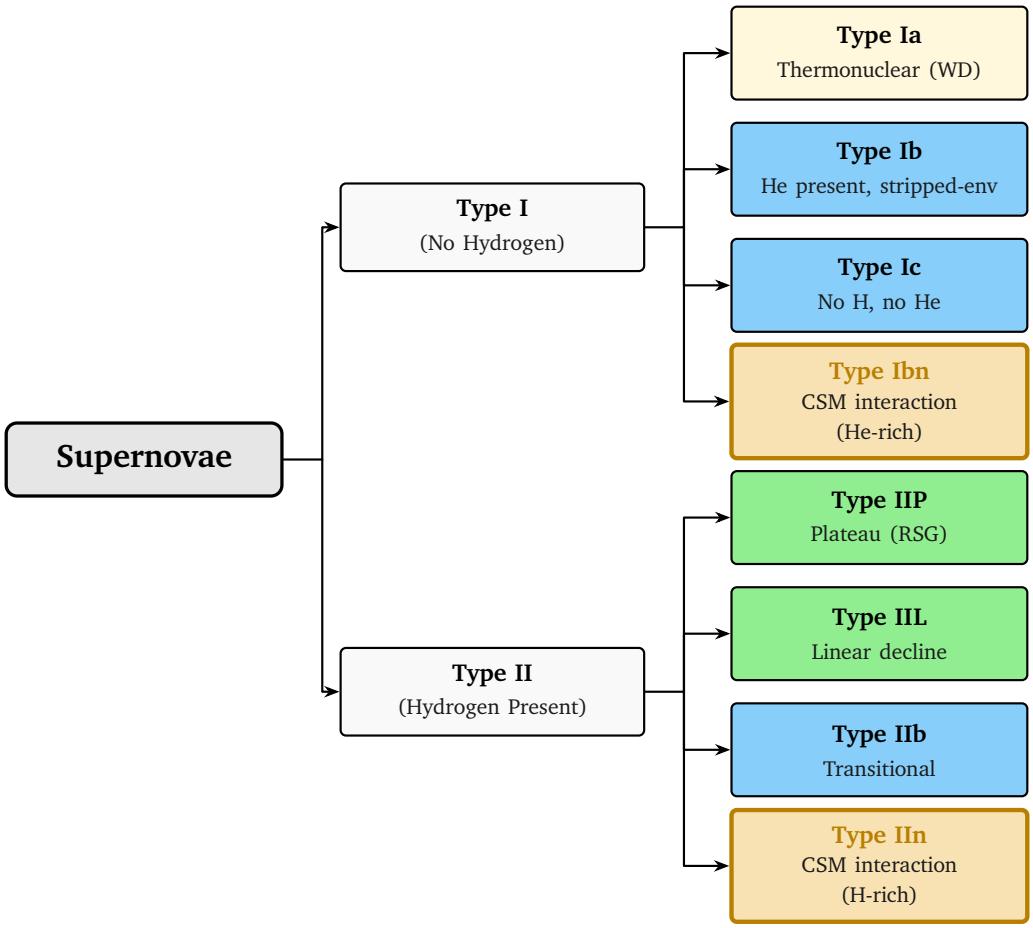

Figure 1.2: Classification tree of SN types following the observational scheme of Filippenko (1997). The primary division separates hydrogen-poor (Type I) from hydrogen-rich (Type II) events. Node colours indicate physical category: thermonuclear (cream), core-collapse H-rich (green), core-collapse stripped-envelope (blue), and interaction-powered (gold). Type IIn and Type Ibn, highlighted in gold, form the focus of this thesis.

and a notably slower decline from maximum light (Schlegel, 1990; Filippenko, 1997).

Spectroscopically, these transients are defined by their complex, multi-component hydrogen emission lines, which typically consist of narrow, intermediate, and broad features. While the narrower cores trace the kinematics of the unshocked and shocked CSM, a very broad base is frequently present, featuring a full width at half maximum (FWHM) of $\approx 5,000$–$10,000$ km s^{-1}. Unlike the narrower emission cores, this broad base does not represent the physical expansion velocity of the gas; rather, it is primarily a radiative transfer effect driven by extreme electron scattering within the dense, ionised CSM (Chugai, 2001). Figure 1.3 illustrates this characteristic three-component Hα profile, as seen in the well-studied SN 2010jl.

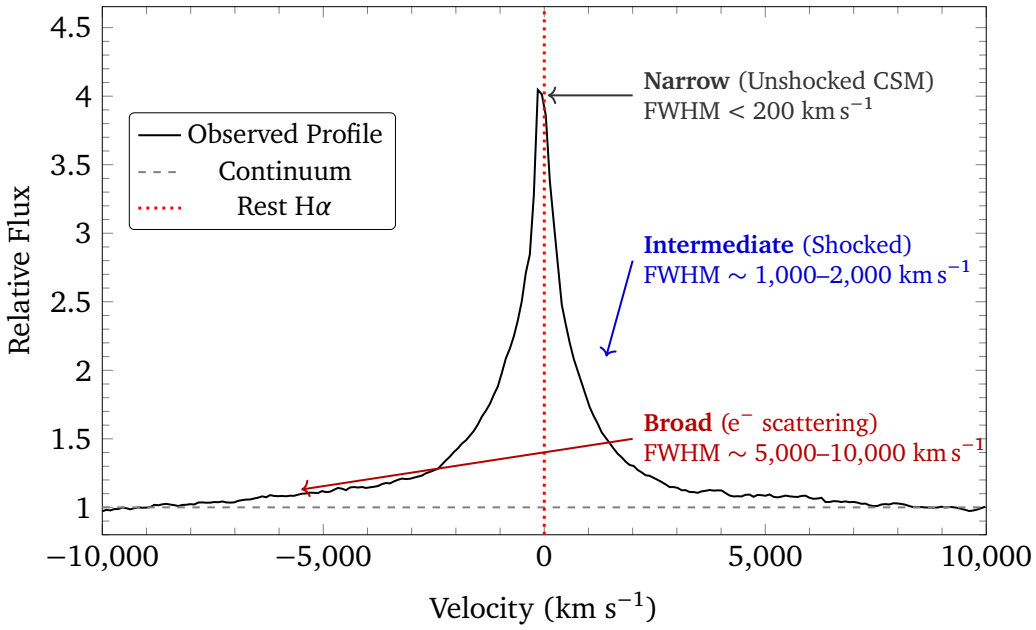

Figure 1.3: The Hα emission line profile of SN 2010jl at day 27 post-discovery (Keck-/LRIS), showing the three characteristic velocity components of Type IIn SNe. Data from WISeREP (Yaron & Gal-Yam, 2012).

1.3.2 The Environmental Masking Problem

Unlike classical taxonomy, which categorises SNe based on their internal engines, the Type IIn designation describes an externally driven phenomenon. The primary radiation source is the conversion of kinetic energy into light at the shock front, rather than a photosphere receding through freely expanding ejecta powered by internal heating or radioactive decay (Smith, 2017).

Because the surrounding circumstellar gas is optically thick, this bright shock emission completely obscures the faster inner ejecta. This intense environmental masking results in the broad P Cygni absorption and late-time nebular lines of the explosion being completely filled in or blocked from view (Smith, 2017).

Consequently, the Type IIn designation does not correspond to a single stellar evolutionary path or unique progenitor type. Almost any SN-like energetic event can be observationally classified as a Type IIn SN, provided it is buried within a thick circumstellar envelope. This implies that, beneath the shock-dominated spectrum, the true event could be a CC-SN, a stripped-envelope explosion, a thermonuclear detonation of a white dwarf, or a non-terminal eruptive outflow (Smith, 2017).

1.3.3 The Type Ibn Supernova Subclass

The physical mechanism of circumstellar interaction is not confined to hydrogen-rich environments. This was notably demonstrated by the discovery of SN 2006jc, the

prototypical Type Ibn SN (Pastorello et al., 2007). Although Type Ibn and IIn SNe both exhibit narrow emission spectral lines that originate from a shockwave colliding with dense, slow-moving CSM, their chemical compositions differ. Unlike SNe IIn, whose spectra are dominated by narrow Balmer lines (hydrogen), the spectra of SNe Ibn are dominated by prominent narrow or intermediate-width helium (He I) emission lines. To be classified as Type Ibn, an SN's spectrum must show weaker Hα emission than He I λ5876 emission. Another distinguishing feature is the much faster fade, due to the gas lacking the high opacity typically provided by hydrogen (Smith, 2017). The differences in the spectra of these two branches are shown in Figure 1.4.

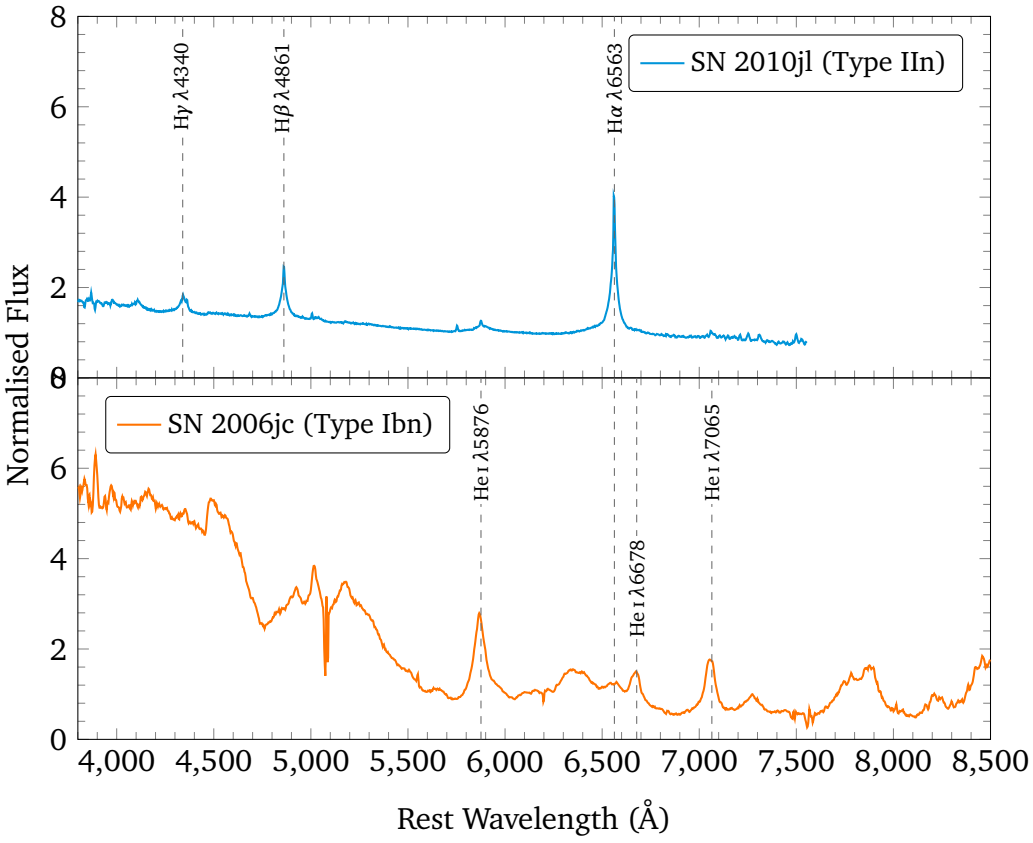

Figure 1.4: Optical spectra of the prototypical Type IIn SN 2010jl (Fransson et al., 2014) at day 27 (upper) and Type Ibn SN 2006jc (Pastorello et al., 2007) at day 14 (lower), normalised to the local continuum. The IIn spectrum is dominated by narrow Balmer emission, while the Ibn spectrum is dominated by (He I) λ5876, (He I) λ6678, (He I) λ7065 with no prominent Hα. Data from WISeREP (Yaron & Gal-Yam, 2012).

These two related types differ in terms of the stellar evolution of their progenitor and the resulting environment around it. As the dense, helium-rich CSM lacks hydrogen, the star must have shed its massive outer hydrogen envelope entirely prior to explosion. This stage of evolution eliminates Red Supergiants (RSGs) as possible progenitors. The primary suspects for the progenitor are Wolf-Rayet (WR) stars or Luminous Blue Variables (LBVs) that evolve into WR stars. This is supported by pre-

shock CSM velocities ($\sim 1,000$ km s^{-1}), which are much greater than those in the RSG environment. The extreme density of the shell implies that H-deficient WR stars can undergo sudden, massive pre-SN eruptions shortly before core collapse, which contradicts standard stellar evolution models that traditionally have no mechanism for such outbursts in H-depleted stars (Smith, 2017).

1.3.4 Photometric Diversity and the Superluminous Regime

The absolute peak magnitudes of SNe IIn do not represent a uniform category. Instead, their peak magnitudes range from moderate-luminosity events from approximately -17 mag, through a normal-luminosity population typically spanning -17 to -18.5 mag (Kiewe et al., 2012), and reaching up to extreme superluminous events brighter than -21 mag (Gal-Yam, 2012). Radiated luminosity is governed by the conversion of kinetic energy and scales directly with the density of the CSM (parameterised by $\dot{M}/v_{\rm wind}$) and the cube of the shock velocity ($L \propto \rho_{\rm CSM} v_{\rm shock}^3$) (Chevalier & Fransson, 1994). This process results in variations in brightness across the class that primarily reflect the varying densities of the surrounding environments rather than the intrinsic radioactive yields of the stellar cores.

Beyond peak luminosity, interacting SNe exhibit dramatic diversity in their light curve morphologies. For instance, the light curve of the superluminous SN 2006gy was characterised by a uniquely slow rise (≈ 70 days) and extreme magnitude peak, driven by smooth, highly efficient energy conversion as the ejecta collided with an exceptionally dense, massive CSM shell (the result of the pre-explosion mass loss of $\sim 0.1\ M_\odot$ yr^{-1}) (Ofek et al., 2007). Conversely, SN 2010jl exhibited a long-lasting, highly luminous plateau phase, powered by a radiative shock propagating through a vastly extended, massive circumstellar envelope (Zhang et al., 2012; Fransson et al., 2014). A third morphological category is defined by erratic, episodic rebrightenings; SN 2009ip, for example, displayed an unexpected double-peak light curve resulting from extreme density variations in the CSM. In this system, fast-moving ejecta collided with slower, pre-existing shells expelled by the progenitor's previous episodic eruptions (Pastorello et al., 2013). These examples demonstrate that the observed light curve is sculpted by the progenitor's mass-loss history, the total mass of the envelope, and the geometry of the CSM environment. The photometric diversity of the SN IIn class is illustrated in Figure 1.5, which compares the light curves of three representative events spanning the full range of observed morphologies.

The upper extreme of this photometric distribution defines the SLSN regime. Operationally, this threshold is crossed when an event achieves a peak absolute magnitude exceeding $M < -21$ mag, or equivalently, a peak bolometric luminosity greater than 7×10^{43} erg s^{-1} (Gal-Yam, 2012). Explaining such extreme radiative output, where the total radiated energy frequently approaches 10^{51} erg, through standard radioac-

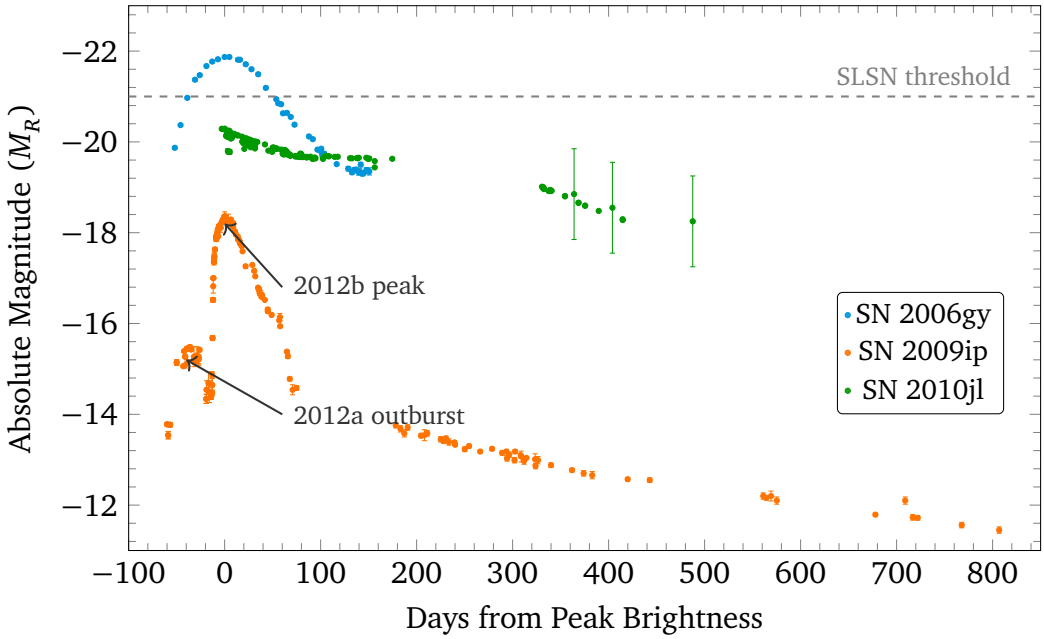

Figure 1.5: Absolute R-band light curves of three Type IIn supernovae illustrating the principal morphological categories of the class: the slow-rising superluminous SN 2006gy (Smith et al., 2007), which exceeds the SLSN threshold (dashed line, $M < -21$) at peak; the long-plateau SN 2010jl (Zhang et al., 2012; Fransson et al., 2014); and the episodically rebrightening SN 2009ip (Pastorello et al., 2013). For SN 2009ip, the main 2012b peak and the 2012a precursor outburst—generally attributed to violent, late-stage eruptive instabilities in the massive progenitor—are annotated. Magnitudes are corrected for distance and Milky Way extinction. Photometric data obtained from the Open Supernova Catalog (Guillochon et al., 2017).

tive decay is physically impossible in the context of a standard core-collapse event. Powering an event such as SN 2006gy through decay alone would require the synthesis of an unphysical $\sim 22\,M_\odot$ of ^{56}Ni, far exceeding the $\sim 0.07\,M_\odot$ typically produced by iron-core collapse (Smith et al., 2007). Therefore, highly efficient CSM interaction is the leading explanation of power source for these extreme transients. It is in this high-luminosity regime, where the CSM mass and geometry play a dominant role in shaping the observables, that one-dimensional spherically symmetric models face their most significant physical limitations.

1.4 Radiation Transfer in Interacting Supernovae

1.4.1 Optical Depth and the Photosphere

The most important quantity for radiative transfer is optical depth, which is defined as the integral of macroscopic opacity χ along the line of sight

$$\tau(z) = \int_{z}^{z_{\max}} \chi(z')\mathrm{d}z' . \tag{1.1}$$

The continuum photosphere is defined as the location where the optical depth reaches approximately $\tau \approx 2/3$. Once this boundary is reached, photons can escape to the observer freely (Mihalas & Mihalas, 1999).

Because SNe are dynamic events, it is not possible to define a physical surface as can be done, for example with a MS star. Standard SNe undergo a process of dynamic homologous expansion, whereby the density drops and the optical depth steadily decreases (scaling $\propto \tau^{-2}$ in the optically thick, electron-scattering dominated regime). The boundary $\tau \approx 2/3$ recedes inward in mass coordinates, revealing deeper layers of the explosion over time (Dessart & Hillier, 2011).

In contrast to the standard model of SNe, in SNe IIn, the forward shock generates radiation that propagates upstream, resulting in the significant ionisation of the pre-shock CSM. The pre-existing CSM is exceptionally dense and provides substantial optical depth. The boundary where $\tau \approx 2/3$ forms entirely within the unshocked CSM, which physically obstructs view of the underlying shock front and the actual SN ejecta (Chevalier & Fransson, 1994; Smith, 2017).

The optically thick envelope is composed of a hot, highly ionised, hydrogen-rich environment where opacity is not driven by atomic line absorption. It is dominated by pure electron (Thomson) scattering, where the opacity is provided by free electrons (Mihalas & Mihalas, 1999). It is the electron-scattering-dominated photosphere located within the unshocked CSM, rather than the ejecta, that reprocesses the high-energy shock emission into the observed optical radiation (Smith, 2017).

1.4.2 Shock Emission Reprocessing

The collision between the expanding ejecta and the slow-moving CSM converts kinetic energy into thermal energy, generating extreme post-shock temperatures of $10^7 - 10^8$ K. Consequently, the forward shock radiates predominantly in the X-ray and extreme ultraviolet (UV) bands. While standard SNe IIn generate shock luminosities on the order of 10^{43} erg s^{-1}, this X-ray and UV emission can surge to $\sim 10^{44}$ erg s^{-1} in the most extreme, highly dense circumstellar environments (Chevalier & Fransson, 1994).

This intense X-ray and UV radiation propagates ahead of the shock front into the

distant, cold, neutral CSM. The radiation drives a rapid ionisation front that strips electrons from the neutral gas, creating a highly ionised precursor. By ionising the gas, the advancing radiation field provides the substantial Thomson scattering opacity (Fransson et al., 1996).

The newly ionised CSM ahead of the shock front becomes highly opaque to X-rays due to electron scattering. These high-energy photons are absorbed, thermalised, and degraded to lower energies through a continuous reprocessing cascade. As detailed by Dessart et al. (2015), because the extended, unshocked wind remains optically thick to this reprocessed radiation, the effective continuum photosphere ($\tau \approx 2/3$) forms at a much larger radius than the physical shock wave. Therefore, the bright optical continuum observed in SNe IIn does not originate from a discrete physical shell, but rather traces this extended radiation boundary residing entirely within the unshocked CSM (Chevalier & Fransson, 1994).

This physical mechanism (illustrated in Figure 1.6) of efficient shock thermalisation provides a framework for understanding superluminous events like SN 2006gy and SN 2010jl (Smith et al., 2007; Fransson et al., 2014). The X-ray trapping in these dense environments is highly efficient; a substantial fraction of the explosion's initial kinetic energy is extracted and radiated as optical light (Chevalier & Irwin, 2011). A direct observational consequence of this profound reprocessing is that many luminous SNe IIn appear optically bright yet X-ray faint at early epochs, as the dense, unshocked CSM completely absorbs and thermalises the hard radiation before it can escape (Ofek et al., 2013).

1.4.3 Electron Scattering and Line Formation

The scattering process described in the previous section is highly conservative. Unlike the absorption and thermalisation that drives X-ray reprocessing in the inner CSM, the outer electron-scattering envelope acts as a nearly conservative scatterer: photons change direction and frequency but are rarely destroyed (Chugai, 2001; Huang & Chevalier, 2018).

This conservative scattering is the physical mechanism behind the broad emission line wings. Historically, the extreme broad base of Hα which can exhibit full widths of $\sim 20,000$ km s^{-1} was attributed to the kinematics of a physically separate, fast-moving region of SN ejecta (Schlegel, 1990). However, when a narrow-line photon emitted near the shock front attempts to escape through the opaque, hot electron gas of the unshocked CSM, it undergoes multiple Thomson scatterings. With each collision, the photon's frequency is slightly shifted via the thermal Doppler effect. This continuous diffusion and accumulation in frequency space transforms the originally narrow emission line into the broadly extended profile with prominent scattering wings observed in SNe IIn (Chugai, 2001).

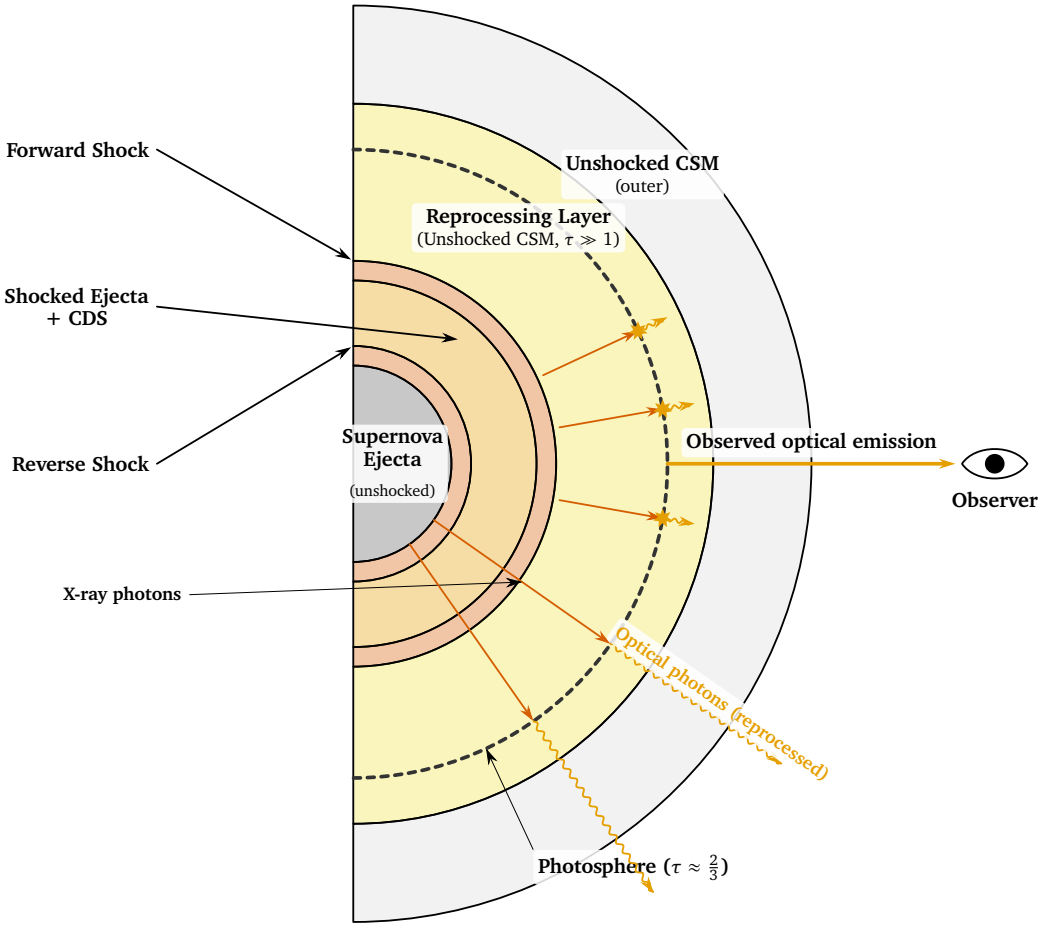

Figure 1.6: Schematic figure of the reprocessing mechanism in a Type IIn SN. X-ray photons generated at the shock front (straight arrows) are thermalised within the optically thick CSM and re-emitted as optical radiation (wavy arrows). The resulting photosphere ($\tau \approx 2/3$, dashed arc) forms inside the unshocked CSM rather than at the shock front or in the ejecta. Visual layout and conceptual geometry adapted from Smith et al. (2008a) and Dessart et al. (2015)

.

As the observed spectra are shaped by radiative transfer effects rather than simple kinematic processes, conventional analytical models prove inadequate. Accurately modelling these multi-scattering radiative transfer effects requires advanced numerical radiative transfer codes — the methodologies of which are described in Chapter 3.

Chapter 2

Circumstellar Environments and Asymmetry

The radiative phenomena outlined in the previous Chapter are the direct result of the core collapse of a massive star. However, the physical environment in which these events occur is formed long before the core collapses. The focus of this chapter shifts from the explosion of the SN to the progenitor systems themselves. Through an examination of the various mass-loss regimes of massive stars, the disruptive impact of binary companions, and the resulting asymmetrical geometries of the expelled material, this Chapter reveals the inherently multidimensional structure of the CSM.

2.1 Progenitor Stars and Mass-Loss Regimes

The dense CSM is shaped by the star's mass-loss history prior to the explosion. Therefore, understanding interacting SNe requires identifying the specific stellar channels capable of expelling extreme quantities of mass prior to core collapse. As established in Section 1.3, the primary progenitor candidates (RSGs, LBVs, WR stars and BSGs) exhibit drastically different mass-loss histories, which govern the density profile of the CSM.

The baseline case for massive star mass loss is the steady wind of a RSG, with typical steady mass-loss rates of $\dot{M} \sim 10^{-6}$ to $10^{-5}\,M_{\odot}\,\mathrm{yr}^{-1}$ (reaching an upper limit of $\sim 10^{-4}\,M_{\odot}\,\mathrm{yr}^{-1}$), and velocities of $v_w \sim 10$ to $20\,\mathrm{km\,s}^{-1}$ (Smith, 2014). This continuous outflow builds up over the late stages of stellar evolution to form a vast circumstellar envelope that can extend to radii of 10^{17} to 10^{18} cm (Smith, 2014). The standard steady-wind profile is defined by the continuity equation

$$\rho(r) = \frac{\dot{M}}{4\pi r^2 v_w}\,. \tag{2.1}$$

This implies the standard density decline $\rho \sim r^{-2}$ that is expected for a stationary stellar wind. As the mass-loss rate is relatively low, the extended CSM remains optically thin. When the ejecta encounters this medium, the result is the weak, short-lived interaction signatures that are characteristic of standard Type IIP or transitional IIP-IIn SNe. The lower physical boundary of the CSM parameter space is therefore established by the steady RSG wind. However, these mass-loss rates are several orders of magnitude too low to supply the extreme, optically thick environments required to power luminous SNe IIn (Smith, 2014).

LBVs occupy an intermediate mass-loss regime during their standard, non-eruptive S Doradus variability phases. In this state, they produce dense stellar winds with mass-loss rates of $\dot{M} \sim 10^{-5}$ to $10^{-4} M_{\odot}$ yr^{-1} and terminal velocities of $v_w \sim 100$ to 500 km s^{-1} (Smith, 2014). While this represents a significant increase over steady RSG winds, powering the extreme luminosity of SNe IIn requires even higher mass-loss rates. During giant eruptions, LBV mass-loss rates surge to $\dot{M} \sim 0.01 - 10\, M_{\odot}$ yr^{-1}, with outflow velocities of $v_w \sim 50 - 600$ km s^{-1} (Smith & Owocki, 2006; Smith, 2014). Because this dense material is situated extremely close to the progenitor ($\sim 10^{15}$ cm), observational constraints dictate that these eruptions must occur just years to decades prior to core collapse. The physical mechanism behind these sudden ejections remains uncertain. While classical models invoke opacity-driven super-Eddington winds (Smith & Owocki, 2006), a prominent alternative framework proposes wave-driven mass loss (Quataert & Shiode, 2012; Shiode & Quataert, 2014). In the latter scenario, vigorous convection during late-stage nuclear phases (such as neon or oxygen burning) excites internal gravitational waves. These waves propagate outward, entering the envelope as acoustic waves and thermalising near the stellar surface. The resulting energy deposition ($\sim 10^7\, L_{\odot}$) inflates the envelope, driving optically thick outflows and extreme mass-loss events that manifest as pre-SN outbursts.

The standard radiatively driven winds of WR stars are characterised by high terminal velocities ($v_w \sim 1,000 - 2,500$ km s^{-1}) and substantial mass-loss rates ($\dot{M} \sim 10^{-5.6}$ to $10^{-4.4}\ M_{\odot}$ yr^{-1}) (Crowther, 2007). However, these standard winds are too fast and steady to accumulate the dense, confined CSM shells required to power SNe Ibn (Smith, 2017). To resolve this problem, the progenitor must have experienced either envelope stripping via binary interaction or an explosive core-related event, a concept that is illustrated by the pre-explosion outburst of SN 2006jc (Pastorello et al., 2007).

Diverse mass-loss histories can be unified mathematically using the wind density parameter:

$$w = \frac{\dot{M}}{v_w}, \tag{2.2}$$

which dictates the radial density profile of the envelope as $\rho_{\mathrm{CSM}} = w/(4\pi r^2)$. This single parameter unifies the progenitor channels into a common physical framework,

as illustrated in Figure 2.1.

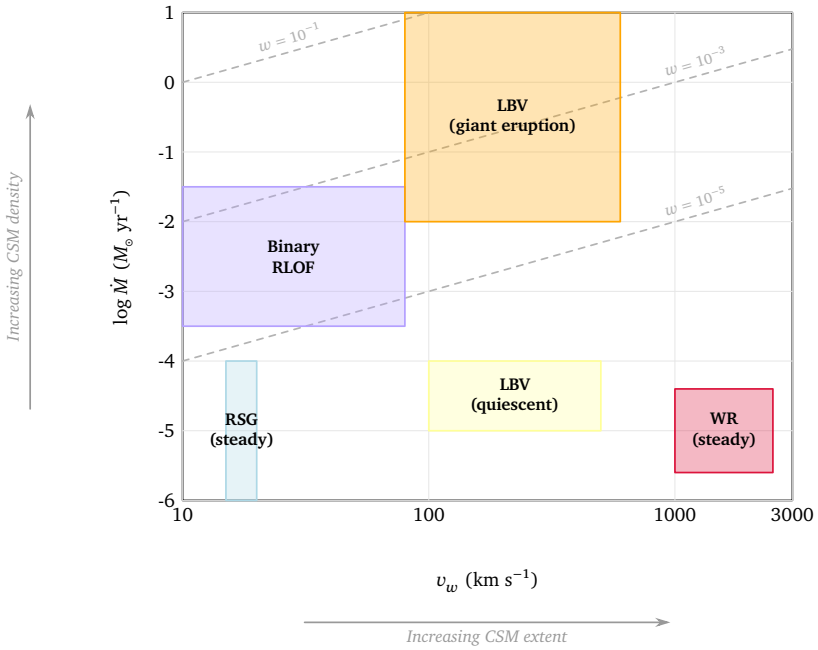

Figure 2.1: Wind parameter space for the primary progenitor channels of interacting SNe. Diagonal dashed lines denote contours of constant wind density parameter $w = \dot{M}/v_w$. Values compiled from Smith (2014) and Crowther (2007).

The spatial boundaries of the CSM provide critical constraints on the timeline of the mass loss, beyond the density of the medium. The inner radius of the CSM can be observed using flash spectroscopy. The timescales of recombination and temporal evolution of early, highly ionised emission lines can be tracked by observations of the spectra of the SN within hours of the explosion. This is before the expanding ejecta sweeps the material. Calculations based on light-travel time and the persistence of these spectral features constrain the inner radius of the dense CSM to extremely compact scales of 10^{14} to 10^{15} cm (Yaron et al., 2017; Bruch et al., 2021). The three density profiles that result from these distinct mass-loss histories are compared schematically in Figure 2.2.

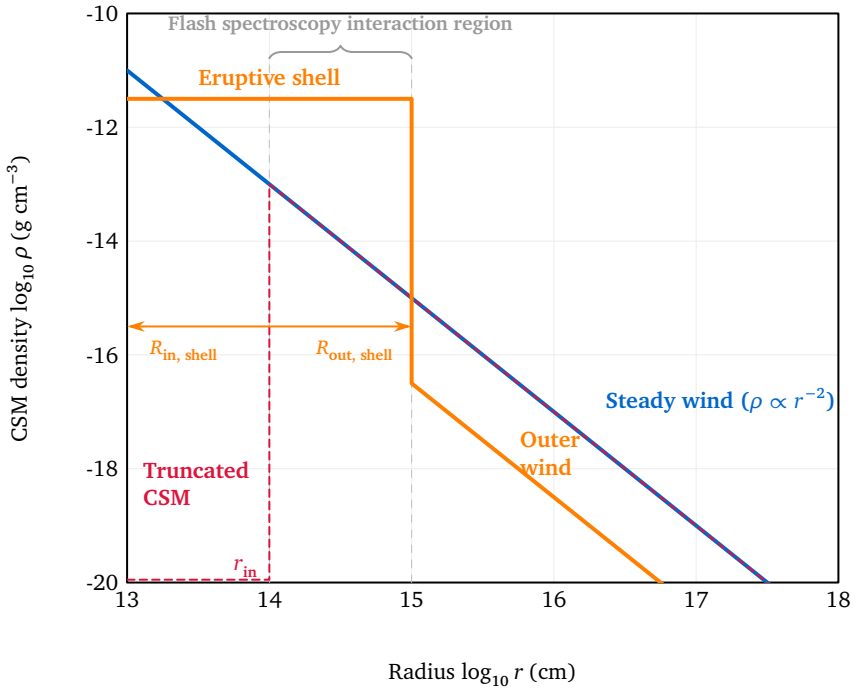

Figure 2.2: Schematic CSM density profiles for three mass-loss histories: a steady wind, a two-component eruptive shell overlying an outer wind, and a truncated profile with an inner cavity at $r_{\rm in}$ (Yaron et al., 2017; Bruch et al., 2021).

However, extracting the true mass-loss history from these observations is complicated by the mathematical degeneracies inherent in standard analytical models. When 1D is used, spherically symmetric models are utilised for fitting light curves, the derived mass-loss rate scales linearly with the assumed wind velocity ($\dot{M} \propto v_w$). Altering the velocity assumption can shift the inferred mass-loss rate by an order of magnitude while producing an identical fit to the observed optical depth and peak luminosity (Moriya & Maeda, 2014). Furthermore, these calculations implicitly assume that the CSM is a perfect sphere. If the pre-explosion mass loss was distributed in an asymmetric, disc-like, or detached configuration, the true structure of the CSM would differ significantly from 1D predictions.

In reality, the eruptive and steady mass-loss processes described in this section are rarely spherically symmetric. Understanding the physical origin of these complex geometries requires looking beyond isolated stellar winds to consider the progenitor's angular momentum budget and the highly disruptive influence of a binary companion.

2.2 Binary Interaction and Progenitor Stripping

Observations of galactic populations indicate that more than 71% of all stars more massive than $\sim 15\ M_\odot$ will exchange mass with a binary companion during their lifetimes (Sana et al., 2012). Because these interactions are the norm, the influence of a companion must be integrated into models of pre-SN mass loss. The necessity of this paradigm is evident when examining stripped-envelope progenitors, such as WR stars. Forming a WR star via standard single-star stellar winds requires a massive progenitor (> 25 to $30\,M_\odot$). In contrast, binary envelope stripping is efficient also at much lower initial masses (~ 10 to $60\,M_\odot$). Population synthesis models show that this stripping channel is required to match the observed rates of stripped-envelope SNe (Yoon et al., 2010; Claeys et al., 2011; de Mink et al., 2014).

During this phase, the hydrogen envelope is stripped and transferred to the companion, leaving behind a bare helium core. While this process establishes the standard progenitor for a Type Ib SN (Podsiadlowski et al., 1992), the specific observational signatures of a Type Ibn event require the formation of a dense CSM. Therefore, the stripped helium core must undergo subsequent, extreme mass-loss episodes shortly before core collapse to generate the necessary interacting environment.

If the initial mass ratio is extreme, or if the stripped primary undergoes a subsequent phase of expansion, mass transfer can become dynamically unstable. The system then enters the Common envelope (CE) phase. The companion spirals into the envelope of the primary star, depositing immense orbital energy into the surrounding gas via dynamical friction. This thermalised energy unbinds and ejects the entire envelope on a dynamical timescale of months to years, which is shorter than steady wind accumulation. The energy budget of this ejection is parameterised using the standard energy formalism, equating the energy required to disperse the envelope, $E_{\rm bind}$, to the change in the binary's orbital energy, $\Delta E_{\rm orb}$, scaled by an efficiency parameter $\alpha_{\rm CE}$,

$$E_{\rm bind} = \alpha_{\rm CE} \Delta E_{\rm orb}\,. \tag{2.3}$$

Because the process is not perfectly efficient, $\alpha_{\rm CE}$ represents the fraction of dissipated orbital energy actually utilised to eject the envelope. Due to unaccounted energy sources such as recombination and accretion, the exact energy budget remains subject to theoretical uncertainty (Ivanova et al., 2013; MacLeod et al., 2017).

Binary influences can also drive mass loss prior to, or in the absence of, direct Roche Lobe Overflow (RLOF). The gravitational pull of a close companion transfers orbital angular momentum, tidally spinning up the primary star. This induced rotation lowers the effective surface gravity at the equator, facilitating mass loss directed towards the orbital plane (de Mink et al., 2014).

2.3 Formation Mechanisms of Asymmetric CSM

When an isolated massive star rotates rapidly, centrifugal forces deform it into an oblate shape, lowering the effective surface gravity at the equator. While older models assumed this produced a slow equatorial disc, modern radiative wind models demonstrate that the driving flux is weakest at the equator. Consequently, the mass-loss rate and wind velocity reach their maxima at the poles (Dwarkadas & Owocki, 2002). The outflow of an isolated rotating star naturally expands into a prolate shape. This geometry can be inverted if the gravity-darkened equator cools below the bi-stability jump ($\sim 25,000\,\mathrm{K}$). In this cooler region, the recombination of ions drastically increases the local line-driving efficiency, triggering a dense, slow-moving outflow that forms an equatorial disc (Vink et al., 2001)

This polar-enhanced geometry cannot explain the dense, confined equatorial structures inferred for most interacting SNe. Instead, the binary stripping mechanisms described previously provide the necessary physical framework to generate these asymmetric environments, as illustrated in Figure 2.3.

When material escapes through the L_2 point (the outer Lagrangian saddle point lying on the common rotational axis) during RLOF, the outflowing gas carries the specific angular momentum of the binary orbit. It is continuously torqued and assembles into a dense circumbinary torus in the orbital plane (Pejcha et al., 2016). Similarly, if the binary ejects its envelope during the CE phase, the expelled mass is concentrated along the equator. Although this CE ejecta aligns with the orbital plane, it is geometrically thick due to vertical isothermal expansion as it leaves the system (MacLeod et al., 2017). Unlike the polar winds of single stars, these direct binary interactions produce the geometrically thick, dense equatorial tori required to power luminous transients.

A more complex geometry arises when mass loss is directed along the polar axis by binary-driven jets, while maintaining a dense equatorial waist. The Homunculus nebula of η Carinae exemplifies this structure. Shaped by binary interactions during a giant eruption, the nebula contains roughly $10\,M_\odot$ of material. The bulk of this mass resides in fast-expanding polar lobes (~ 650 km s^{-1}), while the equatorial torus expands much slower but remains exceptionally dense (Smith et al., 2003). If an SN shocks were to expand into such an environment, the interaction physics would depend entirely on the viewing angle.

These binary-driven processes—whether through L_2 mass loss, CE ejection, or eruptive waists—are the primary drivers of dense equatorial mass concentrations. They lead to the formation of a dense equatorial disc or torus embedded within a more diffuse, approximately spherical outer wind. This specific two-component geometry is the standard configuration implemented in the CASTRO 2D RHD models presented in Chapter 5.

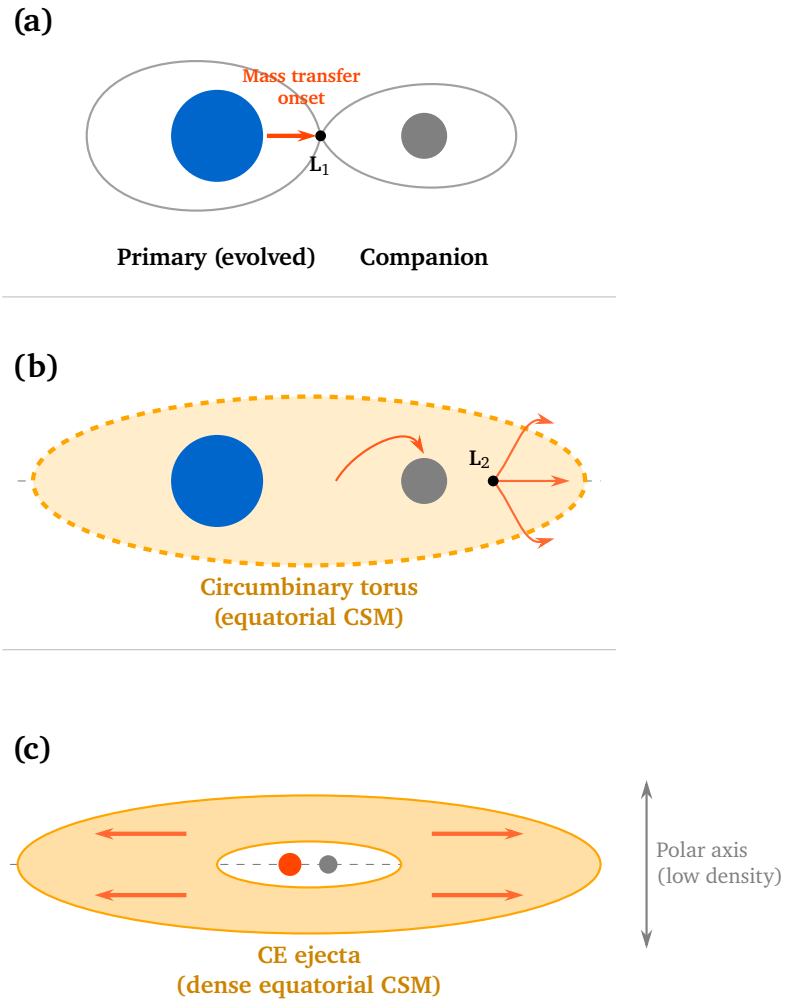

Figure 2.3: Schematic representation of binary interaction channels producing asymmetric CSM. (a) Roche lobe overflow onset at L_1; (b) mass ejection through L_2 forming a circumbinary equatorial torus; (c) CE ejection producing a dense equatorial structure with a low-density polar axis. Visual geometry synthesised from the standard binary interaction schematics of Ivanova et al. (2013) and Smith (2014), based on the theoretical mass-loss frameworks of Pejcha et al. (2016) and MacLeod et al. (2017).

2.4 Observational Evidence for CSM Asymmetry

Spectropolarimetry serves as a direct diagnostic tool for determining the geometry of circumstellar environments. In a perfectly spherical medium, scattering by free electrons yields zero net linear polarisation. Therefore, any measured continuous polarisation signal directly indicates a departure from spherical symmetry, such as the presence of an equatorial disc or bipolar outflow (Wang & Wheeler, 2008; Patat et al., 2011). While this technique provides geometric constraints for interacting SNe, the

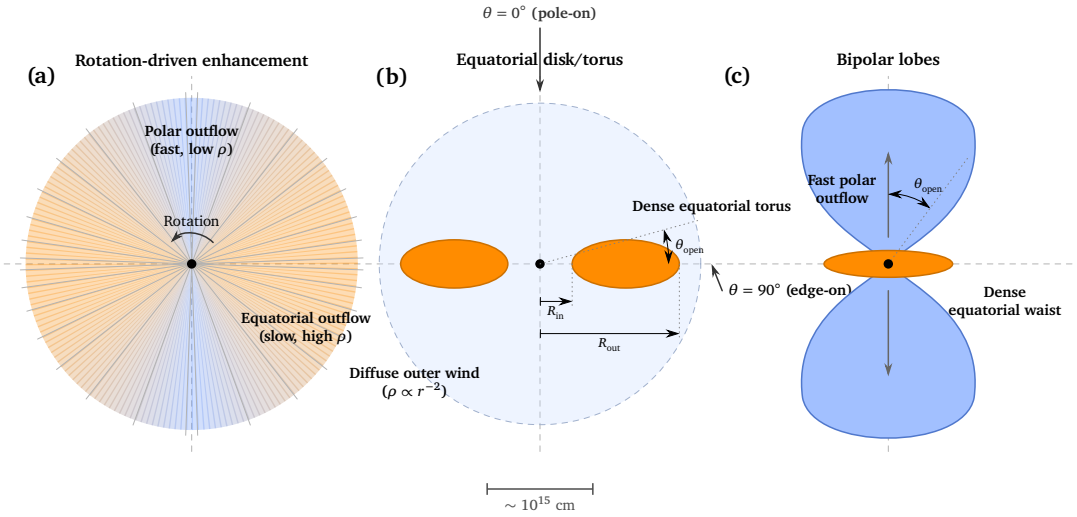

Figure 2.4: Schematic CSM geometries produced by the mass-loss mechanisms discussed in this Chapter. (a) Rotation-driven equatorial density enhancement; (b) equatorial disc/torus embedded in a diffuse outer wind, with viewing angle θ and torus half-opening angle $\theta_{\rm open}$ indicated; (c) bipolar lobe geometry with a dense equatorial waist. Orange colour denotes dense, slow material; blue colour denotes fast, low-density outflow. Scale bar is representative of the inner CSM radius. Visual geometries synthesised from the theoretical frameworks of Dwarkadas & Owocki (2002) for rotating winds, and Smith (2014) for eruptive and binary-driven mass loss.

radiative transfer models presented in this work focus exclusively on synthetic photometry and standard spectroscopy.

The asymmetric CSM imprints directly on emission line profiles. Departures from standard symmetry—such as multi-component profiles, blueshifted emission peaks, or suppressed wings—indicate significant geometric or optical depth asymmetries. In systems with a disc or torus geometry, the observed line profile depends heavily on inclination. An edge-on torus typically blocks specific velocity slices of the expanding gas, producing broader, multi-peaked emission profiles, whereas a pole-on geometry yields narrower, single-peaked lines. The evolution of SN 2009ip demonstrates this behaviour of spectral lines. During the interaction, the Hα profile exhibited a narrow emission core, broad Thomson-scattered wings and persistent asymmetric structures, including fast-moving blueshifted absorption and late-time flux imbalances. These complex, multi-component line profiles can be naturally interpreted as resulting from geometric asymmetries—such as an inclined disc-like structure or asymmetric dust formation within the ejecta (Margutti et al., 2014; Graham et al., 2014).

In the situation, where the CSM were smooth and spherical, the interaction luminosity would decline monotonically as the shock wave swept through the lower-density material. However, the observed light curves of interacting SNe show the opposite: un-

expected re-brightenings and plateaus. These features can be explained by the shock running into regions of increased density, such as dense shells or clumps. For instance, Type Ibn SN 2006jc initially exhibited a rapid decline, but at around 25 days after reaching maximum brightness, its optical light curve formed a plateau accompanied by a re-brightening in the near-infrared. This behaviour is consistent with the SN ejecta colliding with a dense, helium-rich shell cast off during a previous outburst. After 55 days, the optical light curve resumed a rapid decline, a feature primarily attributed to the condensation of dust within the cooling post-shock gas, combined with the shock traversing the finite dense shell (Foley et al., 2007; Smith et al., 2008b).

Direct imaging of nearby nebulae prior to explosion provides geometric evidence of asymmetric structure. The Homunculus nebula of η Carinae is the best example, as thermal-infrared observations can directly map its mass distribution and measure the density contrast between the equatorial waist and the poles. As a result, it was confirmed that the vast majority of the nebula's mass is in the polar lobes (Smith et al., 2003). Together, these observational diagnostics confirm that departures from spherical symmetry are an inherent feature of interacting transients, strictly limiting the utility of 1D hydrodynamic models. Traditional 1D models are inherently unable to capture these viewing-angle-dependent signatures, which motivates the use of multi-dimensional hydrodynamic simulations, which are presented in subsequent chapters.

Chapter 3

Computational Tools and Theoretical Frameworks

3.1 CASTRO RHD Code

Simulations of the highly energetic, compressible fluid dynamics of the SN explosion used the CASTRO code. Developed at Lawrence Berkeley National Laboratory, it is an advanced, multidimensional Eulerian hydrodynamics code specifically engineered for astrophysical flows (Almgren et al., 2020; Zhang et al., 2011).

To accurately model the interaction between the gas and the radiation field, the simulations employed CASTRO's Gray radiation solver. Although an even more accurate treatment could be achieved using a multigroup solver to discretise the radiation by frequency, the Gray solver provides a sufficient approximation for the scope of this study. Assuming local thermodynamic equilibrium, the foundational mixed-frame, frequency-integrated RHD equations solved by the code, correct to $\mathcal{O}(v/c)$, are written as (Zhang et al., 2011; Mihalas & Klein, 1982):

$$\frac{\partial \rho}{\partial t} + \nabla \cdot (\rho \mathbf{u}) = 0\,, \tag{3.1}$$

$$\frac{\partial (\rho \mathbf{u})}{\partial t} + \nabla \cdot (\rho \mathbf{u}\mathbf{u}) + \nabla p = \frac{1}{c}\chi_{\mathrm{F}}\mathbf{F}_{\mathrm{r}}^{(0)} - \kappa_{\mathrm{P}}\left(\frac{\mathbf{u}}{c}\right)(aT^4 - E_{\mathrm{r}}^{(0)}) + \mathbf{f}_{\mathrm{ext}}\,, \tag{3.2}$$

$$\frac{\partial (\rho E)}{\partial t} + \nabla \cdot (\rho E \mathbf{u} + p\mathbf{u}) = -c\kappa_{\mathrm{P}}(aT^4 - E_{\mathrm{r}}^{(0)}) + \chi_{\mathrm{F}}\left(\frac{\mathbf{u}}{c}\right) \cdot \mathbf{F}_{\mathrm{r}}^{(0)} + \mathbf{u} \cdot \mathbf{f}_{\mathrm{ext}}\,, \tag{3.3}$$

$$\frac{\partial E_{\mathrm{r}}}{\partial t} + \nabla \cdot \mathbf{F}_{\mathrm{r}} = c\kappa_{\mathrm{P}}(aT^4 - E_{\mathrm{r}}^{(0)}) - \chi_{\mathrm{F}}\left(\frac{\mathbf{u}}{c}\right) \cdot \mathbf{F}_{\mathrm{r}}^{(0)} \tag{3.4}$$

$$\frac{1}{c^2}\frac{\partial \mathbf{F}_{\mathrm{r}}}{\partial t} + \nabla \cdot \mathbf{P}_{\mathrm{r}} = -\frac{1}{c}\chi_{\mathrm{F}}\mathbf{F}_{\mathrm{r}}^{(0)} + \kappa_{\mathrm{P}}\left(\frac{\mathbf{u}}{c}\right)(aT^4 - E_{\mathrm{r}}^{(0)})\,. \tag{3.5}$$

Here, ρ, $\mathbf{u}$, p, and E represent the gas density, velocity, thermal pressure, and total specific energy, respectively. The radiation field in the comoving frame is described

by its energy density $E_{\rm r}^{(0)}$ and flux $\mathbf{F}_{\rm r}^{(0)}$, while E_r, $\mathbf{F}_{\rm r}$, and $\mathbf{P}_{\rm r}$ denote the mixed-frame radiation energy, flux, and pressure tensor. The coupling between the gas and radiation is governed by the Planck mean opacity ($\kappa_{\rm P}$) and the flux-mean opacity ($\chi_{\rm F}$). Under the Gray radiation approximation, opacity is assumed to be independent of frequency, meaning the Planck mean opacity becomes mathematically equivalent to the Rosseland mean opacity ($\kappa_{\rm P} = \kappa_{\rm R}$).

3.1.1 Specific Numerical Features

To ensure numerical stability during the shockwave's evolution and its transition between stages under extreme physical conditions, two specific features of CASTRO's Piecewise Parabolic Method (PPM) solver were utilised.

The Dual Energy Formalism was employed to maintain thermodynamic stability. In hypersonic flows, where the kinetic energy of the ejecta exceeds the internal thermal energy by several orders of magnitude, standard total energy conservation calculations suffer from severe floating-point cancellation. This loss of numerical precision can lead to unphysical negative temperatures. To resolve this, the dual energy formalism solves an auxiliary advection equation purely for the internal energy in regions of extreme velocity, safely bypassing the unstable calculation (Almgren et al., 2010; Bryan et al., 2014).

To prevent the artificial numerical oscillations that frequently arise from the sharp discontinuities between the fast-moving ejecta and the dense CSM, **Shock Flattening** was utilised. This algorithm dynamically degrades the spatial reconstruction order specifically at the shock fronts, ensuring that the macroscopic shock structure remains mathematically stable and monotonic as it propagates through the grid (Almgren et al., 2010; Fryxell et al., 2000).

3.1.2 Grid Configuration and Boundary Conditions

The simulations were performed in a 2D cylindrical coordinate system (r, z). To close the hydrodynamic equations, the simulations utilised an ideal monatomic gas equation of state (the `gamma_law` EOS), characterised by an adiabatic index of $\gamma = 5/3$. In this regime, the EOS calculates the thermal gas pressure, while the RHD solver independently tracks and applies the dominant radiation pressure.

To capture the macroscopic dynamics of the interaction, the computational space was discretised onto a single-level uniform grid comprising 1024×2048 cells ($r \times z$). Because the physical scale of the SN ejecta expands by several orders of magnitude over time, the physical dimensions of the computational domain were scaled dynamically. Specifically, during each reinitialisation, the domain boundaries were expanded by a factor of two to capture the evolutionary stage and the specific CSM geometry being

modelled:

- **Equatorial Disc Models:** The early-stage (Part 1) domain spanned $r \in [0, 3.475 \times 10^{14}]$ cm and $z \in [-3.475 \times 10^{14}, 3.475 \times 10^{14}]$ cm. For the final evolutionary stages, these boundaries were expanded to $r \in [0, 5.69 \times 10^{18}]$ cm and $z \in [-5.69 \times 10^{18}, 5.69 \times 10^{18}]$ cm.
- **Bipolar Lobe Models:** The initial domain spanned $r \in [0, 4.0 \times 10^{14}]$ cm and $z \in [-4.0 \times 10^{14}, 4.0 \times 10^{14}]$ cm. To capture the late-stage expansion, these boundaries were extended up to $r \in [0, 3.28 \times 10^{18}]$ cm and $z \in [-3.28 \times 10^{18}, 3.28 \times 10^{18}]$ cm.

The computational domain was configured with strict boundary conditions for both the gas dynamics and the radiation field. Hydrodynamically, a reflecting symmetry boundary was enforced along the central z-axis ($r = 0$). Standard zero-gradient outflow boundaries were applied to the outer radial edge and both vertical limits, enabling the expanding gas to freely exit the domain. Vacuum outflow conditions were set for the radiation boundaries to ensure that escaping photon flux leaves the computational domain without undergoing artificial numerical reflection.

3.2 SIROCCO Radiative Transfer Code

Although the CASTRO simulations successfully capture the complex, multidimensional fluid dynamics and thermodynamic evolution of the interacting SN, the hydrodynamics solver cannot generate the detailed electromagnetic observables required for comparison with empirical observations. As established previously, CASTRO employs the Gray Flux-Limited Diffusion (FLD) approximation, which pre-integrates the radiation field over all frequencies to save computational time. Consequently, this approximation discards the detailed wavelength-dependent information and angular scattering physics required to generate spectra.

To connect the 2D RHD simulations with observable data, Monte Carlo Radiative Transfer (MCRT) codes are required. In this study, the open-source MCRT code SIROCCO (Matthews et al., 2025) was utilised. SIROCCO takes the mapped grid of physical macroscopic quantities from CASTRO—specifically density, temperature, and velocity components—and calculates the emergent radiation field. However, the mass fractions of individual species calculated during the RHD simulation are not imported into SIROCCO; instead, the code relies entirely on its own comprehensive internal atomic data libraries to define the elemental composition and independently calculate the detailed ionisation balance.

3.2.1 Monte Carlo Radiative Transfer and the Sobolev Approximation

To generate spectra and light curves, SIROCCO must solve the radiative transfer equation. Because solving this equation analytically across a multidimensional grid is computationally impractical, the MCRT method is used instead. Rather than calculating specific intensities, the continuous radiation field is divided into a vast number of indivisible energy packets (Long & Knigge, 2002; Matthews et al., 2025). The code tracks two distinct types: r-packets represent bundles of radiant photon energy, and k-packets represent the internal thermal kinetic energy of the gas. The probabilistic tracking of these packets, along with their continuous transformation between radiation and thermal energy, naturally enforces global energy conservation while capturing complex scattering events.

As r-packets travel through the expanding computational grid, their interactions with bound-bound atomic transitions (spectral lines) are governed by the Sobolev approximation (Sobolev, 1960). In an SN environment, macroscopic expansion velocities reach approximately 10^4 km s^{-1}, which is several orders of magnitude larger than the microscopic thermal velocities of the gas particles. Because of this, as a photon travels through the ejecta, the continuous expansion creates a strong Doppler shift, causing the photon to sweep across the rest-frame frequencies of the local atomic transitions.

Because of the severe velocity gradient, the interaction between a photon packet and a specific spectral line is not continuous. Instead, it is restricted to a very narrow spatial volume known as the resonance region. The Sobolev approximation exploits this by assuming that the macroscopic properties of the gas, such as density and temperature, remain constant across this microscopic resonance length. This simplifies the radiative transfer problem: it collapses the computationally expensive non-local optical depth integrals into a purely local algebraic calculation that depends almost entirely on the local velocity gradient ($\mathrm{d}v/\mathrm{d}r$). By treating line interactions as strictly localised point events, the code can efficiently process millions of photon packets through a complex, expanding medium.

3.2.2 Radiative Transfer Modes and the Macro-Atom Formalism

Because the computational domain encompasses the expanding SN ejecta, the dense CSM, and the unshocked stellar wind, physical properties such as density and optical depth vary by several orders of magnitude. To manage the immense computational cost of Monte Carlo tracking across these distinct regimes, SIROCCO allows for different radiative transfer modes.

In the deep, optically thick regions of the grid, tracking individual photon packets is computationally prohibitive due to the extreme number of scattering events. To

resolve this, a thermal trapping approximation is utilised. Packets located in regions exceeding a specified optical depth threshold are considered trapped by the dense medium. Instead of simulating individual scatters, the code advects these packets outward at the macroscopic velocity of the gas until they cross into an optically thin region, where standard probabilistic tracking resumes.

While thermal trapping provides a practical framework for calculating energy diffusion, generating detailed spectral lines requires a rigorous treatment of atomic physics. For these calculations, SIROCCO employs the macro-atom formalism (Lucy, 2002, 2003). This approach reformulates the transport of radiation as a statistical flow of energy through various atomic energy levels. When a photon packet is absorbed, it transitions the macro-atom to an excited state. The atom then undergoes a series of internal transitions before decaying and emitting a new packet.

By treating the atoms as energy reservoirs rather than simple scattering targets, the macro-atom formalism ensures strict global energy conservation. Furthermore, it provides an accurate physical treatment of non-local thermodynamic equilibrium (NLTE) effects, which are essential for forming the emission and absorption lines seen in the synthetic spectra. Because this study serves as an initial application of SIROCCO to these specific interacting models—aimed at understanding the capabilities and limitations of the pipeline—the hybrid `macro_atom_thermal_trapping` mode was selected. This configuration successfully balances the computational efficiency required for the dense interior with the detailed quantum mechanical calculations necessary for the observable outer layers.

3.2.3 Configuration

To generate the final synthetic observables, the hydrodynamic output from CASTRO was mapped onto the SIROCCO grid using the conversion routines detailed in Section 4.2.2. To manage the immense computational expense of the Monte Carlo tracking, the spatial resolution of the input data was coarsened. For the pseudo-bolometric light curve calculations, the grid was coarsened by a factor of 4. Because the full NLTE macro-atom treatment required for spectral lines is significantly more computationally intensive, the grid was coarsened further by a factor of 8 for the specific spectral line analysis to ensure tractable execution times. The hydrodynamic profiles were extracted at targeted times, to capture the critical phases of the shock interaction. For the radiative transfer calculations, the macro-atom formalism was configured to focus primarily on the transitions of hydrogen and helium, which are the dominant elements governing the interaction signatures in these models.

The primary outputs of the SIROCCO pipeline are viewing-angle-dependent synthetic spectra, which were extracted over targeted wavelength ranges to capture the essential emission lines. To construct the pseudo-bolometric light curves, these angle-

dependent spectra were integrated over the full calculated wavelength range to yield the total emergent flux. By utilising SIROCCO's multi-angle tracking, the resulting synthetic light curves and spectra directly reflect the geometric asymmetries of the simulated circumstellar environment.

3.3 Analytical CSM

The 1D model of an SN undergoing shock breakout from SNEC (Morozova et al., 2015) is augmented with an analytical unshocked CSM during initialisation, specifically its density and velocity profiles. Routines were adapted from the interaction framework developed by Kurfürst et al. (2020). The baseline environment for all models is a steady, spherically symmetric background wind. This unperturbed medium obeys the standard continuity equation

$$\rho_{\text{wind}} = \rho_{0,\,\text{wind}} \left(\frac{R_\star}{r} \right)^2 , \tag{3.6}$$

where $R_\star$ is the progenitor radius, $\rho_{0,\,\text{wind}}$ is the density evaluated near the stellar surface, and r is the radial distance. This profile assumes a constant mass-loss rate of $\dot{M}_{\text{wind}} = 10^{-6}\, M_\odot\, \text{yr}^{-1}$ expanding at a terminal velocity of $v_{\text{wind}} \approx 15\,\text{km}\,\text{s}^{-1}$, typical of an RSG phase.

3.3.1 Equatorial Disc

The CSM is then added to the background wind. To simulate mass loss, which leads to an asymmetric equatorial disc structure, the parameterisation formulated by Kurfürst et al. (2020) is utilised. The disc-like enhancement is injected into the grid using exponential decay from the orbital midplane

$$\rho_{\text{disc}} = \rho_{0,\,\text{disc}} \left(\frac{R_\star}{r} \right)^w \exp\left[\frac{2\left(\sin\theta - 1\right)}{\left(H/r\right)^2} \right] . \tag{3.7}$$

In this formula, θ represents the polar angle, placing the midplane at $\theta = \pi/2$, and $w = 2$ dictates the radial density decline. To emulate the extreme mass overflow from a binary companion, the base density is overscaled to $\rho_{0,\,\text{disc}} \approx 4 \times 10^{-9}\,\text{g}\,\text{cm}^{-3}$.

The vertical thickness of this structure is influenced by the scale height $H = c_S/\Omega$ (Kurfürst et al., 2020; Kurfürst & Krtička, 2019). The Keplerian angular velocity is defined as $\Omega = \sqrt{GM_\star/r^3}$ at a cylindrical radius r. The local sound speed, c_S, is derived from an assumed effective temperature of the progenitor of 4, 000 K, following a shallow power-law decline (approximately $r^{-0.4}$) outward through the disc.

3.3.2 Bipolar Lobes

Modelling bipolar geometries analogous to the Homunculus nebula of η Carinae requires a distinct computational approach. Rather than being distributed in a continuous equatorial disc, the mass is distributed into discrete, highly collimated eruptive shells. By employing a grid reinitialisation routine, the lobes can be simulated using spatial parameters derived directly from present-day observations. These structures are divided into a primary giant eruption (the Homunculus) and a secondary minor eruption (the Little Homunculus). Based on strict observational constraints (Smith et al., 2003; Smith, 2005, 2006), the primary Homunculus shell is prescribed onto the grid with an outer polar radius of 3.5×10^{17} cm and an inner radius of 3.1×10^{17} cm. The Little Homunculus is initialised further inward, defined by polar boundaries between 7.2×10^{16} cm and 8.2×10^{16} cm.

To enforce the prolate geometry of the lobes, both the radial boundaries and the velocity field of the ejected material must be strictly latitude-dependent. An angular modulation function, $F(\theta)$, was applied to shape the shells:

$$F(\theta) = \frac{v_{\mathrm{eq}}/v_{\mathrm{polar}} + \exp(2\lambda \cos(2\theta))}{1 + \exp(2\lambda \cos(2\theta))}, \tag{3.8}$$

where λ acts as a dimensionless collimation parameter, and v_{eq} and v_{polar} define the equatorial and polar expansion velocities, respectively, for a given eruptive phase. The local outflow velocity at any point in the domain is dictated by $v(\theta) = v_{\mathrm{polar}} F(\theta)$.

The corresponding gas density is intrinsically linked to this modulated velocity field via the continuity equation:

$$\rho(r, \theta) = \frac{\dot{M}}{4\pi r^2 v(\theta)}. \tag{3.9}$$

To ensure that the erupted mass remains physically confined to a bipolar shape, the radial placement of the shells at any given latitude is scaled by the identical modulation function. This yields the boundary condition $r_{\mathrm{in}} F(\theta) \leq r \leq r_{\mathrm{out}} F(\theta)$ (Kurfürst et al., 2020).

Chapter 4

Custom Simulation Tools

4.1 Reinitialisation of 2D RHD Simulation in Castro

In previous models of interacting SNe, such as those presented by Kurfürst et al. (2020) or Holoubek (2024), the simulations relied on a single massive grid with fine resolution to capture both the small-scale shock breakout and the extended CSM simultaneously. This procedure was computationally demanding. A more practical approach is to start with a small, high-resolution grid for the initial stages of the simulation and then pause it when the shock approaches the domain boundary. The physical domain is then expanded and reinitialised with the results of the previous simulation remapped onto it.

CASTRO has a built-in tool for domain expansion called the checkpoint embiggener. However, this tool only works for pure gas hydrodynamics; it does not support radiation. Due to this limitation, the aim was to develop a custom routine that could safely map both hydrodynamic and radiation variables onto a newly expanded grid and restart the simulation.

4.1.1 Initiation and Data Ingestion

The reinitialisation process begins with the `problem_initialize.H` CASTRO module, which reads the global analytic parameters for the far-field CSM and manages the `plotfile_data.H` reading module to load data from the previous simulation. This enables the 2D model to be loaded as input for the simulation instead of relying on the classic CASTRO module (`model_parser.H`). The native approach to restarting a simulation is via a checkpoint that contains the complete internal state required to seamlessly resume a paused run. However, by developing a method to restart directly from a plotfile, the framework gains spatial flexibility. From CASTRO's perspective, this means the overall evolution is treated as a series of separate simulations rather than one continuous run. A direct consequence of this method is that the internal simulation

time resets to zero in every new segment. To ensure precise temporal synchronisation across different reinitialisation phases, the elapsed simulation time was tracked manually and cumulatively aggregated during the post-processing and diagnostic phases. This tracking guaranteed that all resulting light curves, kinematic profiles, and hydrodynamic graphs remained accurately synchronised with the true physical age of the interacting SN. During the data loading phase, species' partial densities are converted into mass fractions. This normalisation prevents severe floating-point errors during interpolation, ensuring numerical stability.

Because the plotfile contains millions of spatial points, a standard array-based interpolation search would be computationally prohibitive and would require excessive memory. To solve this problem, a memory-optimised linked list spatial index—commonly referred to as the cell-linked list method (Hockney & Eastwood, 1988)—is constructed, in which the physical domain is divided into a regular grid of bins. Each data point is assigned to a specific bin, and dedicated arrays track the first point in a bin and link to the next point within the same bin. This custom approach drastically reduces peak memory usage and accelerates all subsequent spatial queries.

In order to map the old data onto the new grid cells, which are twice as coarse, the code identifies the closest original data points. This is handled by the `get_nearest_index` search algorithm (Script A.1). When a physical query coordinate (r, z) from the new grid is provided, the algorithm calculates its corresponding integer spatial bin (i_r, i_z) using the physical domain bounds $(r_{\min}, z_{\min})$ and the bin dimensions $(\Delta r, \Delta z)$:

$$i_r = \left\lfloor \frac{r - r_{\min}}{\Delta r} \right\rfloor, \quad i_z = \left\lfloor \frac{z - z_{\min}}{\Delta z} \right\rfloor . \tag{4.1}$$

The algorithm then searches the immediate 3×3 bin neighbourhood. To account for the geometric compression of grid points near the symmetry axis, which can cause points to be spaced further apart relative to the bin size, the maximum search distance is safely set to twice the bin diagonal. A valid point is only returned if its squared geometric distance to the target, d^2, satisfies $d^2 \leq 4 \times d^2_{\text{bin,diag}}$, where $d_{\text{bin,diag}}$ is the diagonal length of a single spatial bin. If no point is found within this radius, the cell is flagged as lying entirely outside the old simulation domain.

Once the spatial indices have been resolved, the physical variables are mapped onto the new grid cells using two distinct methods (Press et al., 2007). For loading old plotfile data, the direct nearest neighbour approach is utilised. Using the exact indices found by the spatial search algorithm, the new cell simply inherits the physical state (density, temperature, velocity, and species) of the closest original data point. This ensures the internal shock structures are transferred exactly as they were computed, preventing any artificial numerical smoothing. For specific transitions (e.g., determining the exact boundary anchor values used to blend the simulation data into the extended analytic domain), an inverse-distance weighted linear interpolation (Script A.2) is ap-

plied. Originally developed as Shepard's method, this approach scans a broader 5×5 bin neighbourhood around the target boundary coordinate (r, z). The interpolated physical value $f(r, z)$ is calculated as the weighted sum of the neighbouring points f_i:

$$f(r, z) = \frac{\sum_i w_i f_i}{\sum_i w_i} . \tag{4.2}$$

To guarantee numerical stability and prevent division-by-zero singularities when a new grid coordinate perfectly overlaps an original data point, a strict minimum threshold $\epsilon = 10^{-30}$ is added to the weight calculation. Thus, the weight w_i of each neighbouring point is inversely proportional to the square of its geometric distance d_i to the target:

$$w_i = \frac{1}{d_i^2 + \epsilon} , \tag{4.3}$$

where the squared distance from the target coordinate to the i-th neighbour is $d_i^2 = (r - r_i)^2 + (z - z_i)^2$.

4.1.2 Cell-by-Cell Hydrodynamic Mapping

Once the plotfile data has been loaded into memory and the spatial index has been constructed, the framework iterates over the newly expanded computational grid. The `problem_initialize_state_data.H` module then assigns the correct physical state to every cell by applying a three-zone geometric logic (Script A.3), that is illustrated at Figure 4.1. Density, temperature, velocity components, and species' mass fractions are determined entirely by the cell's radial distance from the origin relative to the boundaries of the previous simulation domain.

The computational domain is divided into the following three regions:

- The **Inner Zone** lies within the original simulation bounds (95% of the old domain), and the new grid cells are populated by applying interpolation schemes to the data in the loaded plotfile. This process guarantees that the highly resolved internal shock structures and complex fluid dynamics are transferred exactly as computed.

- Next is the **Transition Zone**, whose main task is to stitch the computed inner zone and the analytical outer zone together to prevent artificial numerical shocks or instabilities. Smoothing is achieved using a hyperbolic tangent blending function applied across an explicitly defined transition width, given by

$$s(d) = \frac{1}{2} \left\{ 1 + \tanh \left[6 \left(\frac{d - d_{\text{start}}}{\Delta_{\text{blend}}} - \frac{1}{2} \right) \right] \right\} , \tag{4.4}$$

where d_{start} marks the beginning of the transition region, and Δ_{blend} constitutes the outermost 5% of the original domain. The final blended physical quantity q is then calculated as $q = (1 - s)q_{\text{plotfile}} + sq_{\text{analytic}}$. This function acts as a continuous spatial weight, seamlessly merging the numerical simulation data with the analytical background gradients.

- The last region is the expanded **Outer Zone**, where no previous simulation data exist and cells must be populated analytically. For the asymmetric equatorial disc simulations, the density is defined using the same analytical method as the initial state (see Section 3.3.1). To ensure a smooth structural transition across the boundary, this analytical density is multiplied by a normalisation factor (Script A.4) derived from the plotfile boundary values:

$$\rho_{\text{outer}} = \rho_{\text{analytic}}(r, z) \times \frac{\rho_{\text{plotfile}}(r_{\text{boundary}}, z_{\text{boundary}})}{\rho_{\text{analytic}}(r_{\text{boundary}}, z_{\text{boundary}})}. \tag{4.5}$$

  Other state variables (temperature, velocity, and species) were purely extrapolated outward from the inner zone boundary using an $r^{-0.5}$ decay profile. However, extrapolating these dynamic variables often induced numerical artifacts. Consequently, a more robust, purely analytical approach was developed for the bipolar lobe models. Instead of extrapolation, the newly expanded zones are populated with fixed, physically motivated background values representing the unperturbed ambient medium (based on Section 3.3.2). Furthermore, this outer analytical domain is dynamic, incorporating shifting kinematics as the lobes continue to expand. The geometric boundaries of the bipolar shells are explicitly calculated as a function of elapsed simulation time ($r = r_0 + v \cdot t$). This approach ensures the background CSM expands consistently alongside the SN. Additionally, the chemical composition in this region is strictly set to reflect CNO-processed stellar winds (40% hydrogen and 60% helium), and a minimum ambient temperature of 100 K is enforced (Script A.5).

4.1.3 Radiation Mapping and Thermodynamic Stability

The final stage of the reinitialisation is handled by `problem_initialize_rad_data.H`, whose main task is to map the radiation energy density onto the expanded grid and inform CASTRO that radiation data is already present. Similar to the hydrodynamic variables, radiation mapping uses a three-zone geometric logic to blend highly resolved inner simulation data with the outer analytic domain.

A significant numerical challenge in RHD is that extrapolating radiation fields or temperature gradients into an empty grid can produce artificial temperature rays and numerical streaking. To eliminate these artifacts, the implementation of the bipolar

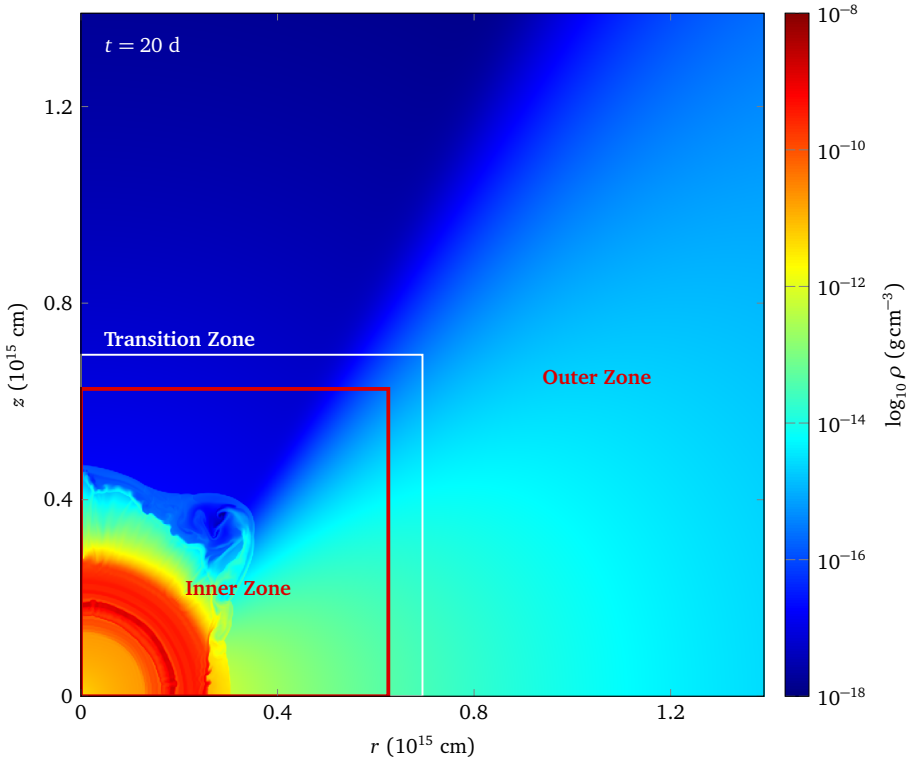

Figure 4.1: Density map at $t = 20$ d illustrating the three spatial domains of the multi-dimensional reinitialisation pipeline: the mapped Inner Zone, the smoothed Transition Zone, and the analytical Outer Zone.

lobes completely bypasses angular interpolation for the expanded outer zone. Instead, the extended domain is initialised with a pure, uniform analytic background radiation field. This field is anchored to a strict thermal equilibrium floor, which is calculated directly from the ambient gas temperature of 100 K. Enforcing this absolute thermodynamic stability in the far-field CSM prevents the radiation solver from propagating artificial fluxes before the physical shock wave reaches the newly mapped grid cells.

As a final thermodynamic safeguard across all zones, the newly mapped primitive variables (density, temperature, and mass fractions) are passed back through the CASTRO EOS before the simulation resumes (Script A.6). This step recalculates the internal and total energy densities for every cell, guaranteeing that the entirely mapped domain remains thermodynamically consistent and mathematically closed before the hydrodynamics solver is engaged.

4.1.4 Validation

To verify the correctness of the reinitialisation pipeline, a residual analysis was performed across the mapping boundaries. It is essential to confirm that transitioning the simulated state from the highly resolved grid of the previous stage (Run A) to

the newly expanded, coarser computational domain (Run B) does not introduce any unphysical macroscopic artefacts.

Validation was performed by calculating the relative residuals immediately after populating the new grid, i.e., between the plotfile used for reinitialisation and the plotfile outputted at simulation time $t = 0$. Standard relative error calculations ($(B - A)/(A)$) are not well suited to high-contrast astrophysical environments; this is why the residuals were normalised by the global maximum of the original fine grid. The relative residual is strictly defined as $(B - A)/(\max(A))$.

The residuals in the heatmaps, Figure 4.2, illustrate that the greatest differences are found in the thin regions containing sharp contact discontinuities and highly structured shock fronts. This is an expected outcome, as during each step, the plotfile is remapped onto a domain that is coarser by a factor of two. When a sharp discontinuity is mapped onto a larger cell volume, the resulting interpolated value is the exact spatial average of the sub-grid structure. This yields local residual banding that is strictly limited to the shock boundaries.

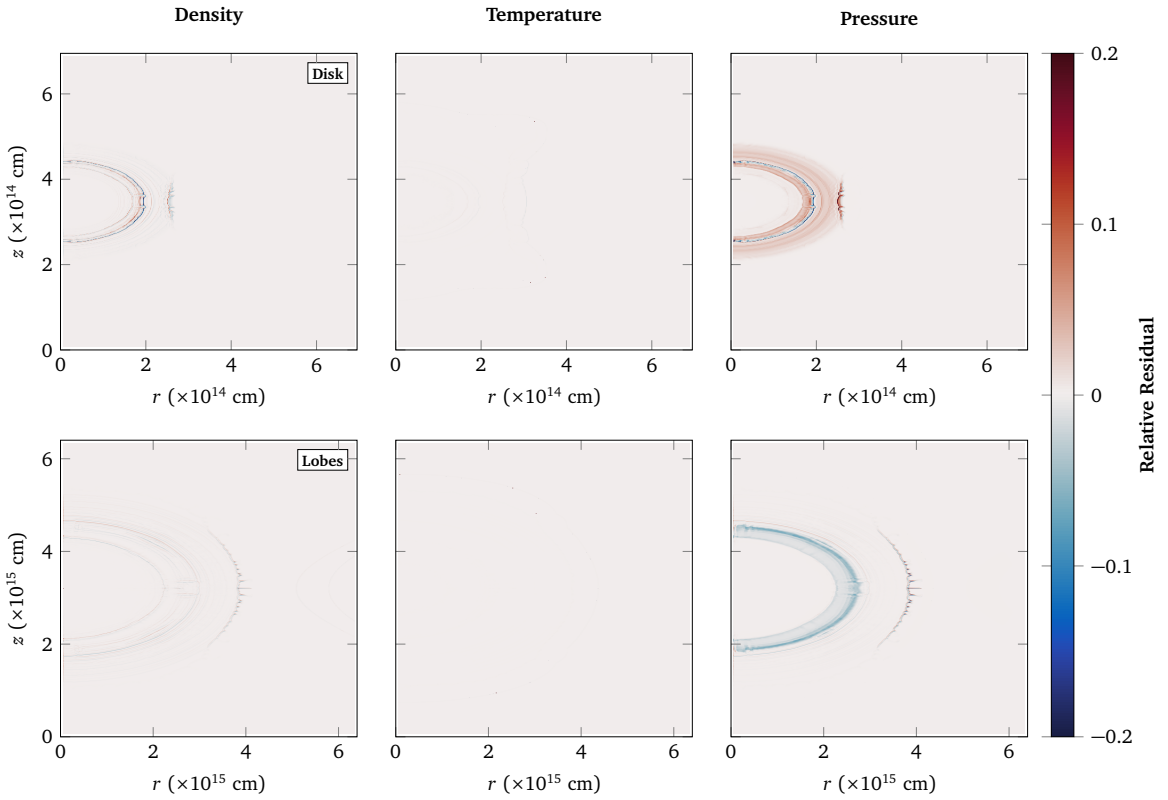

Figure 4.2: Relative residuals for density (left), temperature (centre), and pressure (right). Top row: equatorial disc transition (Part 2 to 3, domain 6.95×10^{14} cm). Bottom row: bipolar lobes transition (Part 5 to 6, domain 6.4×10^{15} cm). The symmetric colourbar spans $[-0.2, 0.2]$.

This grid-averaging effect is confirmed quantitatively in the 1D shock profile comparisons for the equatorial disc (Figure 4.3). The global structure and positioning

of the shocks in the coarse grid track the highly resolved data. The relative residual spikes, which peak at approximately 20% for density and slightly higher for pressure, occur exclusively at the geometric peaks and troughs of the shock structure.

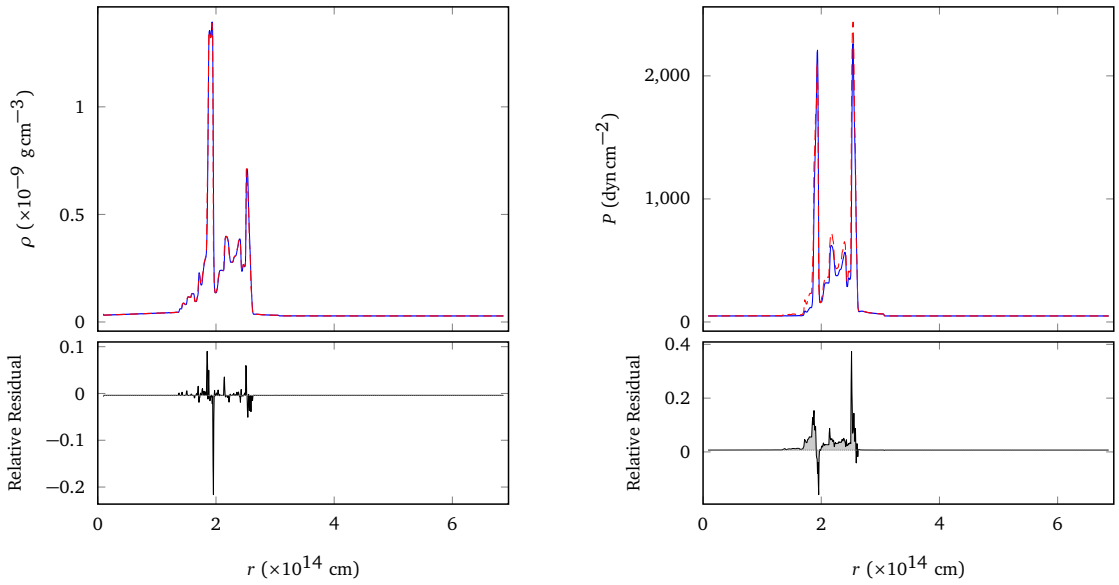

Figure 4.3: 1D shock profile comparisons and relative residuals for the equatorial disc model (Part 2 to 3 transition) for density (top) and pressure (bottom). The highly resolved original grid (Run A) is represented by the solid blue line, and the mapped coarse grid (Run B) by the red dashed line.

Moreover, the 1D profiles for the bipolar lobes model (Figure 4.4) demonstrate that this stability persists even under extreme physical stress. Despite the highly turbulent fluid dynamics and complex shock interactions present at this advanced evolutionary stage ($r \approx 10^{15}$ cm), interpolation errors remain highly localised, and the macroscopic shock amplitudes are perfectly preserved across the grid transition. These discrepancies do not compromise global conservation because they are purely local volume-averaging artefacts, rather than systemic numerical drifts. This ensures that the hydrodynamics solver can safely continue without triggering instabilities.

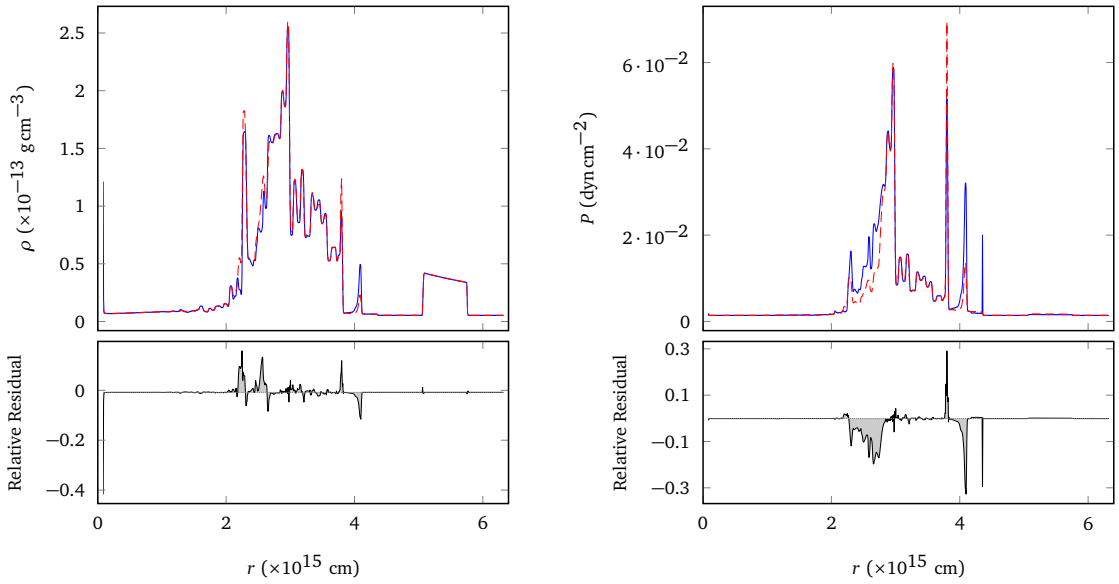

Figure 4.4: 1D shock profile comparisons and relative residuals for the bipolar lobes model (Part 5 to 6 transition) for density (top) and pressure (bottom). The original fine grid (Run A) is shown as a solid blue line, and the mapped coarse grid (Run B) is shown as a red dashed line.

4.2 Post-processing

Currently, there is no unified tool suite for analysing CASTRO plotfile data. The CASTRO developers suggest relying on third-party software such as `yt` or VisIt for visualisation, alongside separate conversion utilities included in the CASTRO distribution. However, this fragmented workflow often requires redundant data transformations, as the standard ASCII outputs generated by CASTRO do not conform to the specific grid structures demanded by RT codes. Furthermore, while the Python-based `yt` package is highly accessible, relying on third-party wrappers introduces significant computational overhead when processing massive multidimensional arrays.

To resolve these inefficiencies, a postprocessing package was developed natively in Julia (Bezanson et al., 2017). Julia was selected because it uniquely solves the "two-language problem", combining the high-level readability of a scripting language with the execution speed of compiled C code. This enabled the creation of a zero-overhead pipeline, the architecture of which is divided into three primary modules: a direct binary reader, an analytical visualisation engine, and a structural transformation layer that converts hydrodynamic data directly into either a generalised ASCII format or the specific grid structure required by the SIROCCO RT code.

4.2.1 Binary Reader

The core of the post-processing package is a custom binary reader designed to load CASTRO plotfile data directly into Julia arrays. The reading process works in two main steps. First, it parses the global ASCII `Header` and the metadata file `Cell_H` located in the `Level_0` directory to map the data structure.

Because the SN interactions in this thesis are simulated on a single uniform grid without using Adaptive Mesh Refinement, the reader is simplified to target only Level 0. This simplification actually speeds up the reading process, as it allows the code to pull strictly continuous memory blocks.

After the correct byte offsets are identified, the script seeks the exact byte location in the binary files. It then uses Julia's `reinterpret` function to instantly convert the raw byte stream into multidimensional Float64 arrays (Script A.7). Additionally, the reader checks the plotfile inventory dynamically. If a derived variable, such as velocity magnitude, is requested but was not saved by CASTRO, the reader automatically calculates it from the saved velocity components. In CASTRO, derived variables are secondary physical quantities, that are computed from the fundamental conserved state variables rather than being explicitly evolved by the core hydrodynamic solver.

4.2.2 Data Converter

The second module of the post-processing pipeline focuses on data conversion. Because different analysis tools and RT codes require specific input formats, this script is designed with two distinct conversion modes: a general ASCII export and a specialised export tailored specifically for the SIROCCO code.

For general analysis, the `export_to_dat` function transforms the loaded multidimensional CASTRO arrays into a standard, column-based text file. It flattens the data arrays and writes them alongside their exact spatial coordinates (r and z). This provides a simple, readable format for any external plotting or analysis software that cannot process native binary files directly.

Rather than relying on intermediate scripts to prepare the data for RT processing, the `export_to_sirocco` function bridges the reader and the RT code directly. Because RT codes typically require lower grid resolutions than hydrodynamics solvers, this function incorporates a built-in downsampling algorithm (Script A.8). To ensure physical conservation during this grid reduction, scalar fields (such as density and temperature) are averaged using a cylindrical volume-weighted method, while velocity vectors are averaged using a simple arithmetic mean.

Finally, the SIROCCO exporter applies a physical masking logic to the grid. It assigns an `inwind` flag to every cell, dictating which regions the RT code should process. The function automatically excludes boundary guard cells and the bottom symmetry

half of the grid. Additionally, it identifies and masks out deep SN ejecta based on a user-defined cutoff limit for the Helium-4 mass fraction. This ensures that SIROCCO dedicates its computational resources exclusively to the relevant circumstellar interacting regions.

4.2.3 Data Visualisation

The final component of the post-processing pipeline is a custom visualisation script. Because astrophysical simulations generate data spanning immense dynamic ranges, tailored plotting logic is necessary to interpret the results effectively. This module automates the generation of 2D heatmaps directly from the extracted CASTRO arrays.

A key feature of the visualiser is its automated management of units and labels. It utilises a predefined dictionary to map raw CASTRO variable names (e.g., `rho_e`) to publication-ready labels with the correct physical units (e.g., e (erg cm^{-3})). Additionally, the script dynamically scales the spatial axes. It can convert the native centimetre coordinates into astronomical units or parsecs, depending on the physical scale of the model, and it automatically formats the elapsed simulation time into days or years.

The visualisation logic was explicitly designed to address the unique temporal and geometric requirements of this study. Because the hydrodynamic initialisation represents an already evolved physical state, the script includes a temporal offset parameter (`start_day_offset`) to correctly recalculate and display the true physical time of the system.

Furthermore, the script accommodates the 2D axisymmetric cylindrical geometry (r, z) of the simulations with flexible spatial bounds. For greater clarity in specific analyses, it can crop the vertical axis at $z = 0$ (`crop_z_zero`) to focus purely on the upper hemisphere. Conversely, it can activate a geometric mirroring function (`mirror_r`, Script A.9) that reflects the radial data across the z-axis, reconstructing a full, symmetrical 2D cross-section of the entire interacting system.

Finally, the script rigorously handles mathematical edge cases during data normalisation. When applying logarithmic colour scales—which are essential for visualising the steep density gradients of the stellar winds—the script automatically filters out zero or negative values to prevent undefined mathematical errors during the plotting process.

Chapter 5

Hydrodynamic Evolution and Synthetic Observables

A RSG with a mass of $M_\star = 15\,M_\odot$ and a radius of $R_\star = 7.285 \times 10^{13}$ cm ($\approx 1,050\,R_\odot$) was selected as the SN progenitor. The 1D model utilised for the initial shock breakout is detailed in Holoubek (2024). The subsequent multidimensional interaction was simulated for two distinct CSM geometries: an equatorial disc and bipolar lobes. To accommodate the expanding spatial domain, a sequential reinitialisation procedure was implemented, wherein data from the preceding simulation phase was mapped as the input for the subsequent grid. This methodology allowed the physical interaction to be computed up to spatial scales of 1 pc.

5.1 Hydrodynamic Models

The hydrodynamic visualisations are presented in two distinct phases for each model. To accommodate the expanding domain, the later stages utilise adjusted scales with lower minima, as the initial ranges are no longer appropriate. Full simulation video sequences are accessible at `https://is.muni.cz/auth/th/k2gxj/Simulation_clips.zip`.

5.1.1 Equatorial Disc

The first part of the hydrodynamic evolution of the SN interacting with the equatorial disc is shown in Figure 5.1. During the early epochs (8 and 40 days post-explosion), asymmetry is already visible. The influence of the disc is seen in the velocity field, where the equatorial shock is decelerated compared to the expanding polar ejecta. Because the simulation is highly resolved, fluid instabilities are clearly captured. The Kelvin-Helmholtz instability is formed along the boundary between the dense disc and the polar wind. At the same time, Rayleigh-Taylor instabilities emerge as finger-like

structures at the borders of the ejecta. The most visible mixing is located directly at the interface between the decelerated ejecta and the disc.

The snapshots from days 170 and 598 illustrate a later phase of the interaction. A clear difference in temperature is observed between the interacting and non-interacting regions. The expanding polar ejecta cool down, while the equatorial zone remains hotter due to the continuous collision. The physical resistance of the disc generates a high-pressure region. This pressure redirects the kinetic energy of the ejecta toward the poles, which creates a distinct bipolar outflow.

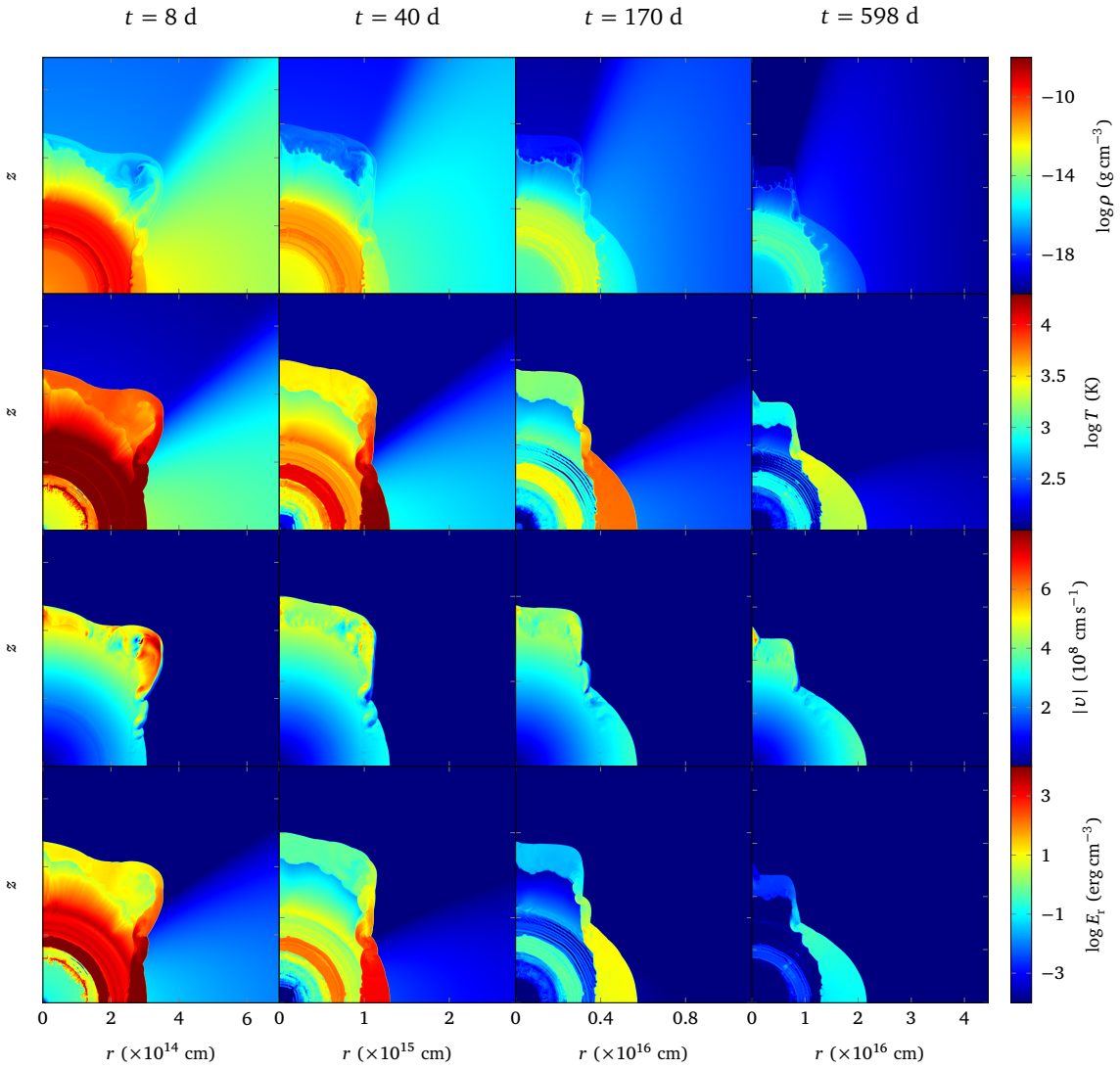

Figure 5.1: Evolution of the SN shock interacting with the equatorial disc. Columns show snapshots at 8, 40, 170, and 598 days post-explosion. Rows display (top to bottom) density (ρ), temperature (T), velocity magnitude ($\mid v \mid$), and radiative energy density (E_r). All panels maintain a 1:1 physical aspect ratio; the vertical spatial scale (z) matches the indicated radial scale (r) for each column.

Figure 5.2 illustrates the late-time remnant phase. As the expansion continues, the overall temperature of the ejecta decreases, and only the outer shock front remains distinctly hot. The mixing with the surrounding medium leads to a decrease in the ejecta density, leaving only the densest structures clearly visible. In the velocity field, the equatorial expansion is almost completely stalled by the remnants of the disc. In contrast, the velocity remains high at the poles, where the ejecta expands freely into space.

By the end of the simulation, the physical domain reaches a size exceeding 1 pc. The original equatorial disc is completely swept up by the SN shock. At this stage, the most prominent feature breaking the spherical symmetry is the bipolar outflow.

5.1.2 Bipolar Lobes

Similar to the Equatorial Disc model, the evolution of the bipolar lobes is divided into two phases. Figure 5.3 presents the early stages of the interaction. Because the structural parameters are based on the Homunculus nebula, the main collision occurs at later times compared to the Disc model. This initial phase captures the expansion of the SN inside the inner cavity, which represents the Little Homunculus. A main difference from the disc simulation is that the ejecta collide directly with the dense lobe walls and gradually fill the entire cavity. This behaviour is clearly visible in the temperature and velocity magnitude panels at $t = 2,184$ d. Furthermore, the interacting ejecta remain noticeably hotter overall when compared to the equatorial disc scenario.

The late-time phase of the interaction is shown in Figure 5.4. At this stage, the ejecta has completely swept up the inner lobe and continues to fill the outer cavity. A notable thermodynamic difference from the disc simulation is that the shocked material remains hotter overall, with a hot, thin shell persisting for over 100 years. Furthermore, the fast polar outflow does not survive the passage through the dense lobe structures. The final geometry of the remnant is heavily influenced by the surrounding lobes, resulting in a broad, peanut-shaped morphology.

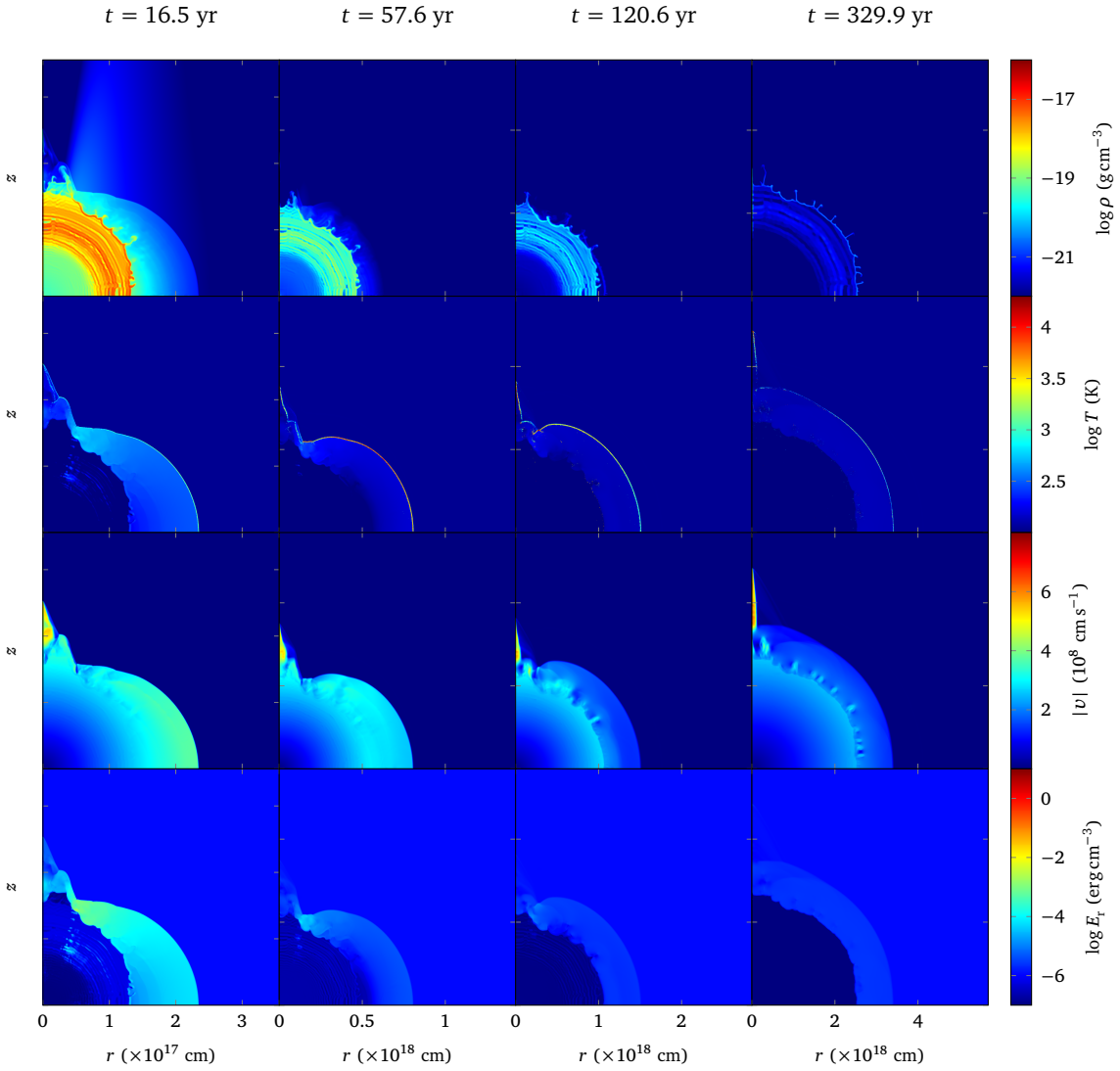

Figure 5.2: Evolution of the SN shock interacting with the equatorial disc. Columns show snapshots at 16.5, 57.6, 120.6, and 329.9 years post-explosion. Rows display (top to bottom) density (ρ), temperature (T), velocity magnitude ($\mid \upsilon \mid$), and radiative energy density (E_{r}). All panels maintain a 1:1 physical aspect ratio; the vertical spatial scale (z) matches the indicated radial scale (r) for each column.

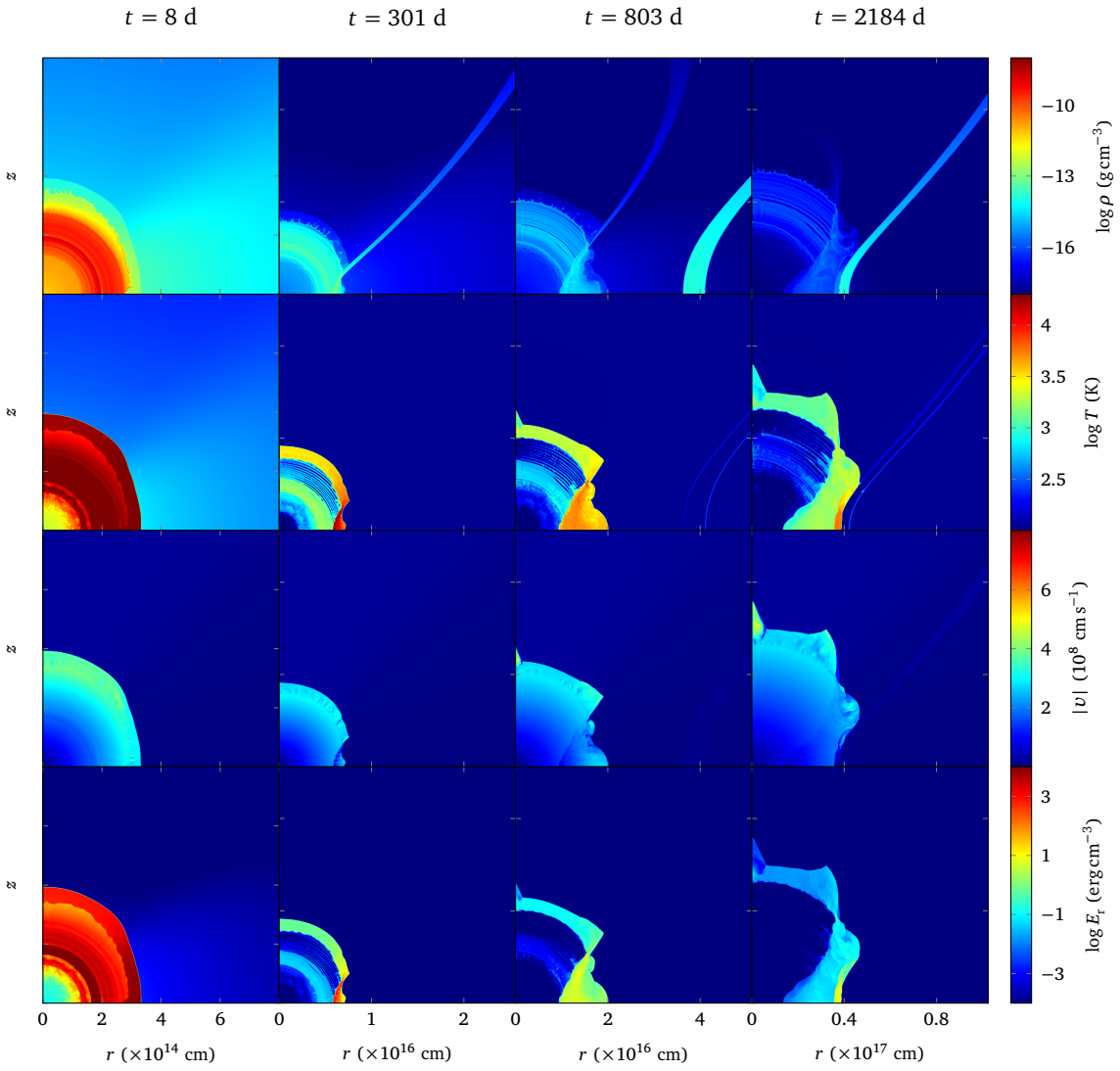

Figure 5.3: Evolution of the SN interacting with the bipolar lobes. Columns show snapshots at 8, 301, 803, and 2,184 days post-explosion. Rows display (top to bottom) gas density (ρ), temperature (T), velocity magnitude ($|v|$), and radiative energy density (E_r). All panels maintain a 1:1 physical aspect ratio; the vertical spatial scale (z) matches the indicated radial scale (r) for each column.

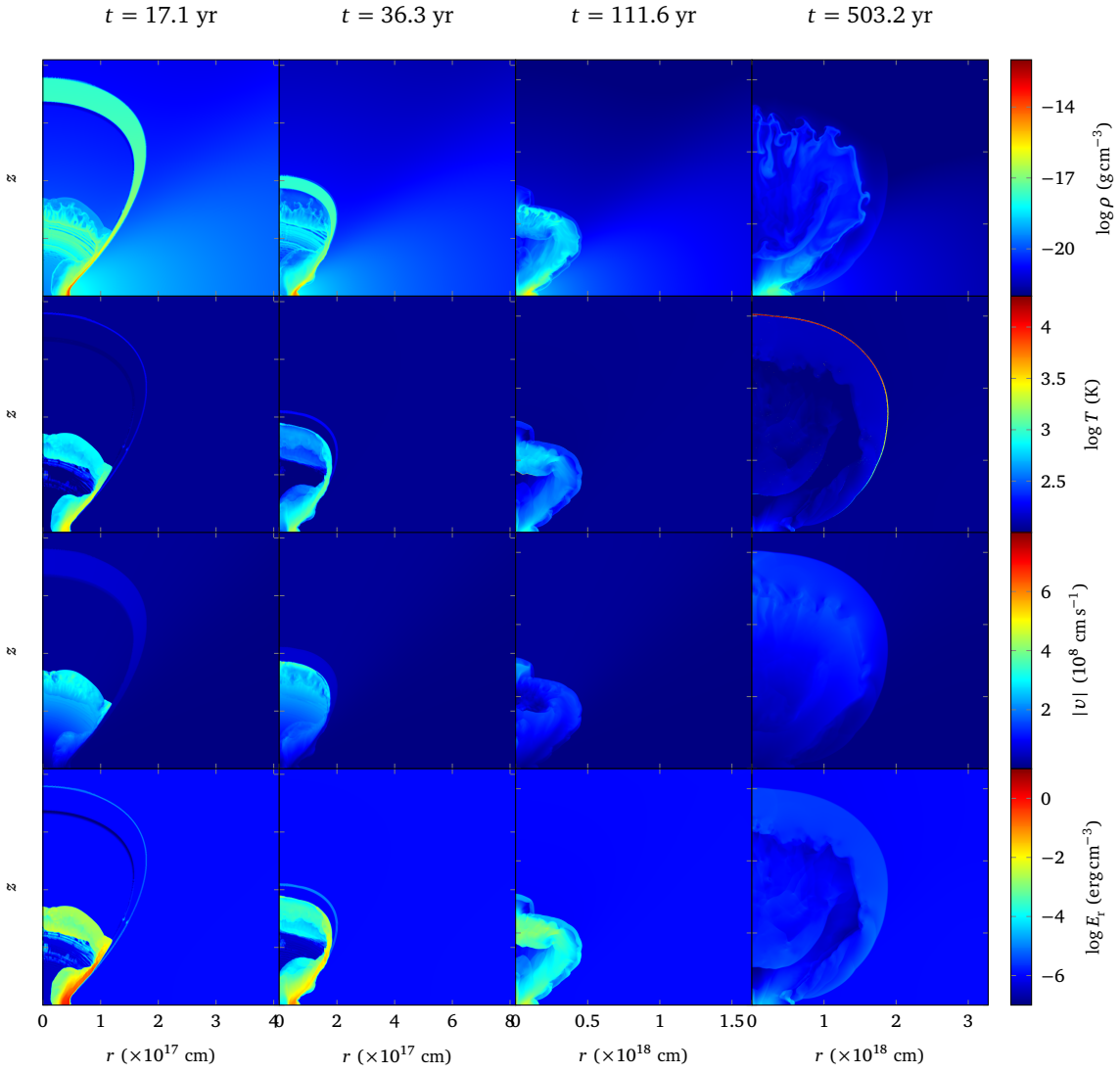

Figure 5.4: Late-time evolution of the SN interacting with the bipolar lobes. Columns show snapshots at 17.1, 36.3, 111.6, and 503.2 years post-explosion. Rows display (top to bottom) gas density (ρ), temperature (T), velocity magnitude ($|v|$), and radiative energy density (E_r). All panels maintain a 1:1 physical aspect ratio; the vertical spatial scale (z) matches the indicated radial scale (r) for each column.

5.2 Synthetic Observables

While hydrodynamic simulations detail the physical morphology and thermodynamic state of the SN remnant, they do not directly yield observable quantities. To determine how the distinct structural differences between the equatorial disc and the bipolar lobes translate into observations, the multidimensional CASTRO data are processed using RT. In this section, the SIROCCO code is used to generate synthetic light curves and spectra based on the hydrodynamic outputs. Even though the simulations extend into the late remnant phase, synthetic observables are only extracted for the early SN phase, because modelling late-time emission requires a different theoretical approach.

5.2.1 Light Curves

The synthetic B, V, and R band light curves for the equatorial disc and bipolar lobe interactions are presented in Figures 5.5 and 5.6, respectively. These observables were derived by processing the pseudo-bolometric spectra generated by SIROCCO across a wavelength range of 100–30, 000 Å. While the total integration yields the bolometric light curve (Figure B.1), convolution with standard transmission functions produces the specific broadband filter photometry. As previously noted regarding the bolometric limits, the initial peak luminosities are overestimated due to the instantaneous thermalisation of the shock breakout within the RT model. Furthermore, discrete vertical jumps are visible—most notably in the Lobes models—which correspond directly to the spatial grid reinitialisation procedure rather than physical collision events.

Despite these numerical artifacts, the defining morphological characteristic of the interaction phase is clearly reproduced: an extended, luminous plateau. The Disc model exhibits a highly continuous plateau, reflecting steady shock propagation into the equatorial torus. In contrast, the Lobes model displays a more structured evolution, particularly in the equatorial viewing angle, which corresponds to the sequential interactions with the nested CSM shells. Following this interaction phase, a distinct colour divergence emerges across all models; while the V and R bands exhibit a steady decline in absolute magnitude, the B band maintains a remarkably constant luminosity, indicating sustained late-time emission in the blue continuum.

5.2.2 Spectra

The spectral analysis focuses primarily on the Balmer series, which constitutes the most significant emission features in Type IIn SNe. Figure 5.7 presents a comparison of the synthetic optical spectra across the 4, 000–7, 500 Å range for both the disc and Lobes models. Because it takes longer for the SN ejecta to reach the more distant polar CSM, the spectra for the two models are taken at different post-explosion epochs

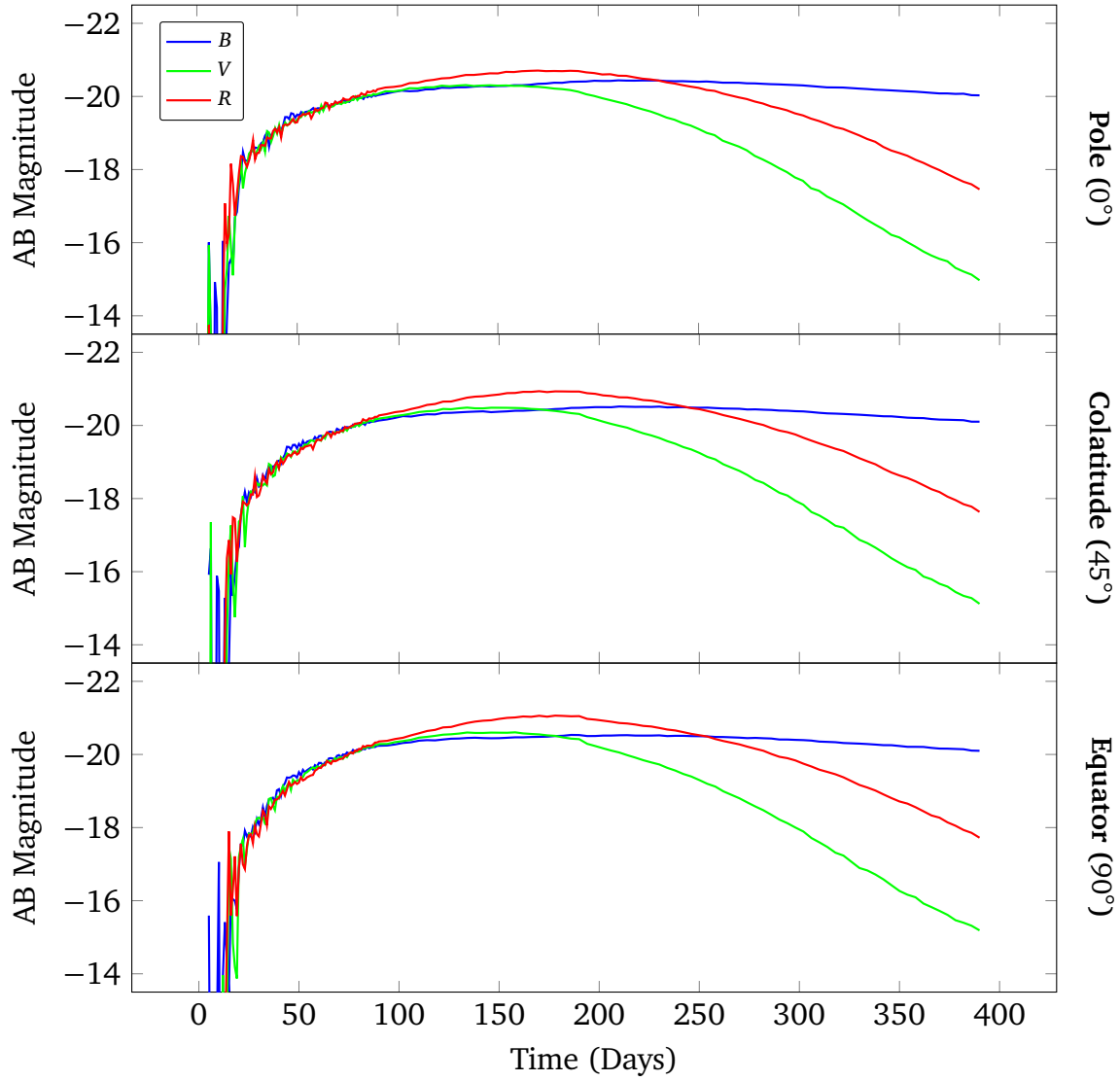

Figure 5.5: Synthetic B, V, and R band light curves for the Equatorial Disc interaction model in absolute AB magnitude. The panels display observer viewing angles at pole-on (0°, top), mid-latitudes (45°, middle), and edge-on (90°, bottom). The y-axis scale highlights the extended interaction plateau and the late-time colour divergence.

corresponding to their respective peak interactions. To facilitate a direct morphological comparison, the flux in each spectrum is peak-normalised to the Hα line. Both models successfully reproduce the prominent peaks typical of the hydrogen Balmer series: Hα, Hβ, Hγ, and Hδ. The observable variability in line profiles between the 0° , 45° and 90° viewing angles is a direct consequence of the highly asymmetric morphological structure of the interaction. In addition to the dominant hydrogen lines, a notable secondary emission feature is present near 5, 900 Å, which can be recognised to He I λ5876.

Figure 5.7 presents a detailed kinematic comparison of the evolving Hα line profile, segmented by viewing angle: pole-on (0°), mid-latitude (45°), and equatorial (90°).

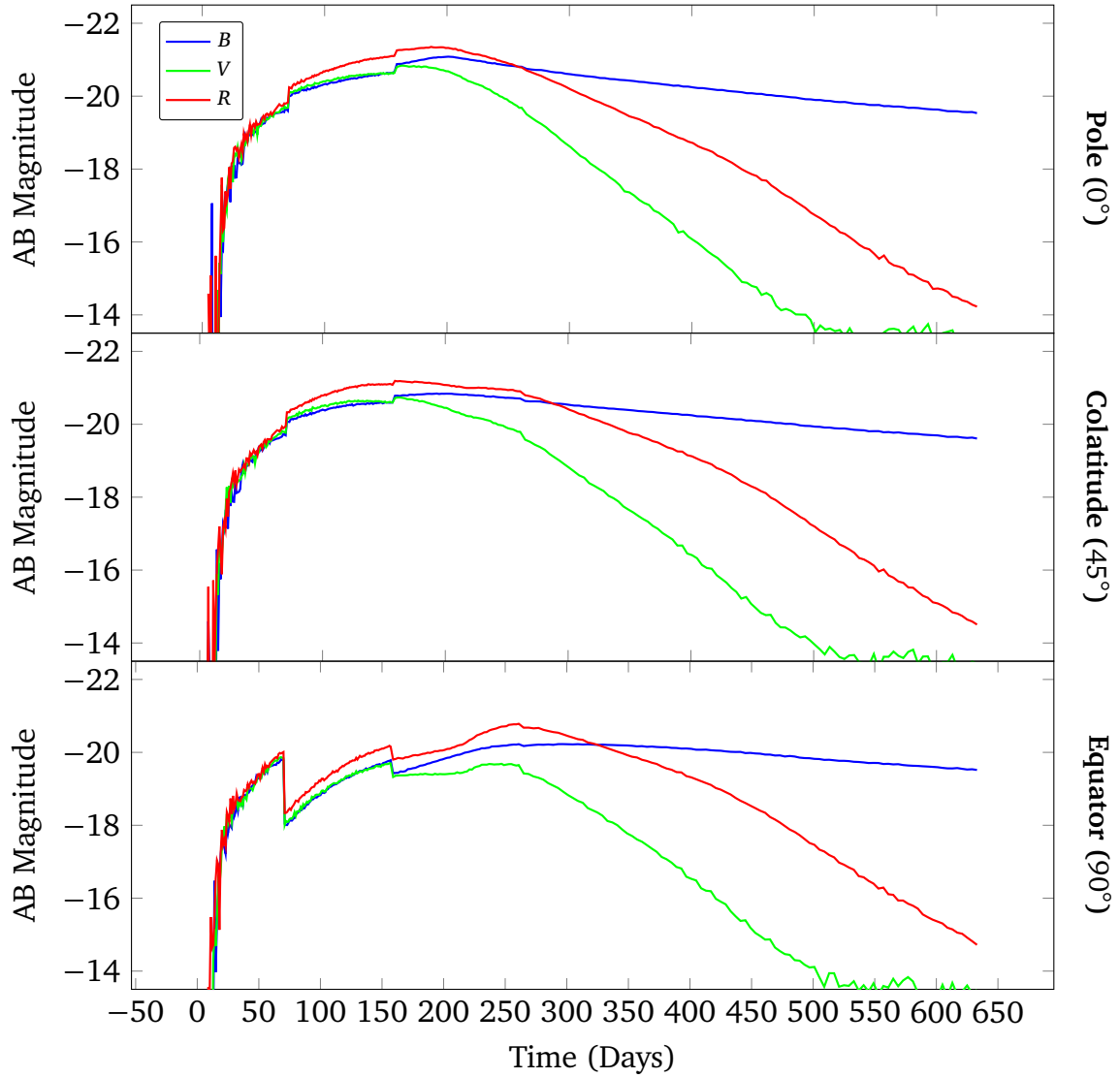

Figure 5.6: Synthetic B, V, and R band light curves for the Bipolar Lobes interaction model in absolute AB magnitude. The panels display viewing angles at pole-on (0°, top), mid-latitudes (45°, middle), and edge-on (90°, bottom). Discrete vertical jumps visible during the plateau phase are numerical artifacts from the spatial grid reinitialisation procedure.

Note that the Lobes model is shown at later physical epochs (up to Day 803) compared to the Disc model (up to Day 250), reflecting the time delay required for the ejecta to reach and interact with the more distant polar CSM structures. The most pronounced morphological differences occur between the polar and equatorial views. This contrast arises because the polar axis represents a path of relatively free expansion, whereas the equatorial plane contains dense CSM that decelerates the ejecta and drives strong interaction. In the Disc model, the equatorial view does not start as a simple peak; instead, it exhibits a complex, multi-peaked structure as early as Day 50. This morphology persists and broadens slightly over the 250-day evolution, maintaining deep emission and absorption variations across the core. Conversely, the pole-on view be-

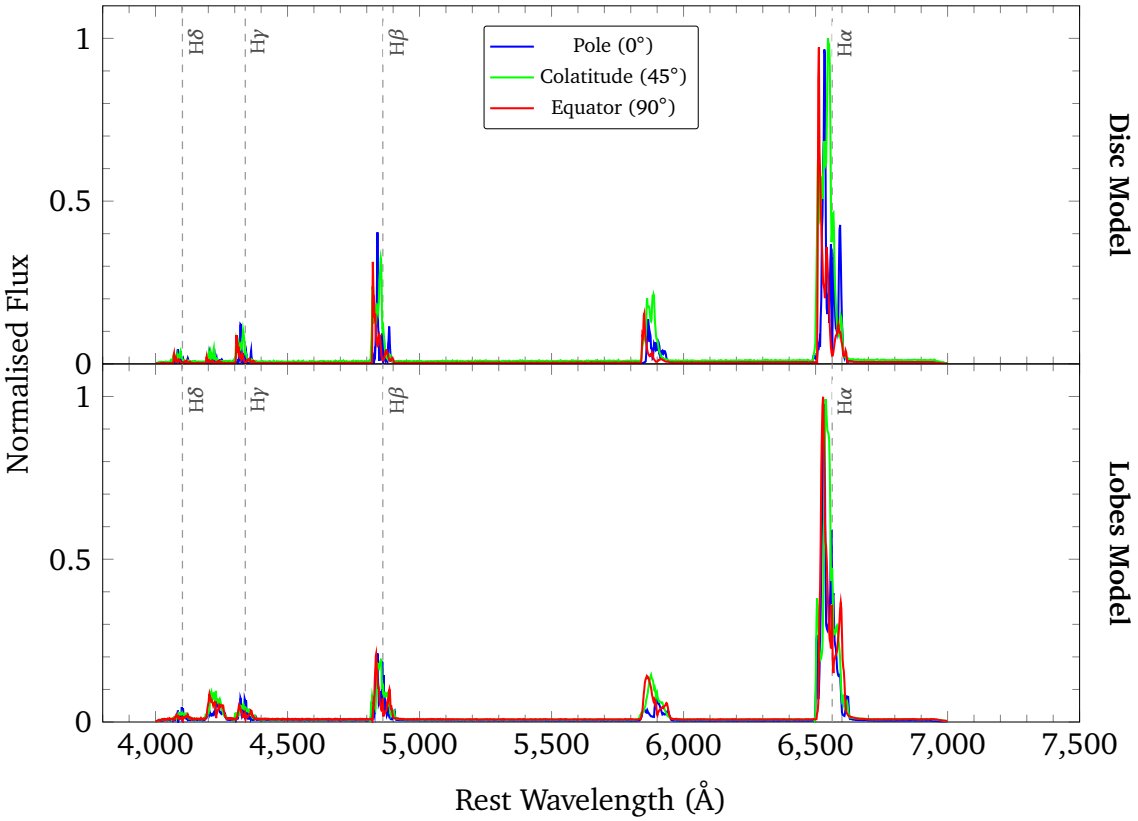

Figure 5.7: Synthetic optical spectra ($4,000 - 7,500$ Å) for the Disc (top) $t = 250$ d and Lobes (bottom) $t = 401$ d models at peak interaction. Flux is peak-normalised to the Hα line. Vertical dashed lines mark the rest wavelengths of the primary Balmer series. The overlay demonstrates how global line profiles and the Balmer decrement vary across the 0° , 45° and 90° viewing angles.

gins at Day 50 with an asymmetric core that evolves into a structured profile by Day 250, dominated by a strong blue-shifted peak.

The kinematic evolution of the Lobes model presents a distinctly different physical scenario. During the earliest epochs (Days 80 and 199), prior to the onset of the main lobe interaction, the line profiles remain relatively narrow and similar across all viewing angles. However, once the interaction begins, stark geometric differences emerge. By Day 803, the pole-on view has broadened considerably, developing extended high-velocity wings and a prominent central dip at the rest wavelength. In contrast, the equatorial view evolves into a much narrower line by Day 803, lacking the extreme velocity wings seen at the poles. A similar, narrow central emission component is also clearly noticeable in the 45° mid-latitude view, reflecting the reduction of the observed radial velocity when viewing the expanding bipolar lobes from the side.

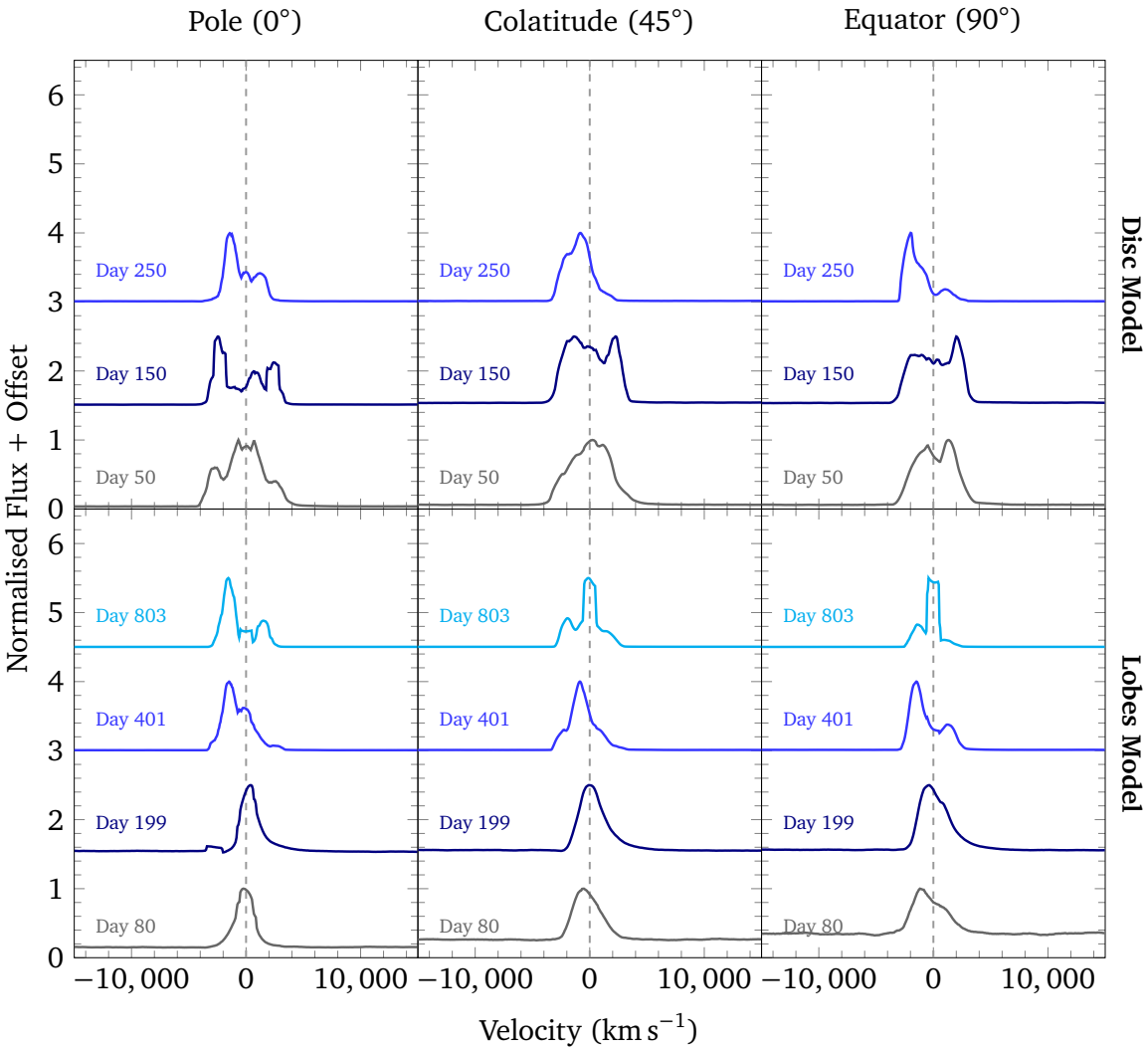

Figure 5.8: Time evolution of the Hα kinematic profile for the Disc (top) and Lobes (bottom) models across three viewing angles. Spectra are plotted in velocity space and vertically shifted by a constant offset for clarity.

Chapter 6

Discussion

The continuous characteristic of the 2D RHD simulations in CASTRO confirms that the reinitialisation procedure introduces no thermodynamic artifacts into the fluid dynamics. This physical robustness allows for a definitive analysis of how diverse CSM geometries dictate the long-term morphological and thermodynamic evolution of the SN remnant.

The simulations reveal a difference in energy dissipation scales between the two geometries. The equatorial disc forces an immediate deceleration of the ejecta during the earliest epochs, precisely when the initial shock kinetic energy is at its absolute maximum. Conversely, the bipolar lobes represent a delayed interaction scenario. Because the ejecta expands and cools significantly before colliding with the distant lobe walls at roughly 0.1 pc, the resulting shock interaction is thermodynamically sustained but dynamically less extreme. If observed, this specific delayed collision would appear as late-time bumps or sudden brightenings in the photometric light curves. This aligns with the observational frameworks established by Smith (2017), who demonstrated that such late-time rebrightenings are the characteristic signatures of pre-SN mass-loss eruptions.

As the interaction transitions into the late nebular phase, the structural consequences of the surrounding CSM become pronounced. The outer bipolar lobes act as a physical boundary that restricts free expansion, effectively functioning as a mass accumulation zone that traps the ejecta. This structural bottleneck results in a remnant that is significantly denser, hotter, and more uniform, maintaining a relatively homogeneous velocity distribution. In contrast, the equatorial disc actively disrupts the compactness of the remnant, exhibiting hydrodynamic behaviour consistent with the models of Vlasis et al. (2016). While the disc completely stalls radial expansion in the equatorial plane, the unhindered polar axes create a path of least resistance. This drives a high-velocity bipolar outflow, allowing the SN to vent its internal energy freely into the interstellar medium.

Due to the discrete processing pipeline, translating the density structures from the

RHD simulations into synthetic observables presents methodological challenges. For this reason, the RT outputs from SIROCCO are used primarily as an exploratory tool. Rather than aiming for exact quantitative matches with real-world photometry, the focus is on identifying qualitative trends in these synthetic spectra and light curves. Despite these constraints, the observables successfully capture how different CSM geometries shape SN emission.

This approach is particularly valuable in the Bipolar Lobes model, especially during the delayed CSM interaction. The evolution of the Hα line profile is a strong indicator of the underlying geometry. When observed from the equator, the Hα line shifts from a broad, interaction-driven profile on Day 401 to a noticeably narrower feature on Day 803. This narrowing occurs because the ejecta is forced into the restricted physical space between the dense lobes. This proves that the viewing angle strongly dictates the observed line width in asymmetric environments. Finally, the synthetic spectra reproduce the core features of Type IIn SNe established by theoretical benchmarks (e.g., Dessart et al. (2015)): the emission is dominated by the hydrogen Balmer series and the Hα core clearly exhibits the anticipated blue shift resulting from the advancing shock front.

The primary limitation in generating synthetic observables stems from the massive spatial scaling required between the hydrodynamics and the RT codes. Throughout the CASTRO simulations, the physical domain expands by four orders of magnitude, growing from an inner boundary of approximately 10^{14} cm out to 10^{18} cm. Mapping this entire evolution onto a single grid would require either a logarithmic spatial scale or an impossibly fine uniform mesh. Because MCRT codes like SIROCCO and SEDONA (Kasen et al., 2006) strictly require uniform grids, a continuous, one-to-one mapping across all epochs was computationally unfeasible. As a result, the pipeline was forced to handle each remapped phase of the hydrodynamic expansion as an independent, discrete simulation. This fragmented approach disrupts the continuous calculation of RT and is the direct cause of the artificial extremes seen in the early light curves. Treating these phases discretely triggers unphysical, instantaneous energy releases, which explains why the pseudo-bolometric peaks cross the superluminous threshold and why the U and I band filters exhibit maxima exceeding ($M_{\rm bol} < -22$ mag) (Figures B.2 and B.3). This discrete processing also causes the sudden brightness jumps during the plateau phase—most notably in the Bipolar Lobes models around Day 70 at the equator, which corresponds exactly to the introduction of the first lobe structures into the grid. An additional comparison of the light curves with those in Kurfürst et al. (2026) further highlights these spectral discrepancies. The comparison shows that the B band is excessively bright, especially in the later stages, and that the I band is too bright at the beginning. It also supports the observation that the light curve in the U filter is systematically too high. These incorrectly composed band light curves are likely the result of the specific parameter setup utilised in SIROCCO and will need to

be re-evaluated and optimised for future work. SIROCCO was utilised for this study to extract morphological trends, despite SEDONA being the established primary code in the standard pipeline.

Given these limitations, part of the future work should focus on processing the hydrodynamic outputs using SEDONA. Because the development of the multidimensional reinitialisation routine required the bulk of the project timeline, this step was deferred. However, a direct cross-code comparison between SEDONA and SIROCCO remains a necessary next step to verify the pipeline and fully understand the systematic errors introduced by the discrete processing.

Conclusions

This thesis investigated the long-term evolution of supernovae interacting with diverse circumstellar media (CSM) using 2D radiation hydrodynamics (RHD) simulations. Two distinct CSM geometries were selected, reflecting different pre-supernova mass-loss histories: an equatorial disc originating from binary interaction, and bipolar lobes resulting from episodic, pre-supernova eruptions. Simulating this evolution presented significant computational challenges. While the CASTRO code includes native domain expansion tools, they do not support radiation transport. To overcome this limitation, a custom sequential reinitialisation routine was developed. By applying a three-zone geometric blending technique, this routine successfully maintained thermodynamic stability while continuously expanding the physical domain up to scales of 1 pc. To streamline the subsequent data analysis, a custom post-processing package was developed natively in Julia. This tool bridges the gap between hydrodynamics and radiative transfer by directly reading CASTRO binary files, automating grid downsampling for the SIROCCO code, and generating 2D visualisations with zero computational overhead.

The long-term RHD simulations revealed dynamic and thermodynamic differences dictated by the underlying CSM geometry. The equatorial disc forces an immediate deceleration of the ejecta in the equatorial plane, creating a path of least resistance at the poles. This drives a high-velocity bipolar outflow that persists for over 200 years. Conversely, the bipolar lobes—modelled with parameters corresponding to the Homunculus Nebula in η Carinae—represent a delayed interaction scenario due to their much greater spatial scales. These vast lobes act as a mass accumulation zone, effectively confining the expanding ejecta. This structural bottleneck results in a remnant that is significantly hotter, denser, and more uniform than its disc counterpart.

Processing RHD structures into synthetic observables via SIROCCO successfully bridged the theoretical fluid dynamics with observational astronomy. Although computational constraints limited the radiative transfer outputs to general spectral shapes rather than exact numerical values, the synthetic spectra successfully reproduced the core defining characteristics of Type IIn supernovae. Specifically, the spectra exhibited the dominant hydrogen Balmer series and the anticipated blue-shifted Hα core. The bipolar lobe model proved particularly insightful during the delayed interaction

phase. The synthetic profiles demonstrated that the viewing angle strongly dictates the observed line width in asymmetric environments; the Hα kinematic profile became noticeably narrower when observed from the equator due to the ejecta being forced into the restricted physical space between the dense lobes.

The primary methodological constraints of this study emerged during the radiative transfer processing. Monte Carlo Radiative Transfer (MCRT) codes like SIROCCO and SEDONA strictly require uniform grids, rendering them incompatible with the massive, multi-scale spatial expansion of the RHD domain. Treating the expanding phases as discrete, independent inputs for SIROCCO disrupted the continuous calculation of radiation transport, introducing artificial extremes in the early observables.

Consequently, future work must focus on mitigating these discrete processing errors to extract precise, quantitative light curves for comparison with real-world photometry. A necessary next step is a direct cross-code comparison between SIROCCO and SEDONA to benchmark how different MCRT codes respond to these fragmented spatial inputs. Furthermore, alternative theoretical approaches will need to be explored to generate synthetic observables for the late remnant phase, as the physical conditions eventually fall outside the temperature and density regimes that standard MCRT codes can accurately process.

This work successfully achieved its primary objective: simulating the complex interaction between a supernova and its asymmetric CSM to study the long-term effects on the remnant morphology. With the custom, continuously expanding RHD simulation pipeline now fully operational, this computational framework is ready to be deployed to study a much wider variety of structures beyond equatorial discs and bipolar lobes.

Bibliography

A. Almgren, M. B. Sazo, J. Bell, A. Harpole, M. Katz, J. Sexton, D. Willcox, W. Zhang, & M. Zingale. Castro: A massively parallel compressible astrophysics simulation code. *Journal of Open Source Software*, 5(54):2513, 2020. doi: 10.21105/joss.02513.

A. S. Almgren, V. E. Beckner, J. B. Bell, M. S. Day, L. H. Howell, C. C. Joggerst, M. J. Lijewski, A. Nonaka, M. Singer, & M. Zingale. CASTRO: A New Compressible Astrophysical Solver. I. Hydrodynamics and Self-gravity. *The Astrophysical Journal*, 715 (2):1221–1238, June 2010. doi: 10.1088/0004-637X/715/2/1221.

W. D. Arnett. Type I supernovae. I - Analytic solutions for the early part of the light curve. *The Astrophysical Journal*, 253:785–797, Feb. 1982. doi: 10.1086/159681.

J. Bezanson, A. Edelman, S. Karpinski, & V. B. Shah. Julia: A fresh approach to numerical computing. *SIAM Review*, 59(1):65–98, 2017. doi: 10.1137/141000671.

M. R. Blanton & S. Roweis. K-Corrections and Filter Transformations in the Ultraviolet, Optical, and Near-Infrared. *The Astronomical Journal*, 133(2):734–754, Feb. 2007. doi: 10.1086/510127.

J. M. Blondin, P. Lundqvist, & R. A. Chevalier. Axisymmetric Circumstellar Interaction in Supernovae. *The Astrophysical Journal*, 472:257, Nov. 1996. doi: 10.1086/178060.

J. M. Blondin, A. Mezzacappa, & C. DeMarino. Stability of Standing Accretion Shocks, with an Eye toward Core-Collapse Supernovae. *Astrophysical Journal*, 584(2):971–980, Feb. 2003. doi: 10.1086/345812.

R. J. Bruch, A. Gal-Yam, S. Schulze, O. Yaron, Y. Yang, M. Soumagnac, M. Rigault, N. L. Strotjohann, E. Ofek, J. Sollerman, F. J. Masci, C. Barbarino, A. Y. Q. Ho, C. Fremling, D. Perley, J. Nordin, S. B. Cenko, S. Adams, I. Adreoni, E. C. Bellm, N. Blagorodnova, M. Bulla, K. Burdge, K. De, S. Dhawan, A. J. Drake, D. A. Duev, A. Dugas, M. Graham, M. L. Graham, I. Irani, J. Jencson, E. Karamehmetoglu, M. Kasliwal, Y.-L. Kim, S. Kulkarni, T. Kupfer, J. Liang, A. Mahabal, A. A. Miller, T. A. Prince, R. Riddle, Y. Sharma, R. Smith, F. Taddia, K. Taggart, R. Walters, & L. Yan. A Large Fraction of Hydrogen-rich Supernova Progenitors Experience Elevated Mass Loss

Shortly Prior to Explosion. *The Astrophysical Journal*, 912(1):46, May 2021. doi: 10.3847/1538-4357/abef05.

G. L. Bryan, M. L. Norman, B. W. O'Shea, T. Abel, J. H. Wise, M. J. Turk, D. R. Reynolds, D. C. Collins, P. Wang, S. W. Skillman, B. Smith, R. P. Harkness, J. Bordner, J.-h. Kim, M. Kuhlen, H. Xu, N. Goldbaum, C. Hummels, A. G. Kritsuk, E. Tasker, S. Skory, C. M. Simpson, O. Hahn, J. S. Oishi, G. C. So, F. Zhao, R. Cen, Y. Li, & Enzo Collaboration. ENZO: An Adaptive Mesh Refinement Code for Astrophysics. *The Astrophysical Journal Supplement Series*, 211(2):19, Apr. 2014. doi: 10.1088/0067-0049/211/2/19.

R. A. Chevalier. Self-similar solutions for the interaction of stellar ejecta with an external medium. *The Astrophysical Journal*, 258:790–797, July 1982. doi: 10.1086/160126.

R. A. Chevalier & C. Fransson. Emission from Circumstellar Interaction in Normal Type II Supernovae. *The Astrophysical Journal*, 420:268, Jan. 1994. doi: 10.1086/173557.

R. A. Chevalier & C. M. Irwin. Shock Breakout in Dense Mass Loss: Luminous Supernovae. *The Astrophysical Journal Letters*, 729(1):L6, Mar. 2011. doi: 10.1088/2041-8205/729/1/L6.

N. N. Chugai. Broad emission lines from the opaque electron-scattering environment of SN 1998S. *Monthly Notices of the Royal Astronomical Society*, 326(4):1448–1454, Oct. 2001. doi: 10.1111/j.1365-2966.2001.04717.x.

J. S. W. Claeys, S. E. de Mink, O. R. Pols, J. J. Eldridge, & M. Baes. Binary progenitor models of type IIb supernovae. *Astronomy & Astrophysics*, 528:A131, Apr. 2011. doi: 10.1051/0004-6361/201015410.

P. A. Crowther. Physical Properties of Wolf-Rayet Stars. *Annual Review of Astronomy and Astrophysics*, 45(1):177–219, Sept. 2007. doi: 10.1146/annurev.astro.45.051806.110615.

S. E. de Mink, H. Sana, N. Langer, R. G. Izzard, & F. R. N. Schneider. The Incidence of Stellar Mergers and Mass Gainers among Massive Stars. *The Astrophysical Journal*, 782(1):7, Feb. 2014. doi: 10.1088/0004-637X/782/1/7.

L. Dessart & D. J. Hillier. Non-LTE time-dependent spectroscopic modelling of Type II-plateau supernovae from the photospheric to the nebular phase: case study for 15 and 25 $M_{\odot}$ progenitor stars. *Monthly Notices of the Royal Astronomical Society*, 410(3):1739–1760, Jan. 2011. doi: 10.1111/j.1365-2966.2010.17557.x.

L. Dessart, E. Audit, & D. J. Hillier. Numerical simulations of superluminous supernovae of type IIn. *Monthly Notices of the Royal Astronomical Society*, 449(4):4304–4325, June 2015. doi: 10.1093/mnras/stv609.

V. V. Dwarkadas & S. P. Owocki. Radiatively Driven Winds and the Shaping of Bipolar Luminous Blue Variable Nebulae. *The Astrophysical Journal*, 581(2):1337–1343, Dec. 2002. doi: 10.1086/344257.

A. V. Filippenko. Optical Spectra of Supernovae. *Annual Review of Astronomy and Astrophysics*, 35:309–355, Jan. 1997. doi: 10.1146/annurev.astro.35.1.309.

T. Foglizzo, P. Galletti, L. Scheck, & H.-T. Janka. Instability of a Stalled Accretion Shock: Evidence for the Advective-Acoustic Cycle. *Astrophysical Journal*, 654(2): 1006–1021, Jan. 2007. doi: 10.1086/509612.

R. J. Foley, N. Smith, M. Ganeshalingam, W. Li, R. Chornock, & A. V. Filippenko. SN 2006jc: A Wolf-Rayet Star Exploding in a Dense He-rich Circumstellar Medium. *The Astrophysical Journal Letters*, 657(2):L105–L108, Mar. 2007. doi: 10.1086/513145.

C. Fransson, P. Lundqvist, & R. A. Chevalier. Circumstellar Interaction in SN 1993J. *The Astrophysical Journal*, 461:993, Apr. 1996. doi: 10.1086/177119.

C. Fransson, M. Ergon, P. J. Challis, R. A. Chevalier, K. France, R. P. Kirshner, G. H. Marion, D. Milisavljevic, N. Smith, F. Bufano, A. S. Friedman, T. Kangas, J. Larsson, S. Mattila, S. Benetti, R. Chornock, I. Czekala, A. Soderberg, & J. Sollerman. High-density Circumstellar Interaction in the Luminous Type IIn SN 2010jl: The First 1100 Days. *The Astrophysical Journal*, 797(2):118, Dec. 2014. doi: 10.1088/0004-637X/797/2/118.

B. Fryxell, K. Olson, P. Ricker, F. X. Timmes, M. Zingale, D. Q. Lamb, P. MacNeice, R. Rosner, J. W. Truran, & H. Tufo. FLASH: An Adaptive Mesh Hydrodynamics Code for Modeling Astrophysical Thermonuclear Flashes. *The Astrophysical Journal Supplement Series*, 131(1):273–334, Nov. 2000. doi: 10.1086/317361.

A. Gal-Yam. Luminous Supernovae. *Science*, 337(6097):927, Aug. 2012. doi: 10.1126/science.1203601.

M. L. Graham, D. J. Sand, S. Valenti, D. A. Howell, J. Parrent, M. Halford, D. Zaritsky, F. Bianco, A. Rest, & B. Dilday. Clues to the Nature of SN 2009ip from Photometric and Spectroscopic Evolution to Late Times. *The Astrophysical Journal*, 787(2):163, June 2014. doi: 10.1088/0004-637X/787/2/163.

E. K. Grassberg, V. S. Imshennik, & D. K. Nadyozhin. On the Theory of the Light Curves of Supernovae. *Astrophysics and Space Science*, 10(1):28–51, Jan. 1971. doi: 10.1007/BF00654604.

J. Guillochon, J. Parrent, L. Z. Kelley, & R. Margutti. An Open Catalog for Supernova Data. *The Astrophysical Journal*, 835(1):64, Jan. 2017. doi: 10.3847/1538-4357/835/1/64.

R. W. Hockney & J. W. Eastwood. *Computer Simulation Using Particles*. Taylor & Francis, Boca Raton, 1988.

F. Holoubek. Superzářivé supernovy, 2024. URL https://is.muni.cz/th/tgq0i/.

F. Hoyle & W. A. Fowler. Nucleosynthesis in Supernovae. *Astrophysical Journal*, 132: 565, Nov. 1960. doi: 10.1086/146963.

C. Huang & R. A. Chevalier. Electron scattering wings on lines in interacting supernovae. *Monthly Notices of the Royal Astronomical Society*, 475(1):1261–1273, Mar. 2018. doi: 10.1093/mnras/stx3163.

N. Ivanova, S. Justham, X. Chen, O. De Marco, C. L. Fryer, E. Gaburov, H. Ge, E. Glebbeek, Z. Han, X.-D. Li, G. Lu, T. Marsh, P. Podsiadlowski, A. Potter, N. Soker, R. Taam, T. M. Tauris, E. P. J. van den Heuvel, & R. F. Webbink. Common envelope evolution: where we stand and how we can move forward. *Astronomy and Astrophysics Reviews*, 21:59, Feb. 2013. doi: 10.1007/s00159-013-0059-2.

H.-T. Janka. Explosion Mechanisms of Core-Collapse Supernovae. *Annual Review of Nuclear and Particle Science*, 62(1):407–451, Nov. 2012. doi: 10.1146/annurev-nucl-102711-094901.

D. Kasen & S. E. Woosley. Type II Supernovae: Model Light Curves and Standard Candle Relationships. *The Astrophysical Journal*, 703(2):2205–2216, Oct. 2009. doi: 10.1088/0004-637X/703/2/2205.

D. Kasen, R. C. Thomas, & P. Nugent. Time-dependent Monte Carlo Radiative Transfer Calculations for Three-dimensional Supernova Spectra, Light Curves, and Polarization. *The Astrophysical Journal*, 651(1):366–380, Nov. 2006. doi: 10.1086/506190.

M. Kiewe, A. Gal-Yam, I. Arcavi, D. C. Leonard, J. Emilio Enriquez, S. B. Cenko, D. B. Fox, D.-S. Moon, D. J. Sand, A. M. Soderberg, & T. CCCP. Caltech Core-Collapse Project (CCCP) Observations of Type IIn Supernovae: Typical Properties and Implications for Their Progenitor Stars. *The Astrophysical Journal*, 744(1):10, Jan. 2012. doi: 10.1088/0004-637X/744/1/10.

P. Kurfürst & J. Krtička. Modeling of interactions between supernovae ejecta and aspherical circumstellar environments. *Astronomy & Astrophysics*, 625:A24, May 2019. doi: 10.1051/0004-6361/201833429.

P. Kurfürst, O. Pejcha, & J. Krtička. Supernova explosions interacting with aspherical circumstellar material: implications for light curves, spectral line profiles, and polarization. *Astronomy & Astrophysics*, 642:A214, Oct. 2020. doi: 10.1051/0004-6361/202039073.

P. Kurfürst, G. Bless, J. Fišák, F. Holoubek, J. Krtička, B. Kubátová, J. Kubát, & M. Zajaček. Supernova interactions with aspherical circumstellar material I: calculations of light curves, AB magnitudes, spectra, and polarisation. *arXiv e-prints*, art. arXiv:2601.15428, Jan. 2026. doi: 10.48550/arXiv.2601.15428.

K. S. Long & C. Knigge. Modeling the Spectral Signatures of Accretion Disk Winds: A New Monte Carlo Approach. *The Astrophysical Journal*, 579(2):725–740, Nov. 2002. doi: 10.1086/342879.

L. B. Lucy. Monte Carlo transition probabilities. *Astronomy & Astrophysics*, 384:725–735, Mar. 2002. doi: 10.1051/0004-6361:20011756.

L. B. Lucy. Monte Carlo transition probabilities. II. *Astronomy & Astrophysics*, 403: 261–275, May 2003. doi: 10.1051/0004-6361:20030357.

M. MacLeod, A. Antoni, A. Murguia-Berthier, P. Macias, & E. Ramirez-Ruiz. Common Envelope Wind Tunnel: Coefficients of Drag and Accretion in a Simplified Context for Studying Flows around Objects Embedded within Stellar Envelopes. *The Astrophysical Journal*, 838(1):56, Mar. 2017. doi: 10.3847/1538-4357/aa6117.

R. Margutti, D. Milisavljevic, A. M. Soderberg, R. Chornock, B. A. Zauderer, K. Murase, C. Guidorzi, N. E. Sanders, P. Kuin, C. Fransson, E. M. Levesque, P. Chandra, E. Berger, F. B. Bianco, P. J. Brown, P. Challis, E. Chatzopoulos, C. C. Cheung, C. Choi, L. Chomiuk, N. Chugai, C. Contreras, M. R. Drout, R. Fesen, R. J. Foley, W. Fong, A. S. Friedman, C. Gall, N. Gehrels, J. Hjorth, E. Hsiao, R. Kirshner, M. Im, G. Leloudas, R. Lunnan, G. H. Marion, J. Martin, N. Morrell, K. F. Neugent, N. Omodei, M. M. Phillips, A. Rest, J. M. Silverman, J. Strader, M. D. Stritzinger, T. Szalai, N. B. Utterback, J. Vinko, J. C. Wheeler, D. Arnett, S. Campana, R. Chevalier, A. Ginsburg, A. Kamble, P. W. A. Roming, T. Pritchard, & G. Stringfellow. A Panchromatic View of the Restless SN 2009ip Reveals the Explosive Ejection of a Massive Star Envelope. *The Astrophysical Journal*, 780(1):21, Jan. 2014. doi: 10.1088/0004-637X/780/1/21.

J. H. Matthews, K. S. Long, C. Knigge, S. A. Sim, E. J. Parkinson, N. Higginbottom, S. W. Mangham, N. Scepi, A. Wallis, H. A. Hewitt, & A. Mosallanezhad. SIROCCO: a publicly available Monte Carlo ionization and radiative transfer code for astrophysical outflows. *Monthly Notices of the Royal Astronomical Society*, 536(1):879–904, Jan. 2025. doi: 10.1093/mnras/stae2677.

D. Mihalas & R. I. Klein. On the solution of the time-dependent inertial-frame equation of radiative transfer in moving media to O(v/c). *Journal of Computational Physics*, 46:97–137, Apr. 1982. doi: 10.1016/0021-9991(82)90007-9.

D. Mihalas & B. W. Mihalas. *Foundations of radiation hydrodynamics*. Dover Publications, 1999.

R. Minkowski. Spectra of Supernovae. *Publications of the Astronomical Society of the Pacific*, 53(314):224, Aug. 1941. doi: 10.1086/125315.

T. J. Moriya & K. Maeda. Constraining Physical Properties of Type IIn Supernovae through Rise Times and Peak Luminosities. *The Astrophysical Journal Letters*, 790 (2):L16, Aug. 2014. doi: 10.1088/2041-8205/790/2/L16.

V. Morozova, A. L. Piro, M. Renzo, C. D. Ott, D. Clausen, S. M. Couch, J. Ellis, & L. F. Roberts. Light Curves of Core-collapse Supernovae with Substantial Mass Loss Using the New Open-source SuperNova Explosion Code (SNEC). *The Astrophysical Journal*, 814(1):63, Nov. 2015. doi: 10.1088/0004-637X/814/1/63.

D. K. Nadyozhin. The Properties of NI CO Fe Decay. *The Astrophysical Journal Supplement Series*, 92:527, June 1994. doi: 10.1086/192008.

E. O. Ofek, P. B. Cameron, M. M. Kasliwal, A. Gal-Yam, A. Rau, S. R. Kulkarni, D. A. Frail, P. Chandra, S. B. Cenko, A. M. Soderberg, & S. Immler. SN 2006gy: An Extremely Luminous Supernova in the Galaxy NGC 1260. *The Astrophysical Journal Letters*, 659(1):L13–L16, Apr. 2007. doi: 10.1086/516749.

E. O. Ofek, D. Fox, S. B. Cenko, M. Sullivan, O. Gnat, D. A. Frail, A. Horesh, A. Corsi, R. M. Quimby, N. Gehrels, S. R. Kulkarni, A. Gal-Yam, P. E. Nugent, O. Yaron, A. V. Filippenko, M. M. Kasliwal, L. Bildsten, J. S. Bloom, D. Poznanski, I. Arcavi, R. R. Laher, D. Levitan, B. Sesar, & J. Surace. X-Ray Emission from Supernovae in Dense Circumstellar Matter Environments: A Search for Collisionless Shocks. *The Astrophysical Journal*, 763(1):42, Jan. 2013. doi: 10.1088/0004-637X/763/1/42.

J. B. Oke. Absolute Spectral Energy Distributions in Stars. *Annual Review of Astronomy and Astrophysics*, 3:23, Jan. 1965. doi: 10.1146/annurev.aa.03.090165.000323.

A. Pastorello, S. J. Smartt, S. Mattila, J. J. Eldridge, D. Young, K. Itagaki, H. Yamaoka, H. Navasardyan, S. Valenti, F. Patat, I. Agnoletto, T. Augusteijn, S. Benetti, E. Cappellaro, T. Boles, J.-M. Bonnet-Bidaud, M. T. Botticella, F. Bufano, C. Cao, J. Deng, M. Dennefeld, N. Elias-Rosa, A. Harutyunyan, F. P. Keenan, T. Iijima, V. Lorenzi, P. A. Mazzali, X. Meng, S. Nakano, T. B. Nielsen, J. V. Smoker, V. Stanishev, M. Turatto, D. Xu, & L. Zampieri. A giant outburst two years before the core-collapse of a massive star. *Nature*, 447(7146):829–832, June 2007. doi: 10.1038/nature05825.

A. Pastorello, E. Cappellaro, C. Inserra, S. J. Smartt, G. Pignata, S. Benetti, S. Valenti, M. Fraser, K. Takáts, S. Benitez, M. T. Botticella, J. Brimacombe, F. Bufano, F. Cellier-Holzem, M. T. Costado, G. Cupani, I. Curtis, N. Elias-Rosa, M. Ergon, J. P. U. Fynbo, F.-J. Hambsch, M. Hamuy, A. Harutyunyan, K. M. Ivarson, E. Kankare, J. C. Martin, R. Kotak, A. P. LaCluyze, K. Maguire, S. Mattila, J. Maza, M. McCrum, M. Miluzio, H. U. Norgaard-Nielsen, M. C. Nysewander, P. Ochner, Y.-C. Pan, M. L. Pumo, D. E. Reichart, T. G. Tan, S. Taubenberger, L. Tomasella, M. Turatto, & D. Wright. Interacting Supernovae and Supernova Impostors: SN 2009ip, is this the End? *The Astrophysical Journal*, 767(1):1, Apr. 2013. doi: 10.1088/0004-637X/767/1/1.

F. Patat, S. Taubenberger, S. Benetti, A. Pastorello, & A. Harutyunyan. Asymmetries in the type IIn SN 2010jl. *Astronomy & Astrophysics*, 527:L6, Mar. 2011. doi: 10.1051/0004-6361/201016217.

O. Pejcha, B. D. Metzger, & K. Tomida. Cool and luminous transients from mass-losing binary stars. *Monthly Notices of the Royal Astronomical Society*, 455(4):4351–4372, Feb. 2016. doi: 10.1093/mnras/stv2592.

P. Podsiadlowski, P. C. Joss, & J. J. L. Hsu. Presupernova Evolution in Massive Interacting Binaries. *The Astrophysical Journal*, 391:246, May 1992. doi: 10.1086/171341.

D. V. Popov. An Analytical Model for the Plateau Stage of Type II Supernovae. *The Astrophysical Journal*, 414:712, Sept. 1993. doi: 10.1086/173117.

W. H. Press, S. A. Teukolsky, W. T. Vetterling, & B. P. Flannery. *Numerical Recipes 3rd Edition: The Art of Scientific Computing*. Cambridge University Press, New York, 3 edition, 2007.

E. Quataert & J. Shiode. Wave-driven mass loss in the last year of stellar evolution: setting the stage for the most luminous core-collapse supernovae. *Monthly Notices of the Royal Astronomical Society*, 423(1):L92–L96, June 2012. doi: 10.1111/j.1745-3933.2012.01264.x.

H. Sana, S. E. de Mink, A. de Koter, N. Langer, C. J. Evans, M. Gieles, E. Gosset, R. G. Izzard, J.-B. Le Bouquin, & F. R. N. Schneider. Binary Interaction Dominates the Evolution of Massive Stars. *Science*, 337(6093):444, July 2012. doi: 10.1126/science.1223344.

E. M. Schlegel. A new subclass of type II supernovae ? *Monthly Notices of the Royal Astronomical Society*, 244:269–271, May 1990.

J. H. Shiode & E. Quataert. Setting the Stage for Circumstellar Interaction in Core-Collapse Supernovae. II. Wave-driven Mass Loss in Supernova Progenitors. *The Astrophysical Journal*, 780(1):96, Jan. 2014. doi: 10.1088/0004-637X/780/1/96.

N. Smith. Doppler tomography of the Little Homunculus: high-resolution spectra of [FeII]λ16435 around Eta Carinae*. *Monthly Notices of the Royal Astronomical Society*, 357(4):1330–1336, Mar. 2005. doi: 10.1111/j.1365-2966.2005.08750.x.

N. Smith. The Structure of the Homunculus. I. Shape and Latitude Dependence from H_2 and [Fe II] Velocity Maps of η Carinae. *The Astrophysical Journal*, 644(2):1151–1163, June 2006. doi: 10.1086/503766.

N. Smith. Mass Loss: Its Effect on the Evolution and Fate of High-Mass Stars. *Annual Review of Astronomy and Astrophysics*, 52:487–528, Aug. 2014. doi: 10.1146/annurev-astro-081913-040025.

N. Smith. Interacting Supernovae: Types IIn and Ibn. In A. W. Alsabti & P. Murdin, editors, *Handbook of Supernovae*, page 403. Springer, 2017. doi: 10.1007/978-3-319-21846-5_38.

N. Smith & S. P. Owocki. On the Role of Continuum-driven Eruptions in the Evolution of Very Massive Stars and Population III Stars. *The Astrophysical Journal Letters*, 645(1):L45–L48, July 2006. doi: 10.1086/506523.

N. Smith, R. D. Gehrz, P. M. Hinz, W. F. Hoffmann, J. L. Hora, E. E. Mamajek, & M. R. Meyer. Mass and Kinetic Energy of the Homunculus Nebula around η Carinae. *The Astronomical Journal*, 125(3):1458–1466, Mar. 2003. doi: 10.1086/346278.

N. Smith, W. Li, R. J. Foley, J. C. Wheeler, D. Pooley, R. Chornock, A. V. Filippenko, J. M. Silverman, R. Quimby, J. S. Bloom, & C. Hansen. SN 2006gy: Discovery of the Most Luminous Supernova Ever Recorded, Powered by the Death of an Extremely Massive Star like η Carinae. *The Astrophysical Journal*, 666(2):1116–1128, Sept. 2007. doi: 10.1086/519949.

N. Smith, R. Chornock, W. Li, M. Ganeshalingam, J. M. Silverman, R. J. Foley, A. V. Filippenko, & A. J. Barth. SN 2006tf: Precursor Eruptions and the Optically Thick Regime of Extremely Luminous Type IIn Supernovae. *The Astrophysical Journal*, 686(1):467–484, Oct. 2008a. doi: 10.1086/591021.

N. Smith, R. J. Foley, & A. V. Filippenko. Dust Formation and He II λ4686 Emission in the Dense Shell of the Peculiar Type Ib Supernova 2006jc. *The Astrophysical Journal*, 680(1):568–579, June 2008b. doi: 10.1086/587860.

V. V. Sobolev. *Moving Envelopes of Stars*. Harvard University Press, Cambridge, MA and London, England, 1960. ISBN 9780674864658. doi: doi:10.4159/harvard.9780674864658.

J. S. Vink, A. de Koter, & H. J. G. L. M. Lamers. Mass-loss predictions for O and B stars as a function of metallicity. *Astronomy & Astrophysics*, 369:574–588, Apr. 2001. doi: 10.1051/0004-6361:20010127.

A. Vlasis, L. Dessart, & E. Audit. Two-dimensional radiation hydrodynamics simulations of superluminous interacting supernovae of Type IIn. *Monthly Notices of the Royal Astronomical Society*, 458(2):1253–1266, May 2016. doi: 10.1093/mnras/stw410.

L. Wang & J. C. Wheeler. Spectropolarimetry of supernovae. *Annual Review of Astronomy and Astrophysics*, 46:433–474, Sept. 2008. doi: 10.1146/annurev.astro.46.060407.145139.

A. Wongwathanarat, H.-T. Janka, & E. Müller. Three-dimensional neutrino-driven supernovae: Neutron star kicks, spins, and asymmetric ejection of nucleosynthesis products. *Astronomy & Astrophysics*, 552:A126, Apr. 2013. doi: 10.1051/0004-6361/201220636.

A. Wongwathanarat, E. Müller, & H.-T. Janka. Three-dimensional simulations of core-collapse supernovae: from shock revival to shock breakout. *Astronomy & Astrophysics*, 577:A48, May 2015. doi: 10.1051/0004-6361/201425025.

S. Woosley & T. Janka. The physics of core-collapse supernovae. *Nature Physics*, 1(3):147–154, Dec. 2005. doi: 10.1038/nphys172.

O. Yaron & A. Gal-Yam. WISeREP—An Interactive Supernova Data Repository. *Publications of the Astronomical Society of the Pacific*, 124(917):668, July 2012. doi: 10.1086/666656.

O. Yaron, D. A. Perley, A. Gal-Yam, J. H. Groh, A. Horesh, E. O. Ofek, S. R. Kulkarni, J. Sollerman, C. Fransson, A. Rubin, P. Szabo, N. Sapir, F. Taddia, S. B. Cenko, S. Valenti, I. Arcavi, D. A. Howell, M. M. Kasliwal, P. M. Vreeswijk, D. Khazov, O. D. Fox, Y. Cao, O. Gnat, P. L. Kelly, P. E. Nugent, A. V. Filippenko, R. R. Laher, P. R. Wozniak, W. H. Lee, U. D. Rebbapragada, K. Maguire, M. Sullivan, & M. T. Soumagnac. Confined dense circumstellar material surrounding a regular type II supernova. *Nature Physics*, 13(5):510–517, Feb. 2017. doi: 10.1038/nphys4025.

S.-C. Yoon, S. E. Woosley, & N. Langer. Type Ib/c Supernovae in Binary Systems. I. Evolution and Properties of the Progenitor Stars. *The Astrophysical Journal*, 725(1):940–954, Dec. 2010. doi: 10.1088/0004-637X/725/1/940.

T. Zhang, X. Wang, C. Wu, J. Chen, J. Chen, Q. Liu, F. Huang, J. Liang, X. Zhao, L. Lin, M. Wang, M. Dennefeld, J. Zhang, M. Zhai, H. Wu, Z. Fan, H. Zou, X. Zhou, & J. Ma. Type IIn Supernova SN 2010jl: Optical Observations for over 500

Days after Explosion. *The Astronomical Journal*, 144(5):131, Nov. 2012. doi: 10.1088/0004-6256/144/5/131.

W. Zhang, L. Howell, A. Almgren, A. Burrows, & J. Bell. CASTRO: A New Compressible Astrophysical Solver. II. Gray Radiation Hydrodynamics. *The Astrophysical Journal Supplement Series*, 196:20, Oct. 2011. doi: 10.1088/0067-0049/196/2/20.

Appendix A

Scripts

A.1 Selected Functions for Reinitialisation in CASTRO

The following sections detail the core C++ implementations used to map, interpolate, and physically stabilise the state data during the grid expansion pipeline.

A.1.1 `get_nearest_index`

This function locates the nearest discrete coordinate within the original, highly resolved plotfile data array, establishing the baseline values for the mapping onto the new coarse grid.

```
int get_nearest_index(amrex::Real r, amrex::Real z)
{
    int ir = std::min(n_r_bins - 1, std::max(0, int((r - r_min) / dr_bin)));
    int iz = std::min(n_z_bins - 1, std::max(0, int((z - z_min) / dz_bin)));

    int best_idx    = -1;
    amrex::Real min_dist_sq = 1.0e50;

    amrex::Real bin_diag_sq = dr_bin*dr_bin + dz_bin*dz_bin;
    amrex::Real max_dist_sq = 4.0 * bin_diag_sq;

    for (int di = -1; di <= 1; ++di) {
        for (int dj = -1; dj <= 1; ++dj) {
            int check_ir = ir + di;
            int check_iz = iz + dj;

            if (check_ir < 0 || check_ir >= n_r_bins ||
                check_iz < 0 || check_iz >= n_z_bins) continue;

            int check_bin = check_ir + check_iz * n_r_bins;

            int idx = bin_head[check_bin];
            while (idx != -1) {
                amrex::Real dr = r - r_data[idx];
                amrex::Real dz = z - z_data[idx];
                amrex::Real dist_sq = dr*dr + dz*dz;

                if (dist_sq < min_dist_sq) {
                    min_dist_sq = dist_sq;
                    best_idx = idx;
                }
                idx = point_next[idx];
            }
        }
    }
```

Script A.1: Function `get_nearest_index` from `plotfile_data.H`.

A.1.2 Inverse Distance-Weighting Interpolation

To determine values between the discrete points of the original grid, this routine implements the Inverse Distance-Weighting interpolation algorithm, calculating a continuous spatial approximation for the required state variables.

```
amrex::Real interpolate_2d_nearest(amrex::Real r, amrex::Real z,
                                   const amrex::Vector<amrex::Real>& data)
{
    int ir = std::min(plotfile_data::n_r_bins - 1,
                      std::max(0, int((r - plotfile_data::r_min) / plotfile_data::dr_bin)));
    int iz = std::min(plotfile_data::n_z_bins - 1,
                      std::max(0, int((z - plotfile_data::z_min) / plotfile_data::dz_bin)));

    amrex::Real min_dist_sq = 1.0e50;
    int nearest = -1;

    for (int di = -1; di <= 1; ++di) {
        for (int dj = -1; dj <= 1; ++dj) {
            int check_ir = ir + di;
            int check_iz = iz + dj;

            if (check_ir < 0 || check_ir >= plotfile_data::n_r_bins ||
                check_iz < 0 || check_iz >= plotfile_data::n_z_bins) continue;

            int check_bin = check_ir + check_iz * plotfile_data::n_r_bins;

            int idx = plotfile_data::bin_head[check_bin];
            while (idx != -1) {
                amrex::Real dr = r - plotfile_data::r_data[idx];
                amrex::Real dz = z - plotfile_data::z_data[idx];
                amrex::Real dist_sq = dr*dr + dz*dz;

                if (dist_sq < min_dist_sq) {
                    min_dist_sq = dist_sq;
                    nearest = idx;
                }
                idx = plotfile_data::point_next[idx];
            }
        }
    }
```

Script A.2: Function `interpolate_2d_linear` from `plotfile_data.H` utilising Inverse Distance-Weighting.

A.1.3 Three-Zone Logic for State Quantities in the Equatorial Disc

This code block translates the spatial blending mathematics into functional syntax, using a hyperbolic tangent function to smoothly merge the inner numerical simulation data with the outer analytical environment.

```
    Real final_rho, final_temp, final_vel_x, final_vel_y, final_vel_z;
    Real final_spec[NumSpec];

    int idx = plotfile_data::get_nearest_index(xx, yy);
    bool has_plot_data = (idx != -1);

    if (has_plot_data && dist < r_limit_visual) {

        // Load plotfile state s
        Real plot_rho  = plotfile_data::density_data[idx];
        Real plot_temp = plotfile_data::temp_data[idx];
        Real raw_vx    = plotfile_data::xvel_data[idx];
        Real raw_vy    = plotfile_data::yvel_data[idx];
m
        Real speed  = std::sqrt(raw_vx*raw_vx + raw_vy*raw_vy);
        Real plot_vx = speed * sintheta;
        Real plot_vy = speed * costheta;
#if AMREX_SPACEDIM == 3
        Real plot_vz = speed * sinphi;
#else
        Real plot_vz = 0.0_rt;
#endif

        // Species
        Real plot_spec[NumSpec];
        if (idx != -1) {
            plot_spec[0] = plotfile_data::X_H1_data[idx];
            plot_spec[1] = plotfile_data::X_He4_data[idx];
            plot_spec[2] = plotfile_data::X_C12_data[idx];
            plot_spec[3] = plotfile_data::X_O16_data[idx];
            plot_spec[4] = plotfile_data::X_Si28_data[idx];
            plot_spec[5] = plotfile_data::X_Ca40_data[idx];
            plot_spec[6] = plotfile_data::X_Fe52_data[idx];
            plot_spec[7] = plotfile_data::X_Ni56_data[idx];
        } else {
            plot_spec[0] = interpolate_2d_linear(xx, yy, plotfile_data::X_H1_data);
            plot_spec[1] = interpolate_2d_linear(xx, yy, plotfile_data::X_He4_data);
            plot_spec[2] = interpolate_2d_linear(xx, yy, plotfile_data::X_C12_data);
            plot_spec[3] = interpolate_2d_linear(xx, yy, plotfile_data::X_O16_data);
            plot_spec[4] = interpolate_2d_linear(xx, yy, plotfile_data::X_Si28_data);
            plot_spec[5] = interpolate_2d_linear(xx, yy, plotfile_data::X_Ca40_data);
            plot_spec[6] = interpolate_2d_linear(xx, yy, plotfile_data::X_Fe52_data);
            plot_spec[7] = interpolate_2d_linear(xx, yy, plotfile_data::X_Ni56_data);
        }
        // Mass fractions sum to approximately 1.0 , scale to partial densities
        Real sum_plot = 0.0_rt;
        for (int n = 0; n < NumSpec; ++n) sum_plot += plot_spec[n];
        if (sum_plot > 0.0_rt)
            for (int n = 0; n < NumSpec; ++n) plot_spec[n] *= (plot_rho / sum_plot);

        if (dist < blend_start) {
            // ZONE A: Pure plotfile
            final_rho   = plot_rho;
            final_temp  = plot_temp;
            final_vel_x = plot_vx;
            final_vel_y = plot_vy;
            final_vel_z = plot_vz;
            for (int n = 0; n < NumSpec; ++n) final_spec[n] = plot_spec[n];
        } else {
            // ZONE B: Tanh blend
            Real normalized_pos = (dist - blend_start) / blend_width;
            Real x_tanh = 6.0_rt * (normalized_pos - 0.5_rt);
            Real s = 0.5_rt * (1.0_rt + std::tanh(x_tanh));

            final_rho   = (1.0_rt - s) * plot_rho   + s * out_rho;
            final_temp  = (1.0_rt - s) * plot_temp  + s * out_temp;
            final_vel_x = (1.0_rt - s) * plot_vx    + s * out_vx;
            final_vel_y = (1.0_rt - s) * plot_vy    + s * out_vy;
            final_vel_z = (1.0_rt - s) * plot_vz    + s * out_vz;
            for (int n = 0; n < NumSpec; ++n)
                final_spec[n] = (1.0_rt - s) * plot_spec[n] + s * out_spec[n];
        }

    } else {
        // ZONE C: Pure outer domain
        final_rho   = out_rho;
        final_temp  = out_temp;
        final_vel_x = out_vx;
        final_vel_y = out_vy;
        final_vel_z = out_vz;
        for (int n = 0; n < NumSpec; ++n) final_spec[n] = out_spec[n];
    }
```

Script A.3: Utilising a 3-zone logic at the disc from `problem_initialize_state_data.H`.

A.1.4 The Analytical Disc Density Normalisation

To prevent unphysical mass discontinuities at the boundary of the equatorial disc model, this snippet calculates and applies a dynamic scalar normalisation, ensuring the analytical background matches the outermost numerical data point.

```
// Scale analytic density by plotfile/analytic ratio at boundary
Real rho_plot_bnd = interpolate_2d_linear(x_bnd, y_bnd, plotfile_data::density_data);
Real out_rho = rho_ana_cell; // failsafe: pure analytic
if (rho_plot_bnd > 1.0e-30_rt && rho_ana_bnd > 1.0e-30_rt) {
    out_rho = (rho_plot_bnd / rho_ana_bnd) * rho_ana_cell;
}
```

Script A.4: The normalisation for the disc density from `problem_initialize_state_data.H`.

A.1.5 Bipolar Lobes Analytical Background and EOS Closure

To prevent numerical artefacts in the highly expanded Lobes Model, the following segment anchors the outer domain to a strict 100 K thermodynamic floor and injects the expected CNO-processed wind mass fractions.

```
// Outer Analytic Temperature (Pure, smooth background wind)
Real out_temp = 100.0_rt;

// SPECIES: Eta Carinae Homunculus is CNO-processed (Helium-rich)
// Mass fractions: ~40% Hydrogen, ~60% Helium. C/O are heavily depleted.
Real out_spec[NumSpec] = {0.0_rt};
out_spec[0] = 0.40_rt * out_rho; // H1
out_spec[1] = 0.60_rt * out_rho; // He4
```

Script A.5: Analytical background for the lobes `problem_initialize_state_data.H`.

Once the spatial interpolation and analytical blending are complete, a final thermodynamic closure is required. The routine below manually invokes the CASTRO EOS to recalculate the internal energy, guaranteeing mathematical consistency before returning control to the hydrodynamics solver.

```
// ============================================================
// 4. FINAL SAFETY CHECKS & EOS ASSIGNMENT
// ============================================================
final_rho  = std::max(final_rho, 1.0e-23_rt);
final_temp = std::max(final_temp, 100.0_rt);

Real spec_sum = 0.0_rt;
for (int n = 0; n < NumSpec; ++n) spec_sum += final_spec[n];
if (spec_sum > 0.0_rt) {
    Real norm_factor = final_rho / spec_sum;
    for (int n = 0; n < NumSpec; ++n) state(i,j,k,UFS+n) = final_spec[n] * norm_factor;
} else {
    state(i,j,k,UFS) = final_rho;
    for (int n = 1; n < NumSpec; ++n) state(i,j,k,UFS+n) = 0.0_rt;
}

state(i,j,k,URHO)  = final_rho;
state(i,j,k,UTEMP) = final_temp;
state(i,j,k,UMX)   = final_rho * final_vel_x;
state(i,j,k,UMY)   = final_rho * final_vel_y;
state(i,j,k,UMZ)   = final_rho * final_vel_z;

eos_t eos_state;
eos_state.rho = final_rho;
eos_state.T   = final_temp;
for (int n = 0; n < NumSpec; ++n) eos_state.xn[n] = state(i,j,k,UFS+n) / final_rho;

eos(eos_input_rt, eos_state);

state(i,j,k,UEINT) = final_rho * eos_state.e;
Real v_sq = final_vel_x*final_vel_x + final_vel_y*final_vel_y + final_vel_z*final_vel_z;
state(i,j,k,UEDEN) = state(i,j,k,UEINT) + 0.5_rt * final_rho * v_sq;
```

Script A.6: Final safety checks from the EOS for the lobes transition `problem_initialize_state_data.H`.

Full codes used for reinitalisation can be find at https://is.muni.cz/auth/th/k2gxj/Reinitialisation_codes.zip..

A.2 Selected Functions from Custom Package in Julia

A.2.1 Native Data Ingestion and Binary Parsing

To bypass the latency of third-party wrappers, the postprocessing pipeline ingests CASTRO binary data directly into RAM. The following Julia snippet from `reader.jl` demonstrates the core extraction loop, using the `reinterpret` function to instantly map the raw binary stream into multi-dimensional arrays.

```
function read_box!(canvas, file, offset, box, var_idx, n_comps)
    xlo, ylo, xhi, yhi = box
    nx = xhi - xlo + 1; ny = yhi - ylo + 1
    open(file, "r") do io
        seek(io, offset)
        while read(io, UInt8) != 0x0A end
        n_bytes = nx * ny * n_comps * 8
        raw_bytes = read(io, n_bytes)
        full_data = reshape(reinterpret(Float64, raw_bytes), (nx, ny, n_comps))
        canvas[xlo+1:xhi+1, ylo+1:yhi+1] .= full_data[:, :, var_idx]
    end
end
```

Script A.7: The `read_box!` extraction loop from the native Julia reader.

A.2.2 Data Conversion and Physical Downsampling

When exporting high-resolution CASTRO data to the SIROCCO RT code, the grid must be downsampled while rigorously conserving mass and energy. The following snippet from `converter.jl` demonstrates the custom downsampling algorithms. A cylindrical volume-weighted average (`ds_cyl`) is applied to scalar fields like density and temperature, whereas a simple arithmetic mean (`ds_simple`) is applied to vector fields like velocity.

A.2.3 Visualisation: Geometric Reconstruction and Unit Scaling

Because CASTRO simulates the models in 2D axisymmetric coordinates, the visualisation script must dynamically reconstruct the full physical cross-section for analysis. The following snippet from `visualization.jl` demonstrates how the radial coordinates and data arrays are mirrored across the z-axis. It also highlights the dynamic spatial scaling, converting native simulation centimetres into appropriate astronomical units.
The entire custom Julia package can be find at https://is.muni.cz/auth/th/k2gxj/CasPost.zip.

```
# ------------------------------------------------------------
# 2. DOWNSAMPLING
# ------------------------------------------------------------
if factor > 1
    println("\nDownsampling by factor $factor...")

    r_cen0 = [xlims[1] + (i - 0.5)*dx0 for i in 1:nr0]

    function ds_cyl(arr)
        nr_in, nz_in   = size(arr)
        nr_out, nz_out = div(nr_in, factor), div(nz_in, factor)
        out = zeros(nr_out, nz_out)
        for i in 1:nr_out
            for j in 1:nz_out
                i_rng = (i-1)*factor+1 : i*factor
                j_rng = (j-1)*factor+1 : j*factor
                w_sum = 0.0
                val   = 0.0
                for ii in i_rng
                    w = r_cen0[ii]
                    for jj in j_rng
                        val   += arr[ii, jj] * w
                        w_sum += w
                    end
                end
                out[i, j] = w_sum > 0.0 ? val / w_sum : 0.0
            end
        end
        return out
    end

    function ds_simple(arr)
        nr_in, nz_in   = size(arr)
        nr_out, nz_out = div(nr_in, factor), div(nz_in, factor)
        out = zeros(nr_out, nz_out)
        for i in 1:nr_out
            for j in 1:nz_out
                block    = arr[(i-1)*factor+1 : i*factor,
                               (j-1)*factor+1 : j*factor]
                out[i,j] = sum(block) / length(block)
            end
        end
        return out
    end

    density_2d = ds_cyl(density_2d)
    temp_2d    = ds_cyl(temp_2d)
    He4_2d     = ds_cyl(He4_2d)
    vx_2d      = ds_simple(vx_2d)
    vy_2d      = ds_simple(vy_2d)
    vz_2d      = ds_simple(vz_2d)

    println("  Grid after downsampling: $(size(density_2d, 1)) x $(size(density_2d, 2))")
end
```

Script A.8: The `ds_cyl` and `ds_simple` downsampling functions from the native Julia converter.

```
        unit_factors = Dict(
            "cm" => 1.0,
            "m"  => 100.0,
            "au" => 1.495978707e13,
            "pc" => 3.085677581e18
        )

        c_factor = get(unit_factors, lowercase(coord_unit), 1.0)
        display_unit = haskey(unit_factors, lowercase(coord_unit)) ? coord_unit : "cm"

        x_lims_unit = xlims ./ c_factor
        y_lims_unit = ylims ./ c_factor

        view_width_unit = x_lims_unit[2] - x_lims_unit[1]
        max_dim = max(view_width_unit, y_lims_unit[2])

        exponent = 0
        scale_factor = 1.0

        if max_dim > 0 && (max_dim >= 1e4 || max_dim <= 1e-3)
            exponent = Int(floor(log10(max_dim)))
            scale_factor = 10.0^exponent
        end

        xs = LinRange(x_lims_unit[1], x_lims_unit[2], size(data, 1)) ./ scale_factor
        ys = LinRange(y_lims_unit[1], y_lims_unit[2], size(data, 2)) ./ scale_factor

        xs_plot = xs
        data_plot = data

        view_width = (x_lims_unit[2] - x_lims_unit[1]) / scale_factor

        if mirror_r
            xs_plot = vcat(-reverse(xs), xs)
            data_plot = vcat(reverse(data, dims=1), data)
            view_width *= 2.0
        end
```

Script A.9: The spatial unit conversion and radial mirroring logic from the native Julia visualiser.

Appendix B

Light Curves

This section presents the mathematical formalism used to derive synthetic light curves from the calculated spectra. Equation B.1 computes the total bolometric luminosity ($L_{\rm bol}$) at a given time (t_n) and viewing angle (μ) by integrating the specific luminosity (L_ν) across the entire simulated frequency range:

$$L_{\rm bol}(t_n, \mu) = \int_{\nu_{\rm min}}^{\nu_{\rm max}} L_\nu(t_n, \mu)\, {\rm d}\nu\,. \tag{B.1}$$

Equation B.2 calculates the broadband absolute magnitude in the standard AB system (Oke, 1965). This is achieved by convolving the specific flux (f_ν) with the dimensionless filter transmission function, $T_{\rm b}(\nu)$ (Blanton & Roweis, 2007). The inverse frequency weighting (ν^{-1}) accounts for the energy response of photon-counting detectors, while the constant -48.60 provides the standard AB zero-point calibration:

$$M_{\rm AB}(t_n, \mu, {\rm b}) = -2.5 \log_{10}\left[\frac{\int T_{\rm b}(\nu)\nu^{-1} f_\nu(t_n, \mu)\, {\rm d}\nu}{\int T_{\rm b}(\nu)\nu^{-1}\, {\rm d}\nu}\right] - 48.60\,. \tag{B.2}$$

B.1 Bolometric Light Curves

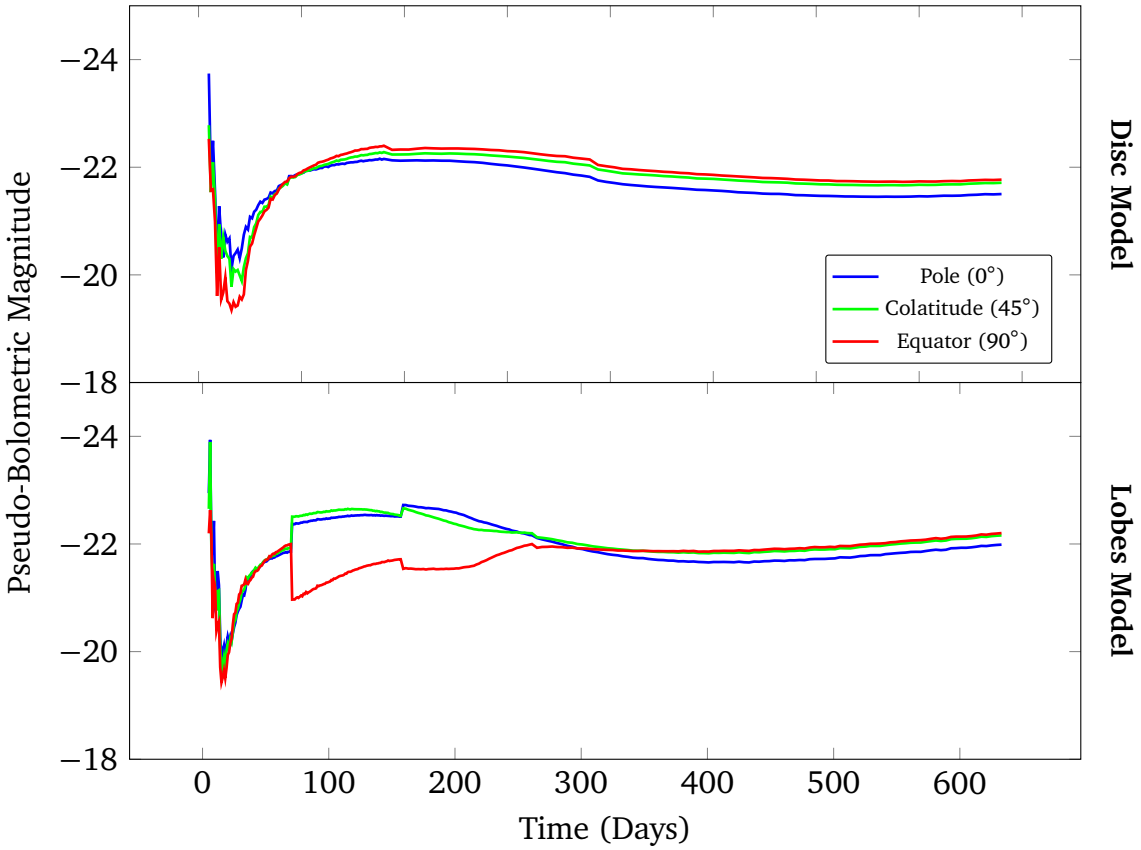

Figure B.1: Synthetic pseudo-bolometric light curves for range $100-30,000$ Å comparing the Equatorial Disc (top) and Bipolar Lobes (bottom) models. Line colors indicate the observer viewing angle: pole-on (0°, blue), mid-latitude (45°, green), and edge-on (90°, red).

B.2 Lightcurve for Specific Bands

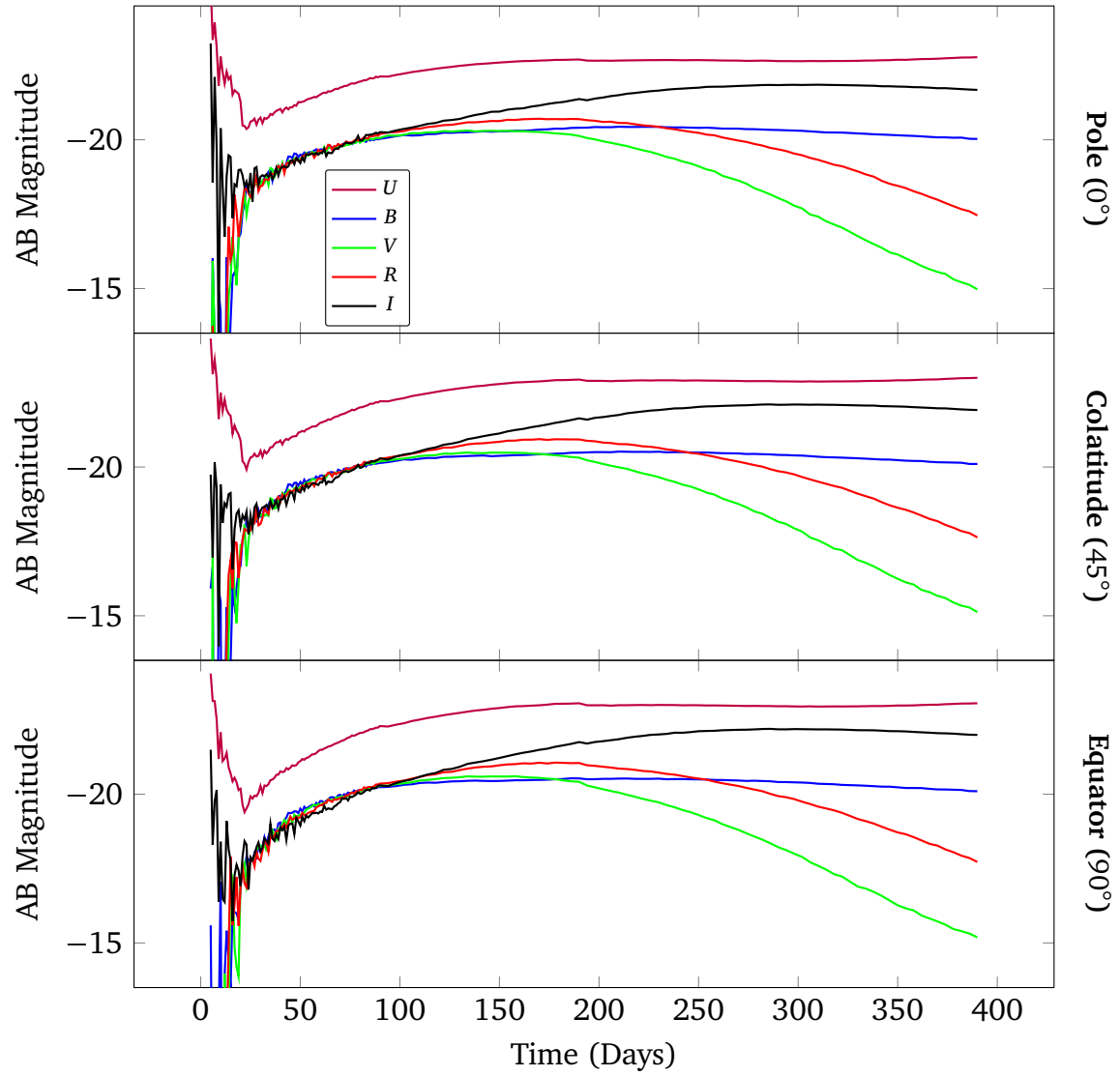

Figure B.2: Synthetic *UBVRI* broadband light curves for the Equatorial Disc model. The panels display the photometric evolution from three distinct viewing angles: pole-on (0°, top), mid-latitude (45°, middle), and edge-on (90°, bottom).

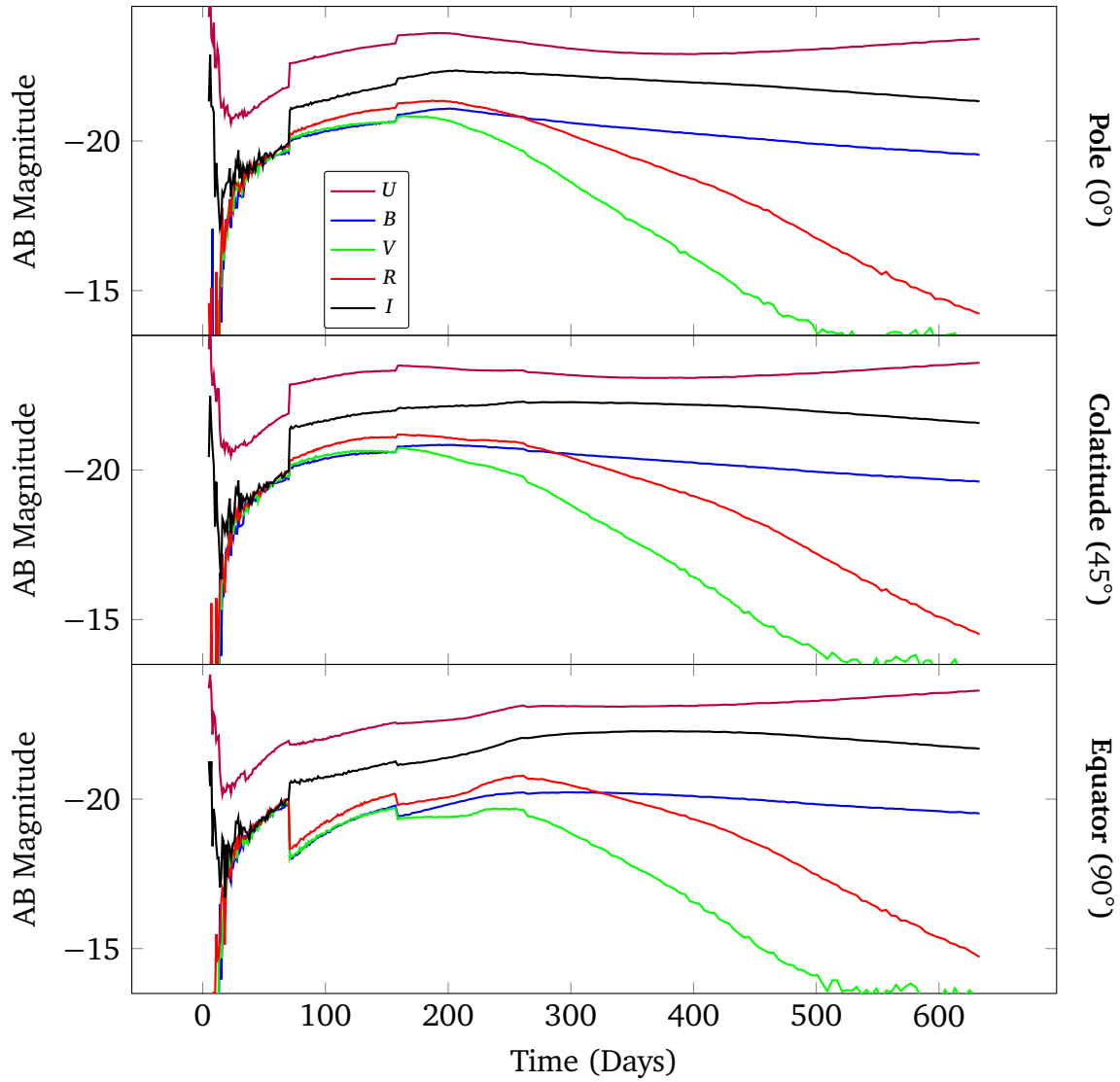

Figure B.3: Synthetic *UBVRI* broadband light curves for the Bipolar Lobes model. The panels display the photometric evolution from three distinct viewing angles: pole-on (0°, top), mid-latitude (45°, middle), and edge-on (90°, bottom)